The Space-time Structure of an Axisymmetric Turbulent Boundary Layer Ingested by a Rotor

N. Agastya Balantrapu

Dissertation submitted to the Faculty of the
Virginia Polytechnic Institute and State University
in partial fulfillment of the requirements for the degree of

Doctor of Philosophy
in
Aerospace Engineering

William J. Devenport, Chair
W. Nathan Alexander
Stewart A. L. Glegg
K. Todd Lowe
Wing F. Ng

December 17, 2020
Blacksburg, Virginia

Keywords: Turbulence structure, boundary layer, transverse curvature, pressure gradient, turbulence ingestion

The Space-time Structure of an Axisymmetric Turbulent Boundary Layer Ingested by a Rotor

N. Agastya Balantrapu

(ABSTRACT)

A low-speed, axisymmetric turbulent boundary layer under a strong adverse pressure gradient is experimentally studied for its relevance to marine applications, urban air-transportation and turbulence ingestion noise. The combined effect of lateral curvature and streamwise pressure gradient are examined on the mean flow, turbulence structure, velocity correlations and wall pressure fluctuations. Additionally, the upstream influence of a rotor operating in this flow is examined to improve the understanding of the turbulence necessary to develop advanced noise prediction tools. Measurements were made in Virginia Tech Stability tunnel documenting the flow over a 0.432-m diameter body-of-revolution comprised of a forward nose-cone, a constant diameter mid-body and a 20 degree tail-cone, at a length based Reynolds number of 1.2 million.

The principal finding of this work is the resemblance of the boundary layer to a free-shear layer where the turbulence far from the wall plays a dominant role, unlike in the canonical case of the flat-plate boundary layer. The mean flow along the tail developed inflection points in the outer regions and the associated velocity and turbulence stress profiles were self-similar with a recently proposed embedded shear layer scaling. As the mean flow decelerates downstream, the large-scale motions energize and grow along with the boundary layer thickness; However, the structure is roughly self-similar with the shear-layer scaling, emphasizing the role of the shear-layer in the large-scale structure. Additionally, the correlation structure is discussed to provide information towards the development of turbulence models and aeroacoustic predictions.

The associated wall pressure fluctuations, measured with a longitudinal array of microphones, evolved significantly downstream with the dimensional wall pressure spectra weakening by over 20-dB per Hz. However, the spectra collapsed to within 2-dB with the wall-wake scaling, where the pressure-scale is the wall shear stress, and the time-scale is derived from the boundary layer thickness and edge velocity. The success of this scaling, even in the viscous roll-off regions, suggests the increasing importance of the outer region on the near-wall turbulence and wall-pressure. Investigation of the space-time structure revealed the presence of a quasi-periodic feature with the conditional signature of a roller-eddy. The structure appeared to scale with the wall-wake scaling, and was found to convect downstream at speeds matching those at the inflection points (and outer turbulence peak). It is hypothesized that the outer region turbulence in strong adverse pressure gradient flow strongly drive the near-wall turbulence and therefore both the wall pressure and shear stress.

Subsequent measurements made with the rotor operating at the tail, using high-speed particle image velocimetry, provided the space-time structure of the inflow turbulence as a function of the rotor thrust. The impact of the rotor on the mean flow, turbulence and correlation structure in the vicinity of the rotor is discussed to supply information towards validating numerical simulations and developing turbulence models that account for the distortion due to the rotor.

This work was sponsored by the Office of Naval Research, in particular Drs. Ki-Han Kim and John Muench under grants N00014-17-1-2698 and N00014-20-1-2650.

The Space-time Structure of an Axisymmetric Turbulent Boundary Layer Ingested by a Rotor

N. Agastya Balantrapu

(GENERAL AUDIENCE ABSTRACT)

Understanding turbulent flows adjacent to surfaces placed in fluid flows is necessary to develop efficient technologies to mitigate undesirable drag, vibrations and noise. Particularly, this is of an increased interest with the imminent abundance of urban short-haul air transportation. While several fundamental aspects of these flows have been clarified, certain specific areas still remain to be addressed, including the impact of curved surfaces, like those of submarine hulls and aircraft fuselage, and the impact of mean pressure gradients.

This study seeks to fill some of these gaps by studying the flow over a body-of-revolution through wind tunnel experiments. The nature of the velocity and wall-pressure fluctuations are examined in detail. It was found that the boundary layer was significantly different from the canonical case of a flat-plate flow, with the mean velocity and turbulence structure developing the characteristics of a free-shear layer (flows unbounded by surfaces). Specifically, the velocity and turbulence intensity appeared self-similar with a recently proposed embedded shear layer scaling, which is based on the parameters at the inflection point in the mean velocity profile. The large-scale motions in the outer regions, despite energizing and growing as the flow decelerated downstream, appeared self-similar with the shear layer parameters, emphasizing the role of shear layer motions within in the boundary layer. This is important since the turbulence relatively further from the wall are now the important sources of pressure fluctuations and therefore drag, vibrations and noise. The associated wall-pressure fluctuation were studied with a focus on the wall-pressure spectrum and the space-time structure. A quasi-periodic feature was detected in the instantaneous fluctuations, which had a conditional structure reminiscent of a conditional roller, and appeared to convect downstream at speeds matching those at the inflection points in the velocity profile. Therefore it is hypothesized that the large-scale motions in the embedded shear layer play a dominant role on the near-wall turbulence and therefore on the wall pressure and shear-stress. This is different from the behavior of the wall-studied flow past a flat-plate. It is therefore important to factor this into technologies aiming to increase the efficiency and quieten the vehicles

Acknowledgments

Thanks to my mom Anita, my dad Venkateswar Rao, my brother Chotu and my fiancée Sadhana; For being ever supportive and enabling me to pursue my dream.

Thanks to my undergrad advisor Dr. Kunal Ghosh for mentoring and encouraging me to pick an academic career. And then my PhD advisor and my role-model, Dr. William Devenport. You are the finest example of a research leader and an inspiring teacher. In addition to shaping my goals and transforming my abilities as a researcher, you have really shaped my personality; You taught me the art of communicating, the philisophy of leading and a spirit of optimism; I hope to not only carry these forward but to share them with my future colleagues and students; Thank you. Thanks also to my committee members, Dr. Nathan Alexander, Dr. Stewart Glegg, Dr. Todd Lowe and Dr. Wing Ng; Your guidance and suggestions have assumed a critical role in my journey towards PhD.

Thanks to my colleagues here at CREATe and VT whom I enjoyed working with; The list here is pretty long, spanning a couple of research generations: Dr. Liselle Joseph, Dr. Ian Clark, Dr. Christopher Hickling, Nick Molinaro, Anthony Millican, and Harsh Sharma from my early years; Dr. Kyle Daniel, Ashley Saltzman, Chi Young Moon, Russell Repasky, Vidya Vishwanathan, Nandita hari, Shishir Damani, and Dr. Matthew Szoke from my later years. Special thanks goes here to Liselle for introducing me the group and mentoring me in my early years. Also, my colleague and dear friend Christopher, thank you for always being there - the scenic drives, family dinners, and de-stressing walks in the COVID-era have energized me to keep moving forward during challenging times.

Thanks are particularly due to Bill Oetjens and Dr. Aurilien Borgoltz for their help with over ten weeks of testing at the tunnel; Also the expertise at the AOE machine shop, particularly of Mr. James Lambert, Cameron Hollandsworth and Scott Patrick was instrumental in developing the hardware. Thanks much to the friendly staff at AOE main office, specially, Kelsey, Courtney, Cameron, and Erin, for facilitating help with processing countless purchases, travel reimbursements and organizing social events.

Also, my friends – rather – my family at Blacksburg with whom I built many, long-lasting memories, specially with Srinath, Sadhana, Vijay, Kai, Vishnu, and Pavan Gundu.

At the time of writing this thesis, the world was working its way through COVID, a global life-threatening pandemic. I am greatly indebted to all front-line medical professionals and administrative leaders for rising to this challenge.

Contents

List of Figures ix

List of Tables xv

1 Introduction 1

1.1 Structure and Contents 2

1.2 Attributions 3

1.3 Achievements 3

2 Background and Literature Review 5

2.1 Structure and dynamics of a zero pressure gradient boundary layer 5

2.1.1 Mean velocity profile 5

2.1.2 Statistics of turbulent motions 7

2.1.3 Instantaneous dynamics and coherent structures 7

2.2 Effects of adverse pressure gradient on the flow 9

2.3 Effect of lateral curvature on the flow 11

2.4 Summary of Literature 12

3 The structure of a highly decelerated axi-symmetric turbulent boundary layer 13

3.1 Abstract 14

3.2 Introduction 14

3.3 Apparatus and instrumentation 17

3.3.1 Wind Tunnel 17

3.3.2 Steady pressure measurements 19

3.3.3 Turbulent velocity measurements 19

3.4 Results and Discussion 22

3.4.1 Axial symmetry impact of tethers and trip height 23
3.4.2 Characteristics of the inflow to the APG ramp 24
3.4.3 Mean flow characteristics on the ramp 26
3.4.4 Turbulence statistics on the APG ramp 28
3.4.5 Self-similarity in the outer region along the ramp 30
3.4.6 Turbulence structure of streamwise velocity 34
3.4.7 Correlation structure of streamwise velocity 36
3.5 Conclusions 44
3.6 Acknowledgements 44
3.7 Declaration of interests 45
3.8 References 45

4 Wall pressure signature of an axisymmetric boundary layer under a strong adverse pressure gradient 47

4.1 Abstract 48
4.2 Introduction 48
4.3 Apparatus and instrumentation 51
4.3.1 Fluctuating wall pressure measurements 53
4.4 Results and Discussion 54
4.4.1 Flow characteristics and parameters 54
4.4.2 Wall pressure spectrum: trends and scaling 56
4.4.3 Space-time structure and relation to spectral scaling 60
4.5 Conclusions 66
4.6 Acknowledgements 67
4.7 Declaration of interests 67
4.8 References 67

5 Space-time structure of an axisymmetric boundary layer ingested by a rotor 70

5.1 Introduction 71

5.2 Apparatus and Instrumentation 72
5.2.1 Time-resolved measurements of the inflow to the rotor 74
5.3 Results and Discussion 76
5.3.1 Inflow at nominally zero thrust 76
5.3.2 Effect of thrust on the mean flow 79
5.3.3 Effect of thrust on the turbulence 83
5.4 Conclusions 84

6 Conclusions and Outlook **87**

Bibliography **90**

List of Figures

2.1 Schematic of the zero pressure gradient turbulent boundary layer 6

3.1 Schematic of the top-view of the test-section showing the BOR geometry and experimental arrangement 19

3.2 (a) Photograph of the BOR installed in test-section of Virginia Tech Stability Tunnel (b) Arrangement of 85 pressure taps on the body: 52 ports measuring the streamwise distribution and 36 ports measuring the circumferential uniformity 20

3.3 Schematic showing the various measurements of the turbulent velocity over the Body-of-Revolution 20

3.4 Velocity measurements on the BOR ramp with single hotwire (a) Dual probe arrangement on ramp to measure the single point statistics and large-scale convection velocity. (b) Radial correlations at the BOR tail (x/D = 3 .172) measured with a moving and fixed single hotwire. (c) Arrangement to measure circumferential correlation at the tail 22

3.5 Setup for PIV measurements on the tail cone. Laser sheet - pulsed from a sufficiently downstream station - illuminated the tail cone boundary layer and a single camera mounted directly above the field-of-view was traversed along the ramp. 23

3.6 (a) Schematic showing the location of stagnation pressure cross-section measured to verify circumferential uniformity. (b) Contours of stagnation pressure coefficient (C_{po}) at BOR tail verifying circumferential uniformity. 24

3.7 Streamwise pressure distribution on the BOR; Measurement; Potential flow simulation; LES from Zhou et al. (2020) 25

3.8 (a) Mean velocity profile upstream of corner (x/D=1.977); U_∞ is the tunnel free-stream velocity (See table 3.1) (b) Turbulence intensity profile at x/D=1.977 25

3.9 Contours of streamwise mean velocity (U_s) on the ramp from single hotwire measurements scaled on the tunnel reference velocity (U_∞); Arrows at the measurement stations reveal the flow orientation as measured by quadwire. Broken black line identifies the edge of the boundary layer. Inset to the top right shows the global position of the measurement. 27

3.10 Characteristics of Boundary layer on ramp: (a) Displacement thickness (δ_1) as a fraction of the velocity thickness (δ) (b) Shape factor H $= \delta_1/\delta_2$ (c) Skin-friction coefficient (C_f) from LES Zhou et al. (2020) 27

3.11 Flow parameters in APG region (a) Pressure gradient parameters (b) Reynolds numbers 29

3.12 Contours of streamwise Reynolds normal stress on the ramp from single hotwire measurements scaled on the tunnel reference velocity. Inset to the top right shows the global position the measurement. 30

3.13 (a)Turbulence kinetic energy based on in-plane Reynolds normal stresses. (b) Ratio of streamwise normal stress to kinetic energy (c) Ratio of streamnormal normal stress to kinetic energy (d) Ratio of Reynolds shear stress stress to kinetic energy 31

3.14 (a) Mean velocity profiles with the vertical axis representing the distance from the surface scaled with δ and horizontal axis representing the velocity scaled with the edge velocity. (b) Profiles of the streamwise Reynolds stress with the $U_e - \delta$ scaling. Legend to the right shows the streamwise positions. . . . 32

3.15 (a) Mean velocity profiles with $U_e - \delta_1$ scaling. (b) Profiles of the streamwise Reynolds stress with the $U_e - \delta_1$ scaling. (c) Location of the peak streamwise Reynolds stress scaled on δ_1 . See figure 3.14 for legend. 32

3.16 Embedded shear layer scaling for mean flow. (a) Mean velocity defect profiles with black line representing the complementary error function $1 - erf(\eta)$. (b) Streamwise Reynolds normal stress profiles (c) Streamwise growth of vorticity thickness (δ_ω) of the shear layer. See figure 3.14 for legend. 34

3.17 Contours of the pre-multiplied spectra of the streamwise velocity $f' G_{u_s u_s}/U_\infty^2$ at representative streamwise stations on the ramp. Frequency $f' = fD/U_\infty$ where D is body diameter (D = 0.4318 m) and U_∞ is tunnel free-stream velocity. (a) x/D = 2.3 (b) x/D = 2.62 (c) x/D = 2.85 (d) x/D = 3.17. Dashed lines indicate the position of the peak levels relative to the surface and the corresponding frequency. 35

3.18 Comparison of the turbulence structure at various upstream stations with that at the downstream BOR tail (x/D=3.17). Contours level represent the ratio of the pre-multiplied power spectra to that at the BOR tail on a dB -scale. (a) x/D = 2.3 (b) x/D = 2.62 (c) x/D = 2.85 35

3.19 Contours of the pre-multiplied spectra of the streamwise velocity $f'G_{u_s u_s}/U_d^2$ at different streamwise stations on the ramp. Frequency $f' = f\delta_\omega/U_e$ where δ_ω (x) is vorticity thickness and U_e(x) is edge velocity. (a) x/D = 2.3 (b) x/D = 2.62 (c) x/D = 2.85 (d) 3.17. Horizontal dashed lines indicate the position of the peak levels in the shear layer and vertical dashed lines indicate the center-frequency of the broad peaks 36

3.20 Contours of the pre-multiplied spectra of the streamwise velocity $f'G_{u_s u_s}/U_d^2$ at different streamwise stations on the ramp. $f' = f\delta_\omega/U_e$ where δ_ω (x) is vorticity thickness and U_e(x) is edge velocity. (a) x/D = 2.3 (b) x/D = 2.62 (c) x/D = 3.17. 37

3.21 Pre-multiplied spectra of the streamwise velocity based on shear layer parameters. Line spectra in each plot are shown for a particular location in the shear- layer based co-ordinate system. Line spectra shown for η = -1; -0.5; 0; 0.5; 1; moving from bottom to top. 37

3.22 Integral timescale of the streamwise velocity on the ramp boundary layer. (a) Time-scales normalized on constant reference velocity and BOR diameter; grey arrows shown the variation in the downstream direction. (b) Integral scales from (a) normalized on δ/U_s; orange curve represents the corresponding integral scales from a planar zero- pressure gradient boundary layer at a Re_{δ_2}=15000 (Morton et al. 2012); Corresponding x-axis shown on top. (c) Integral scales normalized on the shear layer time-scale (δ_ω/U_e). For legend see Figure 3.14 38

3.23 Contours of convection velocity normalized on the local mean streamwise velocity measured from dual single-hotwire measurements. Dashed black line represents the boundary layer edge on ramp 39

3.24 (a) Two point correlation of the streamwise velocity from PIV with anchor point at x/D = 3.172 and $-$z/D = 0.177 (corresponds to 0.56 δ from surface). (b) Spatial correlation from (a) as a function of streamwise separation from PIV compared with hotwire estimates via Taylor's hypothesis. 40

3.25 Two-point correlation from PIV compared to spatial correlation obtained from single-point hotwire measurements using Taylor's hypothesis 41

3.26 (a) Integral length scales in the boundary layer at x/D = 2.933; (b) Apparent convection velocity at representative streamwise stations; 42

3.27 (a) The cross-section at Ramp tail (x/D=3.17) showing the measurement grid for circumferential and radial correlation measurements. Circumferential correlations were measured about the vertical axis and radial correlations along the horizontal axis. The contour levels in the background reveal the turbulence intensity; (b) Correlation coefficient of the streamwise velocity: solid lines indicate PIV results; dashed line indicate hotwire results. Streamwise correlation in black; radial in red; and circumferential in blue. 43

4.1 Schematic of the test-section showing the BOR geometry and experimental arrangement. 52

4.2 Schematic showing the circumferential location of the surface mics on the tail cone with respect to the tethers. The view corresponds to as seen by an observer located downstream of the BOR and viewing directly downstream. 53

4.3 Longitudinal arrangement of the surface mics on the BOR tailcone. The microphones are arranged on the rear-half of the tail with a nominal spacing of 12.5-mm 54

4.4 Dimensional auto-spectra of the wall pressure fluctuations $\phi(f)$ for various streamwise positions on the tail. The spectra is normalized with $p_{ref} = 20\mu Pa$ to show the sound pressure level (SPL). Legend shown towards the right of the figure where the color shifts from bright to dark on going downstream . 56

4.5 (a) Non-dimensional auto spectra of the fluctuating pressure with frequency normalized on the outer-scale (U_e/δ) and pressure scaled with shear stress at the wall (τ_w). (b) Root mean square of the fluctuating pressure along the tail scaled on τ_w. (c) The viscous time-scale along the ramp shown as a function of the outer scale of the flow. 58

4.6 Non-dimensional wall pressure spectra with other candidate time-scales where τ_w is the pressure-scale.(a) Viscous scaling with $f\nu/u_\tau^2$ (b) Embedded shear layer scaling with $f\delta_\omega/U_e$. (c) Zagarola-Smits scaling fU_{zs}/δ where $U_{zs} = U_e\delta_1/\delta$. (d) Displacement thickness scaling $f\delta_1/U_e$. 59

4.7 Snapshot of the instantaneous pressure along the ramp with time on the horizontal axis and position on the tail on the vertical axis. Contours represent the pressure normalized with the corresponding root-mean-square values. The snapshot corresponds to 0.2-seconds of a total of 32-seconds. 61

4.8 (a) Snapshot of the pressure signal at x/D=2.85 (b) Magnitude of the wavelet transform corresponding to the signal in (a) 62

4.9 Contours of the large intermittency measure for a 0.2-second snapshot of the pressure signal at x/D=2.85 estimated from equation **??** based on the wavelet transform of the signal shown in figure 8(a-b). 63

4.10 (a) The conditional structure of the wall pressure at $x/D = 2.88$ (b) Conditional structure from all streamwise stations with the pressure normalized on the local wall shear-stress τ_w and the time-delay normalized with the outer-time scale δ/U_e. 64

4.11 Space-time correlation function of the wall pressure show at representative locations on the tail. (a) x/D = 2.73 (b) x/D = 2.85 (c) x/D = 3.05. 64

4.12 Phase convection velocity of the wall pressure shown as a function of spatial separation between the probes normalized on the boundary layer thickness. Each curve corresponds to an anchor microphone position with the corresponding color and symbols shown in the legend above. 66

5.1 Photograph of the test-section, showing the experimental arrangement comprised of a BOR, a rotor mounted at the BOR tail that is driven by the downstream drive-system via a hollow shaft. 73

5.2 Rendering of the geometry of the five-bladed rotor immersed in the tail boundary layer, showing the front-view and the side-view. The diameter of the rotor is 216 mm which corresponds to half the diameter of the BOR. 73

5.3 Photograph showing the experimental arrangement for the time-resolved particle image velocimetry measurements. The cameras and laser installed outside the floor were focused onto the axial-radial plane (shown in the insert at top-right) just upstream of the rotor. 75

5.4 (a) Contours of the time-averaged axial mean velocity (normalized on the tunnel free-stream velocity) for the zero-thrust configuration with J = 1.44; Thick black line represents the edge of the boundary layer. (b) Profiles of the mean velocity in the axial, radial and circumferential directions from the tail exit (shown by the vertical grey line in (a) compared with previous measurements from no-rotor configuration 77

5.5 Turbulence profiles at the BOR tail for J = 1.44. (a) Turbulence stresses based on the time-averaged mean velocity, compared with results from the no-rotor measurements. (b) Auto-spectrum of the axial unsteady velocity, shown at three representative locations in the boundary layer at the BOR tail, and compared against the no-rotor results. Sold lines represent the zero-thrust results while dotted lines represent the no-rotor estimates. 78

5.6 Contours of the premultiplied spectra of the axial velocity compared for (a) no-rotor case and (b) with the rotor at zero-thrust 79

5.7 Contours of the mean axial velocity revealing the effect of thrust on the inflow. The axial velocity is normalized with the corresponding values from J = 1.44 to demonstrate the change relative to zero-thrust. (a) shows the result for J = 1.10 or the moderate thrust case and (b) shows the result for J = 2.64, the braking condition (negative thrust) 80

5.8 Results from the radial profile at the BOR tail ($x/D = 3.1717$) evaluating the effect of thrust. Time averaged mean velocities are shown in (a) and Reynolds stress of the axial velocity are shown in (b). Black represents the zero-thrust results, J = 1.44 (from figure 5.4(b)), blue represents the results for J = 1.10 and red represents the results for J = 2.64. 81

5.9 Mean velocity and turbulence profiles at the BOR tail ($x/D = 3.1717$) from figure 5.8 normalized on the boundary layer parameters. Vertical axis represents the distance from the surface ($|y - y_s|$) normalized with the boundary layer thickness (δ) while horizontal axis represents the mean velocity magnitude U (a), Reynolds normal stress of the axial velocity (b), and the turbulence kinetic energy ($TKE = 0.5(u_x^2 + u_r^2 + u_\theta^2)$) (c), all normalized with the edge velocity U_e. Color legend shown in figure 5.8 82

5.10 Mean velocity profile at the BOR tail with embedded shear layer scaling for the thrusting conditions, shown with the results from various streamwise stations on the tail measured without the rotor (from Balantrapu et al. [6]). 82

5.11 Contours of the pre-multiplied spectra of the axial velocity with the boundary layer scaling, revealing the impact of the rotor on the turbulence structure. (a) J = 1.10, (b) 1.44 and (c) J = 2.64 83

5.12 Contours of the auto-correlation coefficient of the axial velocity $\rho_{u_x u_x}$, as a function of time-delay τ, showing the effect of the rotor on the turbulence length scales. Note that the results correspond to zero separation in the boundary layer. (a) Results from no-rotor (b) J = 1.44 (c) J = 1.10 (d) J = 2.64 85

List of Tables

3.1 Boundary layer characteristics at inflow (x/D=1.977) to the BOR ramp . . 26

3.2 Boundary layer characteristics on the ramp. C_f and U_τ are obtained from large eddy simulations on the BOR at matched Reynolds number (Zhou et al. 2020). 28

3.3 Integral length scales of the streamwise velocity in the radial and circumferential direction at the BOR tail 43

4.1 Flow parameters at the mic locations. C_f U_τ are obtained from large eddy simulations on the BOR at matched Reynolds number. 55

5.1 Test matrix for the time-resolved inflow measurements 74

5.2 Operating conditions and flow parameters for various advance ratios 81

Chapter 1

Introduction

Turbulent boundary layers – the thin viscous regions of flow close to surfaces in flight – are known to generate significant drag, vibrations and noise. These undesirable consequences lead to decreased flight efficiency that translates to higher carbon emissions, in addition to noise pollution and tactical vehicle detection. The noise pollution is a particularly growing concern due to the imminent proliferation of short-haul urban transportation, along with the abundance of unmanned aerial vehicles. Fundamentally, the turbulent flows generate pressure fluctuations on the underlying surfaces resulting in unsteady structural vibrations and noise. The radiated noise is a key concern when turbulent flows convect past the sharp discontinuity like airfoil trailing edge, or when a ingested by rotors and must be addressed to meet increasingly stringent regulations.

Understanding turbulent flows and their interaction with the moving surfaces is a prerequisite to develop technologies to mitigate drag and noise in practical applications. However, due to the inherent complexities of turbulent flows, most research was aimed at an idealized case: the flow over a smooth flat-plate aligned with the flow, known as the zero-pressure gradient turbulent boundary layer (ZPGTBL). Consequently we have well established scaling laws, and well accepted models of the velocity layer structure [67], wall-pressure spectrum [7, 11, 26], skin-friction [72, 78], and far-field acoustic signature [22]. But practical configurations such as aircraft and marine vehicles have more complex boundary conditions including surface curvature, mean pressure gradients, surface roughness, and obstacles. These conditions are expected to significantly alter the turbulence structure and it is important to understand the turbulence structure to extend or replace the existing models for the flat-plate flow.

This dissertation aims to enhance the knowledge of the practical configurations, by considering the strongly decelerating flow over a body-of-revolution, imitating the case of aircraft fuselages and marine vehicles. Particularly, the impact of surface curvature and streamwise pressure gradient examined on the velocity and wall pressure structure based on wind-tunnel measurements. The evolution and scaling laws for the mean flow, turbulence structure and correlation structure and wall pressure spectrum are investigated. Additionally, the influence of a rotor ingesting the flow is examined through spatio-temporally resolved particle image velocimetry measurements, to provide insights into the rotor-flow interaction, as required to develop more accurate noise prediction tools. The detailed structure and organization of the dissertation is explained below in § 1.1, followed by the list of attributions that describe the contributions of all investigators of the project in § 1.2. A list of major findings and the associated achievements are then mentioned in § 1.3.

1.1 Structure and Contents

This is a manuscript style dissertation, comprising of six chapters that are partly composed of manuscripts that are either under revision or to be submitted to peer-reviewed journals.

Chapter 1 describes the motivation and outlines the structure and contents of the dissertation.

Chapter 2 is comprised of a summary of previous work in the areas of axisymmetric boundary layers and pressure-gradient boundary layers. Here, the concepts and definitions are introduced only briefly as a more detailed literature review relevant to each chapter is attached locally with each chapter .

Chapter 3 is the first manuscript titled "The structure of a highly decelerated axisymmetric turbulent boundary layer" has been submitted and reviewed by the Journal of Fluid Mechanics and is currently under revision. The paper begins with a review of the previous work, summarizing the current understanding of the effects of curvature and adverse pressure gradients on the structure and mechanics of the boundary layers. The wind-tunnel measurements are then discussed, beginning with a description of the inflow conditions to the tail cone, followed by the characterization of the flow on the tail. The self-similarity in the outer region is evaluated with respect to the mean flow and turbulence structure. Finally, the correlation structure, measured with a combination of hotwire anemometry and particle image velocimetry are presented, highlighting the differences with respect to the well-studied fundamental case of the flat-plate flow.

Chapter 4 is the second manuscript titled "The wall pressure signature of an axisymmetric boundary layer under a strong adverse pressure gradient" and will be submitted to the Journal of Fluid Mechanics. The paper describes the wall pressure fluctuations associated with the turbulence described in chapter 3. First, a review is presented of the relevant wall pressure studies examining the effects of surface curvature and mean pressure gradient on the wall pressure spectrum. Then the measurement setup and intrumentation, largely similar to that in chapter 3, is summarized. The results are discussed, including an examination of the wall pressure spectrum scaling and the space-time structure of the pressure fluctuations.

Chapter 5 is the third manuscript titled "The space-time structure of an axisymmetric boundary layer ingested by a rotor" and will be submitted to the Journal of Fluid Mechanics after further analysis. This paper discusses the space-time structure of the flow ingested by a rotor for a range of thrusting conditions. The distortion of the mean flow and the turbulence structure in the vicinity of a rotor is evaluated as a function of thrust with an ultimate goal to supply information towards the development of more accurate turbulence models and noise prediction tools.

Chapter 6 discusses the conclusions of this work and identifies avenues of further research.

The formatting of the dissertation varies across the chapters due to the inclusion of journal manuscripts. While chapters 1, 2, 5 and 6 are presented in the conventional dissertation format, the manuscripts in chapters 3 and 4 are presented in the original format of the journal.

1.2 Attributions

The work presented in this dissertation has benefited from collaborations with several colleagues and mentors mentioned below.

Dr. Christopher Hickling has been a close collaborator on this project. Particularly, his leadership during the design and fabrication of the body-of-revolution and the associated hardware has been instrumental. He is a co-author on several journals and all conference proceedings that resulted from this work. Further, his dissertation work includes a companion study of the noise radiated by the propeller ingesting the BOR flow discussed in this work in chapter 5.

Dr. William J. Devenport is the principal investigator and the chair of the advisory committee for the work presented here. In addition to conceptualization, funding acquisition and project management, he has closely supervised and reviewed the work presented here.

Dr. W. Nathan Alexander is the co-principal investigator of this work and a member of the advisory committee for the work presented here. His role in the conceptualization, funding acquisition and project management was parallel to that of Dr. William Devenport.

Dr. Stewart A. L. Glegg is a member of the advisory committee and has provided valuable advice during the data analysis stage.

Dr. Meng Wang and his student Di Zhou have provided the skin-friction estimates from their large eddy simulation work, which played an important role in chapters 3 and 4.

1.3 Achievements

The key findings and achievements of this work are summarized below.

- The tail boundary layer is very different from the flat-plate case, and is strongly impacted by the adverse pressure gradient. The flow is out of equilibrium and evolves significantly along the tail becoming increasingly wake-like. However, the mean velocity and turbulence intensity along the ramp is shown to be self-similar with a recently proposed embedded shear layer scaling.

- The flow becomes increasingly turbulent in the outer regions and the large-scale motions energize and grow roughly with the boundary layer thickness. Spectral analysis showed that the low-frequency motions scale with the shear layer parameters, emphasizing the role of the embedded shear layer in organizing the turbulence.

- The correlation structure of the boundary layer has been documented to provide inputs to turbulence ingestion noise predictions. It is hypothesized that non-linear interactions could be important given the high turbulence levels as it was discovered that the turbulence in the inner half of the boundary layer convected about one and a half times faster than the local mean speed. Therefore corrections are required when extrapolating the single-point measurements to a multidimensional correlation structure, to serve as inputs to aeroacoustic predictions.

- The fluctuating pressure on the wall, imposed by the turbulent motions, appear to be governed by the motions across the layer. While shear-stress at the wall is the pressure scaling, the outer scales, based on the boundary layer thickness and edge velocity serve as the governing time scales. The associated wall pressure spectrum collapsed to within 2-dB with this scaling, as compared with a 20-dB varation in the dimensional spectrum.

- The existence of quasi-periodic feature in the wall pressure, with a roller type signature, was detected using wavelet analysis. The conditional structure appeared to scale with the mixed scaling and convected at speeds that matched those at the inflection points in the flow, suggesting that inviscid instabilities could be playing a role in adverse pressure gradient layers.

- It is hypothesized that the outer region turbulence plays a very significant role in the layer, influencing the near-wall motions and consequently both the skin-friction and wall pressure. Further investigation using three-dimensional, spatio-temporally resolved datasets are required to validate this hypothesis.

- Non-intrusive spatio-temporally resolved measurements of inflow to the rotor, operating at the tail of the body, were made using high-speed, two-dimensional, three-component particle image velocimetry. The results obtained as a function of thrust are expected to provide a direct insight into the influence of rotors on the inflow in addition to validating advanced large-eddy simulations and augmenting the development of more accurate turbulence modelling.

Chapter 2

Background and Literature Review

This chapter serves the purpose of providing a context to the work that follows, complementing the detailed review in each of the manuscripts in the following chapters. Here, the fundamental case of a zero pressure gradient layer is reviewed in detail to introduce the velocity structure and provide an insight into the turbulent motions. This is followed by a brief discussion of the effects of lateral curvature and adverse pressure gradients. A more detailed review is included in chapters 3 and 4, covering the effects on both the velocity and wall pressure fluctuations respectively.

2.1 Structure and dynamics of a zero pressure gradient boundary layer

Figure 2.1 shows the schematic of a two-dimensional flow over a smooth flat plate ($y = 0$), generated by a uniform free-stream with velocity U_∞. With the absence of mean pressure gradient and surface curvatures this is generally referred to as the zero-pressure-gradient turbulent boundary layer (ZPGTBL). Extensive research into this canonical configuration over the past few decades has lead to an improved understanding and subsequent incorporation into review articles and textbooks, and will be briefly reviewed here.

2.1.1 Mean velocity profile

The boundary layer is widely thought to comprise of an inner region ($0 < y < 0.15\delta$) dominated by viscosity and an outer region where viscosity plays an indirect role in the momentum transport processes. Accordingly, for the inner region, the velocity and length scales are based on the wall-shear stress τ_w and viscosity ν with $U_\tau = \sqrt{\tau_w/\rho}$ as the velocity scale and ν/U_τ is the length-scale. For the outer region, U_τ remains as the velocity scale, with the length scale generally taken as the thickness of the boundary layer(δ) itself. Furthermore, the inner region is dynamically very active, and has been sub-structured into three zones: an inner, viscous sublayer where the turbulence is suppressed by the wall, and the velocity varies as $U/U_\tau = yU_\tau/\nu$ or $U^+ = y^+$; This is followed by a buffer layer that transitions into a logarithmic layer where the log law ($U^+ = \frac{1}{\kappa}ln(y^+) + C$) is expected to hold. Here, κ is the Karman's constant and C is a constant which are generally about 0.39 and 4.9 respectively.

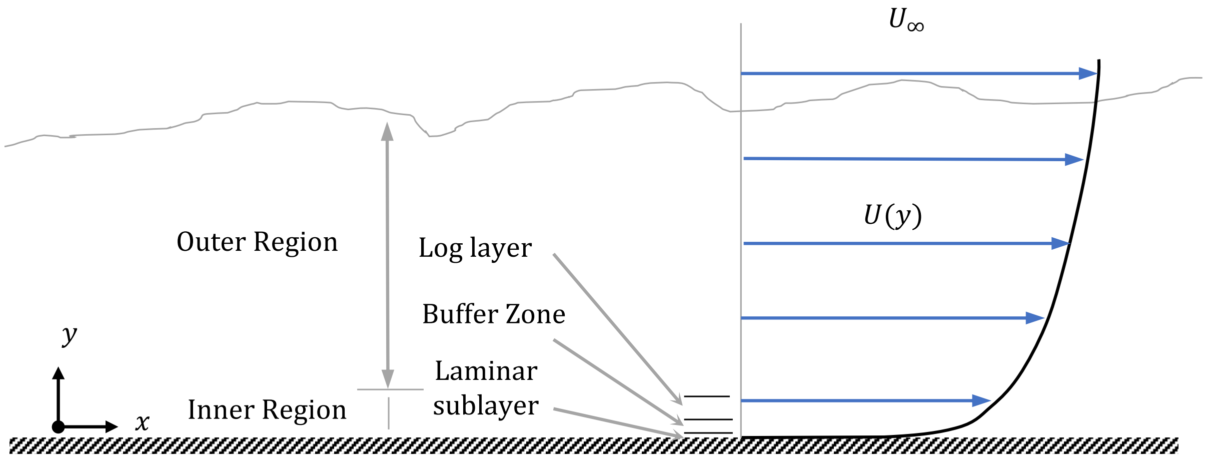

Figure 2.1: Schematic of the zero pressure gradient turbulent boundary layer

While the exact extents of these layers have been found to be Reynolds number dependent [70], the viscous sub-layer is generally very thin (0.01δ) extending upto $y^+ \approx 7$, where as the log layer extends from $30\nu/U_\tau < y < 0.15\delta$.

The outer region – the remaining 85% of the boundary layer above the log region – is also known as the wake layer. The velocity profile here is described by the defect law,

$$\frac{U_e - U}{U_\tau} = f\left(\frac{y}{\delta}\right) \tag{2.1}$$

which implies that the momentum deficit even far away from the wall is sustained by the skin-friction. Modelling the outer region as a deviation from the log law, Coles [14] proposed a law of the wake,

$$\frac{U}{U_\tau} = \frac{1}{\kappa} ln(y^+) + C + \frac{\Pi}{\kappa} W\left(\frac{y}{\delta}\right) \tag{2.2}$$

where $W(\frac{y}{\delta})$ is the wake function, considered universal and formulated as $2sin^2\ (\pi y/2\delta)$ and Π is the wake strength parameter, is empirically found to be about 0.51. In summary, the mean velocity profile has been established for the flat-plate layer and can be estimated with the knowledge of a few parameters: the boundary layer thickness δ, the edge velocity U_e and the friction velocity U_τ. However, it must be noted that two different scalings, the wall law and wake law, are required to completely describe the boundary layer profile and consequently the velocity profile is never strictly self-similar. For example, the extent of the inner region increases with the wake region shifting outward, as the Reynolds number increases [70, 79].

2.1.2 Statistics of turbulent motions

Though the fluctuating motions are complex and range across a wide spectrum of scales, they are organized by the wall and the statistical behavior of the motions is well-established. While all motions are damped right at the surface due to friction and rigidity, the statistics increase on moving outward, peaking in the inner regions before eventually decaying across the outer region. For example, the streamwise Reynolds stress u^2 profiles attain a maximum just above the viscous sublayer ($y^+ \approx 15$ [41]) before decaying to zero outside the edge of the boundary layer. Though the location of this peak has been widely accepted to be constant, recent experimental studies accounting for the sensor-resolution effects [16, 34], observed the magnitude to weakly depend on the Reynolds number. This Reynolds dependence appears to arise from increasing contribution from the large-scale motions in the log region that modulated the underlying small scale motions [49]. This dependence seems to have been captured by the mixed scaling $\sqrt{U_\tau U_e}$ proposed by DeGraaff and Eaton [16].

In the outer regions the motions are nearly isotropic, with the vertical and the spanwise normal stresses approximately equal to the streamwise stresses [22]. Closer to the wall, the motions become increasingly anisotropic, with $u^2 > w^2 > v^2$ throughout the layer. In the logarithmic region, both the wall-normal and the spanwise stresses peak, at about half the streamwise stress levels, with v^2 slightly smaller than w^2 due to the wall-normal boundary condition. The Reynolds shear stresses $\overline{uv}$, representing the vertical transport of the streamwise momentum, is usually negative, and peaks in the log region with a maximum of U_τ^2 before being damped down at the wall.

2.1.3 Instantaneous dynamics and coherent structures

The dynamics of the motions, responsible for the statistical properties mentioned above, have been extensively studied [1, 21, 29, 35, 37, 64], focusing mainly on coherent structures, which are considered responsible for much of the production, transport and dissipation of the turbulent energy, through their formation, interactions and demise. Several definitions of coherent structure or eddies exist [20, 32], but they generally imply three dimensional motions that are spatially correlated (through some variable such as velocity, vorticity) and importantly, persist over a significant time period [1]. Such coherent motions are known to occur on a wide range of spatial and temporal scales and are somewhat organized by the wall. These instantaneous motions can be identified through flow-visualization, conditional sampling techniques, and eduction methodologies such as Proper Orthogonal Decomposition [61] and the results depend on the method used. Adrian [1], Panton [57], Robinson [64] among others have critically reviewed the coherent motions, although at low Reynolds numbers (due to sensor limitations), and will be briefly discussed here. Different coherent motions, identified by extensive research, can be broadly classified into [70]:

- Low-speed near wall streaks

- Hairpin or horse-shoe vortices of a range of scales
- Large scale motions formed by groups of hairpin vortices
- Very large scale motions or super structures at high Reynolds number flows, possibly formed from streamwise alignment of large-scale motions

Close to the wall, alternating, elongated regions of low and high speed regions, known as streaks, are known to exist. These structures are coupled to quasi-streamwise vortices [27, 36, 64] which lift the low speed momentum away on the upward side and bring down the high speed fluid on the downward side, leading to the streaky structures. Identified by Kline et al. [42] in their low Reynolds number flow visualization study, these streaks were found to occur in the viscous and the buffer regions ($y^+ < 50$) and were about 1000 wall units long, spaced in the spanwise direction by about 80 - 120 units and had a velocity roughly about half the local mean velocity. Though quiet initially, the streaks were observed to turn away from the wall, unstably break and ejected into the overlying higher speed flow. Such motions, known as ejections, often occur in groups and is termed as the bursting. These ejections, with u<0 and v>0 contribute to the Q2 motions (Wallace [73]) and are responsible for the shear-stresses and generation of turbulent structures. Often, such motions are followed by sweeps - downward sloping motions of high momentum (first identified by Corino and Brodkey [15]) obeying the conservation of mass, also known as Q4 motions. Both sweeps and ejections contribute to the production of Reynolds shear stresses, explaining the near-wall peak explained in § 2.1.2; For the flat plat boundary layer, while ejection motions dominate the buffer layer beyond $y^+ = 12$, the sweep motions dominate the inner regions.

In the outer regions, arch-type vortices shaped like hairpin/horseshoe exist, with the combination of both types co-existing in the logarithmic overlap layer. Such a model has been observed in both low and high Reynolds number flows, both experimentally Adrian [1] and through numerical simulations Kim et al. [39]. Frequently, these hair-pins extend all the way from the wall to the boundary layer edge, and are straight over extended regions, inclined at 45° to the wall. At the wall, the transverse dimensions are about $100\nu/U_\tau$ wide (corresponding to the streak spacing) and get thicker with increasing distance from the wall [1]. Conceivably, the general shape appears to depend on the Reynolds number, with rounded structures existing at lower Reynolds and elongated horse-shoes or hair-pins at higher Reynolds numbers [29].

Through direct numerical simulations, Zhou et al. [80] observed the vortical structures with a minimum strength (relative to the mean flow vorticity) to subsequently produce secondary hair-pin structures – termed autogeneration – suggesting their occurrence in groups called packets. At higher Reynolds numbers ($Re_\theta > 7800$) these vortex packets, long and ramp-shaped, were found to be denser and occasionally extending across the layer and characterized by low streamwise momentum zones within them (due to coherent vortex induction) [2, 31]. Such Large Scale Motions (LSMs), asociated with the outer bulges at the boundary layer edge, were shown to have a streamwise scale of $2 - 3\delta$ [70].

Furthermore, at even higher Reynolds numbers, it is possible that the largest vortex packets – consisting of a heirarchy of smaller packets – are meandered spanwise, with the longest streamwise scales reaching 10δ-15δ [33]; Commonly referred to as Very Large Scale Motions (VLSMs) and superstructures. Not easy to detect through single point measurements, these superstructures, possibly restricted to the log regions, could significantly contribute to the time-averaged Reynolds stresses and turbulent kinetic energy [21]. Additionally, the large scale super structures can impress their footprints on the near-wall motions, progressively modulating them at higher Reynolds numbers [33, 49], hinting towards a top-down mechanism unlike the bottom-up energy transfer mechanisms proposed by much lower Reynolds number studies.

In summary, there is enough evidence outlining the importance of various coherent structures in turbulent boundary layers. Under zero-pressure gradient, the low speed streaks and quasi-streamwise vortices dominate the wall sublayer and buffer regions. In the logarthmic and outer regions, hairpin vortex structures exist and contribute significantly to the turbulent kinetic energy and Reynolds stress production. In higher Reynolds number flows, packets of hairpin vortices enveloping elongated zones (2-3δ) of low speed fluids exist and are found to extend to the outer region through the logarithmic regions. Larger packets, known as superstructures/ VLSMs could exist with streamwise lengthscales of $(10$-$15)\delta$ and modulate the near-wall structures, playing important role in the turbulence dynamics. Such a picture, with a hierarchy of super-packets, packets and individual hairpins is consistent with the primitive energy cascade hypothesis by Richardson [63]. Furthermore, at any streamwise location, the structure changes from progressively new packets formed near the wall to older and larger, detached packets further away, perhaps imparting a 'memory' to the outer flow [2].

2.2 Effects of adverse pressure gradient on the flow

Adverse pressure gadient (APG) flows occur in all practical applications – aircraft fuselage and wings, marine vehicles, wind turbines, automobiles, compressor blades, pipes and channel flows. As the flow decelerates downstream under the APG, the structure of the mean flow, turbulence, and therefore the fluctuating pressure alters significantly, and the flow could eventually separate leading to loss in performance and efficiency. Furthermore, propellers operating downstream of marine vehicles and aircraft – such as Piaggio Avanti P180, MQ-9 Reaper – ingest the body boundary layers radiating both tonal and broadband noise; This noise, a source of discomfort and tactical disadvantage, is a direct function of the correlation structure of the incoming boundary layer flow [23]. Therefore understanding the effects of APG on the turbulence and its correlation structure is critical towards the development of accurate noise prediction models, and ultimately efficient vehicles. While intense study over the last few decades has certainly developed our understanding of APG flows, several specific challenges remain; A short review of the progress and remaining challenges is presented below while a more specific review, and the exact limitations that this dissertation addresses are presented in chapter 3 and 4.

Pressure gradient flows are an outstandingly complex problem, as the flow is sensitive to the upstream history in addition to the Reynolds number and local pressure gradient – posing an infinite parametric space. However, previous studies have discovered several characteristics that are generic to all APG flows. For example, as the flow decelerates, the mean velocity deficit increases across the boundary layer and the outer regions play a more important role, with the large-scale turbulence intensifying, as a new secondary peak in the turbulent stresses manifests in the outer region. However, as the pressure gradient increases, the outer regions gradually expand into the inner regions, and the defect law fails to collapse mean velocity profiles, especially when $U_\tau \to 0$ as the flow approaches separation. The defect law formulation is valid only for a special class of flows – engineered by Clauser [13], known an equilibrium flows – where the inputs (the force history, pressure gradient) are in equilibrium with the output (the mean velocity profile). Such layers have a constant force history represented by the parameter,

$$\beta_C = \frac{\delta_1}{\tau_w}\frac{\partial p}{\partial x} \tag{2.3}$$

that suggests the strength of the pressure-gradient force relative to the skin-friction. Several other works [8, 9, 19, 47, 48, 50, 59] have proposed different pressure gradient parameters in their attempts to produce self-similarity and equilibrium, but have met with limited success that are valid only for a certain section of pressure gradient flows. Recently, Maciel et al. [46] examined the prominent scalings and noted that is not possible to collapse the flow statistics from a broad range of pressure gradient flows; Instead the success of a scaling can only be judged based on the order of magnitude of the resulting collapse. With such an argument, they observed that the Zagarola-Smits scale – with $U_{ref} = U_e\delta_1/\delta$ and $L_{ref} = \delta$ – was the most successful for a broad spectrum of pressure-gradients. The ZS scaling, originally proposed by Zagarola and Smits [79] as an outer scaling for pipe flows, and first extended to pressure gradient flows by Castillo and George [9], represents the bulk average velocity deficit and appears to capture the memory of the flow through the parameter δ_1/δ.

However, the full structure of the velocity is not yet clear. There is no consensus on whether an inner-outer region classification is still valid; Under what conditions the log-region breaks down and what is the process of breakdown – if it is general or systematic, via a change in the slope and offsets. Similarly, the impact of APG on the near-wall viscous regions and the law of the wall is not established. Progress on such issues requires a sustained and sytematic study over a broad range of pressure-gradients, with carefully designed experiments that are supplemented by expensive simulations.

Similar arguments extend to the Reynolds stress profiles in an adverse pressure gradient flow. However, as mentioned earlier, it is known that the Reynolds stress profiles deviate from the canonical case; The peak in the inner region decays and a new secondary peak develops in the outer regions, which amplifies and shifts outward with an increasing pressure-gradient, as observed by numerous works [5, 8, 28, 46, 47, 56, 66, 69]. Similar peaks, observed in the cross-stream normal stress and Reynolds shear stress, were shown to coincide with new peaks in the turbulence production, dissipation and transfer [40] suggesting a possibility of a fundamental change in the turbulent physics, especially when the pressure gradient is strong. In fact some studies have suggested a resemblence to free-shear flows [40, 66] and are discussed in detail in Chapter 3 of this dissertation.

Studies examining the outer region turbulence have observed that the large-scale activity is amplified, and the outer region turbulence appears to modulate the near-wall turbulence both in the amplitude and frequency [18, 28], somewhat similar to high Reynolds number ZPGTBLs discussed above. The exact reason for the large-scale domination is not clear. However, a recent DNS study revealed that the hairpin vortex packets which concatenate to form the LSMs are affected by the pressure gradient. Under mild APG ($\beta_C < 2$), the concatenation of the hairpin packets is enhanced resulting in a larger streamwise lengthscale than in a ZPGTBL at similar conditions; However, at stronger APGs the concatenation was suppressed and therefore the streamwise lengthscale was reduced, even in comparison to a ZPGTBL [44]. Furthermore, it was found that the Q2 and Q4 motions in the outer regions suggested the presence of counter-rotating roll modes that played an important role in the organization of the turbulence at strong APGs [44, 66].

2.3 Effect of lateral curvature on the flow

The effects of lateral curvature have been studied by considering axial flow past a circular cylinder. Generally, the impact of transverse curvature, discussed in greater detail in Chapter 3 and 4, has been characterized by two parameters. i) δ/r_s: the ratio of the boundary layer thickness to local radius of curvature; ii) $r_s^+ = r_s U_\tau/\nu$, the radius based Reynolds number [60]. Flows with high δ/r_s generally correspond to thin cylinder flows, with high r_s^+ high Reynolds number flow over a thin cylinder, and those with low r_s^+ corresponding to axisymmetric wakes with thin wall layers; These represent applications like the towed-array systems, where the transverse curvature effects are significant, and have been studied by several works [12, 38, 45, 58, 62, 71, 74]. This study concerns with the case of a low δ/r_s and high r_s^+ which corresponds to a high Reynolds number flow over a large cylinder, like in vehicle-relevant conditions.The effects of transverse curvature, though mild, could still be significant in such cases.

For example, the mean velocity profiles are known to be fuller, with increased shear stress at the wall. The turbulence statistics have been observed to decay at a faster rate on moving from the wall [43]. This has been attributed to a relatively lower surface area per unit volume of the flow, that could generate the turbulence. However, the fundamental turbulence structure is shown to be mostly similar to the flat-plate case (presented in § 2.1.3), except an enhanced large-scale turbulence due to the weaker constraint imposed on the flow by the cylindrical wall with a lower area.

2.4 Summary of Literature

This work considers an axisymmetric boundary layer under a strong adverse pressure gradient, which is of relevance to marine vehicles and short-haul urban air transportation. Before examining the combined effects of adverse pressure gradient and lateral curvature on the turbulence and flcutuating wall pressure, a short review is provided of the previous work. The canonical case of a zero-pressure gradient boundary layer over a flat-plate, covering the mean velocity profile, turbulence statistics and instantantaneous dynamics are reviewed to provide a context for the following discussion on the individual effects of lateral curvature and APG.

While the effects of lateral curvature are mild for vehicle relevant conditions, the effects of adverse pressure gradient can be significant and complex; In general, it is found that establishing the detailed structure of the velocity and turbulence as a function of APG requires a systematic study over a range of APGs through carefully designed experiments and simulations and is beyond the scope of this work. This study focuses on the effects of strong APG on the boundary layer and previous work has suggested a fundamental change in the character of such boundary layers. Some studies have observed the velocity profiles in the outer region to become inflectional at wall-normal locations corresponding to the secondary peaks in turbulence production, dissipation and transfer; Recent studies have suggested a strong resemblance to fre-shear flows, proposing a new embedded-shear layer scaling for the mean flow. The following chapters, in the form of journal manuscripts, review the concerned body of literature in greater detail, followed by an examination of the fundamental aspects of the mean flow, turbulence and fluctuation wall pressure in order to reveal the physics of such boundary layers; Additionally, the documented data is expected to serve in validating large-eddy-simulations, and providing the source terms to serve as inputs to predictions of turbulence ingestion noise.

Chapter 3

The structure of a highly decelerated axi-symmetric turbulent boundary layer

This chapter includes the manuscript submitted to the Journal of Fluid Mechanics and is currently under revision.

The structure of a highly-decelerated axi-symmetric turbulent boundary layer

N. Agastya Balantrapu[1], Christopher Hickling[1], W. Nathan Alexander[1], and William Devenport[1]†

[1]Department of Aerospace and Ocean Engineering, Virginia Tech, Blacksburg, VA 24060, USA

(Received xx; revised xx; accepted xx)

Experiments were performed over a body-of-revolution at a length-based Reynolds number of 1.9 million. While the lateral curvature parameters are moderate ($\delta/r_s < 2, r_s^+ > 500$), the pressure gradient is increasingly adverse ($\beta_C \in [5–18]$), reminiscent of vehicle-relevant conditions. The mean flow in the outer regions of this fully-attached boundary layer displays some properties of a free-shear layer, with the mean velocity and turbulence intensity profiles attaining self-similarity with the 'embedded shear layer' scaling (Schatzman & Thomas 2017). Spectral analysis of the streamwise turbulence revealed that, as the mean flow decelerates, the large-scale motions energize across the boundary layer, growing proportionally with the boundary layer thickness. When scaled with the shear layer parameters, the distribution of the energy in the low frequency region is roughly self-similar, emphasizing the role of the embedded shear layer in the large-scale motions. The correlation structure of the boundary layer is discussed at length to supply information towards the development of turbulence and aeroacoustic models. One major finding is that the estimation of integral turbulence length scales from single-point measurements, via Taylor's hypothesis, requires significant corrections to the convection velocity in the inner 50% of the boundary layer. The apparent convection velocity is roughly 40% greater than the local mean velocity, suggesting the turbulence is convected much faster than previously thought. Closer to the wall even higher corrections are required.

Key words: [TBD]

1. Introduction

Turbulent boundary layers growing over axially symmetric bodies, such as the fuselage of some aircraft or marine vehicles, are very common and have been the focus of many past research efforts (Cipolla & Keith 2003; Glauert & Lighthill 1955; Jordan 2014; Kumar & Mahesh 2018; Lueptow *et al.* 1985; Neves *et al.* 1994; Piquet & Patel 1999; Rao 1967; Snarski & Lueptow 1995; Tutty 2008). Understanding the fundamental mechanisms and the interaction of these layers with the environment is important as they are a source of significant drag, noise and structural vibrations. Particularly, these boundary layers are often ingested by rotors, generating both tonal and broadband sound known

† Email address for correspondence: devenport@vt.edu

as turbulence ingestion noise (Glegg & Devenport 2017), which is a growing concern due to the imminent abundance of short-haul urban air transportation.

Most research in axially symmetric boundary layers has considered axial flow past a constant-radius circular cylinder, excluding any streamwise pressure gradient effects. The impact of the lateral curvature on the flow has been commonly characterized by two parameters, (i)δ/r_s, ratio of boundary layer thickness to radius of curvature, and (ii) $r_s^+ = r_s u_\tau/\nu$, radius based Reynolds number, where u_τ and ν are the skin-friction velocity and kinematic viscosity respectively. Three flow regimes have been reported based on these parameters, i) large r_s^+ and large δ/r_s, corresponding to a high Reynolds number flow over a long slender rod ii) small r_s^+ and large δ/r_s, corresponding to an axially symmetric wake with an inner layer due to the wall, and iii)large r_s^+ and small δ/r_s, corresponding to the high Reynolds number flow over a large cylinder (Piquet & Patel 1999). The first two regimes, with significant curvature effects, have been extensively studied with their relevance to towed array sensor systems (Cipolla & Keith 2003; Lueptow *et al.* 1985). The third regime representing practical, vehicle relevant conditions, has received comparatively less attention. Though this flow regime is relatively similar to the flat-plate boundary layer, many important effects are still observed, such as higher skin-friction and fuller velocity profiles due to increased transverse mixing. The turbulence intensity away from the surface is lower compared to the flat-plate case, due to the relatively fuller mean velocity profiles (Kumar & Mahesh 2018; Piquet & Patel 1999). However, the fundamental structure of the turbulence has been shown to remain very similar to the flat-plate counterpart, except the enhanced large-scale activity due to the less-constrained motion, as a result of the relatively smaller surface area (Neves *et al.* 1994; Snarski & Lueptow 1995). For a detailed summary, refer to Jordan (2014).

However, axially symmetric boundary layers under streamwise pressure gradients have not been investigated in detail, with the recent studies focusing only on the mean flow in the adverse pressure gradient (APG) region and downstream wake (Hammache *et al.* 2002; Kumar & Mahesh 2018). This is not surprising, since planar pressure gradient flows themselves are complex and are under active investigation. Generally, the flow structure is sensitive to the Reynolds number, local pressure gradient and the upstream history (Bobke *et al.* 2017), posing a prohibitively large parameter space. Despite such a challenge several aspects have been clarified, including an increased mean velocity defect in the outer region, and a corresponding increase in the turbulence activity, manifesting as a secondary peak in the turbulence stresses, that amplifies and drifts away from the wall with increasing pressure gradient (Kitsios *et al.* 2017; Nagano *et al.* 1998). Several studies on the turbulence structure of APG layers have attributed this to the increased importance of large-scale motions (on the order of boundary layer thickness) in the outer region. For example, Vila *et al.* (2017) have shown that the first four modes of a moderately-decelerated boundary-layer, estimated through proper orthogonal decomposition (POD), accounted for 40% of the turbulent kinetic energy, and captured both the magnitude and location of the outer peak in the Reynolds streamwise normal stress and shear stress profile. While the details are, of course, sensitive to the flow history and local parameters, these large-scale motions in the outer layer (log region and above) have been shown to strongly interact with the small-scale motions closer to the wall, modulating both the amplitude and frequency (Lee 2017; Harun *et al.* 2013; Drozdz & Elsner 2017).

Questions regarding the impact of APG on the growth and organization of the large-scale motions in the outer region have been partly answered, with Skåre & Krogstad (1994);

Maciel *et al.* (2017) observing the sweeping motions to be stronger and to occur more frequently than ejections, compared to their equal probability for the ZPG case. Lee (2017) – in his direct numerical simulation (DNS) of mild ($\beta_C = (\delta_1/\tau_w)dp/dx = 0.72$), moderate ($\beta_C = 2$) and strong ($\beta_C = 9$) APG layers – observed the characteristics of the energized large-scale motions to be very sensitive to the severity of APG. While the spanwise length-scale of the conditional u'-structures increased monotonically with the pressure gradient, the streamwise length scale did not; The streamwise scale was longer for weak APG ($\beta < 2$) but was significantly shorter at stronger APG, shorter even in comparison with the ZPG case. By analyzing both the instantaneous and conditional structures, he observed that the streamwise hairpin structures actively concatenated into larger motions at mild APG, but were generally more separated and less coherent, resulting in reduced concatenation for stronger APG. Additionally, he observed this suppression of the hairpin vortex packets to be associated with increased importance of the conditional roll modes – that were centered in the outer layer and corresponded to sweeps and ejections – in organizing the overall flow. Overall, this is indicative of a fundamental change in the turbulence structure as the boundary layer experiences a strong APG.

Indeed, both experimental (Skåre & Krogstad 1994) and DNS studies (Gungor *et al.* 2016; Kitsios *et al.* 2017) investigating large-defect boundary layers have observed a new secondary peak in the turbulence kinetic energy production, dissipation and transfer, collocated with the peak in the turbulent stress profiles. Furthermore, some of these studies have also observed the mean velocity profiles to be inflectional at the same location that generally indicate inviscid instability, prompting Kitsios *et al.*; Gungor *et al.* to suggest some resemblance with free shear flows. While the inflectional profiles have been observed in previous experimental studies as well (Song *et al.* 2000; Elsberry *et al.* 2000), recent investigation by Schatzman & Thomas (2017) has revealed some strong evidence for the resemblance to free shear flows. Through quadrant-analysis of the shear-stress profiles, measured by laser Doppler anemometer, they observed sweeping motions to dominate above the inflection point and ejections to dominate below. This spatial organization, observed at all streamwise locations in the boundary layer, led them to hypothesize the presence of an embedded shear layer with spanwise-oriented coherent vorticity centered about the inflection point. These motions were attributed to inviscid instabilities as the Rayleigh-Fjørtoft theorem was satisfied, which requires the spanwise mean vorticity to reach a maximum at the inflection point (i.e $U''(U-U_{IP}) < 0$, where $'$ denotes differentiation with respect to the cross-stream coordinate and U_{IP} is the velocity at the inflection point). Inspired from prior work on free-shear layers, they proposed new length and velocity scales, based on the shear and velocity at the inflection point. With these scales and a coordinate system centered about the inflection point the mean velocity and turbulence intensity profiles over a significant streamwise extent were found to collapse. While this is certainly encouraging, there are several outstanding questions. For instance, the instantaneous flow is not expected to 'see' the mean velocity profile, and therefore the occurrence of inflectional instabilities is debatable. Though Schatzman & Thomas find that the Rayleigh-Fjørtoft theorem is satisfied at the outer inflection point, which is considered a necessary and generally sufficient condition for the presence of inviscid instabilities, Maciel *et al.* find no evidence for the coherent structures indicative of such an instability, Kevin-Helmholtz or varicose. Furthermore, this hypothesis is not compatible with the occurrence of an outer peak in the Reynolds stresses even in the absence of inflection points, as in the flow of Maciel *et al.* (2018). This gives rise to a conjecture that the inflectional velocity profiles and the outer turbulence peaks are simply correlated, without sharing a cause-and-effect relationship. In any case, further investigation into this requires a systematic study over a broad range of pressure gradients and is outside our scope. Here, our interest is to examine whether the embedded shear layer scaling is valid for an axisymmetric body, with a practical and vehicle-relevant configuration, and if so, to observe the implications on the turbulence and correlation structure, from a perspective of providing information to support the turbulence modelling and aeroacoustic predictions.

It is important to mention that from a broader perspective of developing a framework for non-equilibrium APG flows, there are several outstanding issues, many of which are discussed by Maciel *et al.* (2018). For example, the layer-structure of APG flows, as to a clear definition of 'outer' versus 'inner' regions; a consistent choice of parameters to quantify the various forces; and a parameter to represent the flow history, require a continuation of sustained effort, meticulous experiments and rigorous analysis.

To conclude, axially-symmetric boundary layers with moderate curvature parameters but strong axial pressure gradient – that represent practical, vehicle-relevant conditions – are not understood due to the inherent complications posed by axial pressure gradient. The relative importance of the different aspects, and the validity of some of the recent developments in APG flows must be examined with respect to mean flow, turbulence, and correlation structure. The present study aims to fill some of these gaps through experiments over a body-of-revolution, with the key objectives being:

(i) to reveal the physics of an axially-symmetric boundary layer with a practical flow history, examining both the mean flow and the turbulence structure, and in part, examine the embedded shear layer hypothesis.

(ii) to provide the experimental dataset for validation of Large Eddy Simulations for high Reynolds number, adverse pressure gradient flows.

(iii) to provide new quantitatively usable insight into the correlation structure as needed to define the source terms for turbulence ingestion noise prediction and other flow acoustic problems.

2. Apparatus and instrumentation

2.1. *Wind Tunnel*

This study was performed in the Virginia Tech Stability Wind Tunnel, a low-speed closed-circuit facility with an interchangeable test-section that is 7.32 m long, with a 1.85-m x 1.85-m cross-section. All measurements were made in the anechoic test-section, where the side-walls are formed by tensioned Kevlar 120 fabric that remains acoustically transparent while containing the flow. These side-walls are flanked by anechoic chambers lined with 0.610-m acoustic foam-wedges to absorb the transmitted sound down to 190 Hz. The floor and ceiling of the test-section are comprised of 0.61-m square metal perforate panels covered by Kevlar, and backed by acoustic foam-wedges. This facility can achieve speeds up to 80 ms^{-1}, and the flow in the empty test-section is closely uniform, with a free-stream turbulence intensity of 0.016% at 12 ms^{-1} that increases to 0.034% at 57 ms^{-1}. An exchange tower behind the fan is used to regulate the temperature in the tunnel with the atmospheric ambient. The detailed aerodynamic and aero-acoustic performance of this facility has been documented by Devenport *et al.* (2013).

2.2. *Body of Revolution (BOR)*

The Body-of-Revolution (BOR) geometry, shown in figure 1, was inspired by prior work on a body-of-revolution with an aft-ramp designed to have a Stratford-Smith pressure distribution (that corresponds to a boundary layer constantly on the verge of separation) (Hammache *et al.* 2002). The BOR was chosen to have a characteristic length of $D = 0.4318$ m, with a fore body comprised of a 2 : 1 semi-ellipsoid nose and a constant diameter cylindrical section, with a 0.8 mm trip-ring sandwiched at $x/D = 0.98$. The coordinate frame used throughout this paper is shown in figure 1, and has an origin at the nose, with x-axis along the BOR axis of symmetry, y-axis pointing vertically upward, and the z-axis towards the port-wall, completing a right-handed system. The aft-ramp of the BOR is a cone joined to the constant-diameter section through a sharp corner. Steady Reynolds Averaged Navier Stokes (RANS) calculations and surface oil flow visualization on a quarter-scale BOR – that set the half-apex angle at 20° – were used to ensure that the boundary layer would decelerate as rapidly as possible without separating. The tail-cone was truncated at $x/D = 3.172$, with a local radius of $0.073D$, to facilitate the installation in the wind tunnel.

The BOR was fabricated in-house, and is hollow, with the shell made from concentric rings of rigid-polyurethane tooling foam, supported internally by Aluminum 6061 bulk-heads on either side of the constant-diameter section. The outer surface was smoothed and spray-painted to ensure a seamless skin that is opaque to the flow. The entire assembly, weighing 55 kg, was suspended at the center of the test-section with a variable-tension tether system, and positioned by a downstream shaft, resulting in a net blockage of 4.3% (see figure 2(a)). The tether system consisted of cruciform tethers that were cleated to the fore-bulkhead inside the body, just downstream of the trip ring, forming clean, sealed, cylinder-body junctions at the points where they entered the body. These tethers ran diagonally across the test-section, tensioned by manual linear stages just outside the ceiling on either sides, and stabilized by 14.4 kg steel blocks on the floor side. The angle between the tethers was close to 90°, allowing precise adjustment of the body angle-of-attack. The tethers, initially 1.6 mm steel cables, were upgraded to 0.9 mm ones over the course of experiments. The restricted influence of these tethers on the BOR turbulence, documented with a single hotwire anemometer, is summarized here and described in § 3.1. The tether wakes, measured outside the BOR boundary layer at the tail-cone end, were about 10° wide and appeared mild, with a peak velocity deficit and turbulence intensity of 5% and 1.5% of the free-stream velocity. More importantly, the mean velocity and turbulence intensity profiles of the BOR boundary layer at the tail, directly downstream of the wakes showed no explicit variation from the other circumferential stations, suggesting a constrained if not negligible impact of the tethers. In any case, both the surface pressure and the velocity measurements were made at circumferential stations furthest away from the tether wakes to ensure the minimum influence.

The hollow shaft used to position the BOR at the downstream end was flush to within 1-mm with the outer-skin at the BOR tail, and was connected to a streamlined strut on the downstream end. The shaft was 0.91 mm long, with the length set through potential flow calculation, to restrict the inviscid perturbation of the streamlined strut at the BOR tail to within 0.5% of the tunnel free-stream velocity. Further, the downstream strut was streamlined (with polystyrene and sheet-metal) to a McMaster Henderson airfoil to minimize the trailing edge shedding (see Glegg & Devenport 2017, pg. 253).

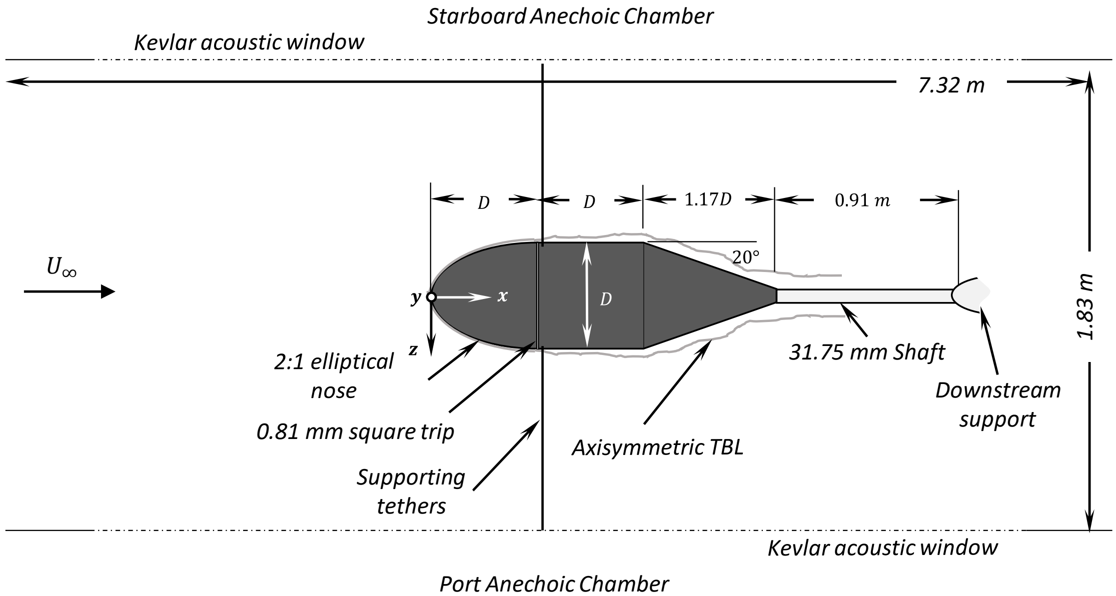

Figure 1: Schematic of the top-view of the test-section, showing the BOR geometry and experimental arrangement.

2.3. *Steady pressure measurements*

Steady pressure measurements were made to examine the circumferential uniformity and document the axial distribution of the surface pressure. 85 half-millimeter diameter pressure taps were embedded into the body of revolution: 51 ports measured the streamwise distribution of the mean surface pressure, and 36 ports measured the circumferential uniformity on the nose at $x/D = 0.095$ and 0.5 (figure 2(b)). The pressure signal was sampled at 100 Hz, via Tygon tubes, by a DTC Initium ESP-32HD acquisition system (range = 10 in. WC range, accuracy = $\pm 0.05\%$). The body was installed at $0 \pm 0.25°$ angle of attack by iteratively adjusting the position with the tether system, until the pressure measured by the circumferential arrays were uniform. The free-stream static pressure, stagnation pressure and velocity were measured from pressure taps in the wind-tunnel contraction and settling chamber 2.51 m upstream from the test-section leading edge. A thermocouple in the diffuser measured the ambient temperature.

To further confirm the circumferential uniformity, the stagnation pressure distribution at the BOR tail ($x/D = 3.172$) was measured with a custom built Pitot-probe rake. The rake consisted of a radial line of 119, 0.5 mm diameter pitot probes positioned across the wake diameter from $r/D = 0.12$ to 0.3 on either side of the sting support (figure 2). The rake was rotated about the x-axis to 36 angular stations resolving the body of revolution wake profile, including the tether wakes. An Esterline 98RK-1 NetScanner system with range = ± 10 in. WC and accuracy = 0.05% was used to measure the stagnation pressure.

2.4. *Turbulent velocity measurements*

Measurements of the turbulent velocity were made at a Reynolds number $Re_L = U_\infty L/\nu$ of 1.90x10^6, where U_∞ is the tunnel free-stream velocity and $L(= 1.3695\text{-m})$ is the BOR length. U_∞ was nominally 22-ms^{-1}, and was varied in order to maintain a constant Re_L (to within 2%) as the tunnel temperature drifted. Measurements were made using a combination of constant-temperature hotwire-anemometry and particle image velocimetry (PIV), as summarized in figure 3. The inflow to the APG ramp was

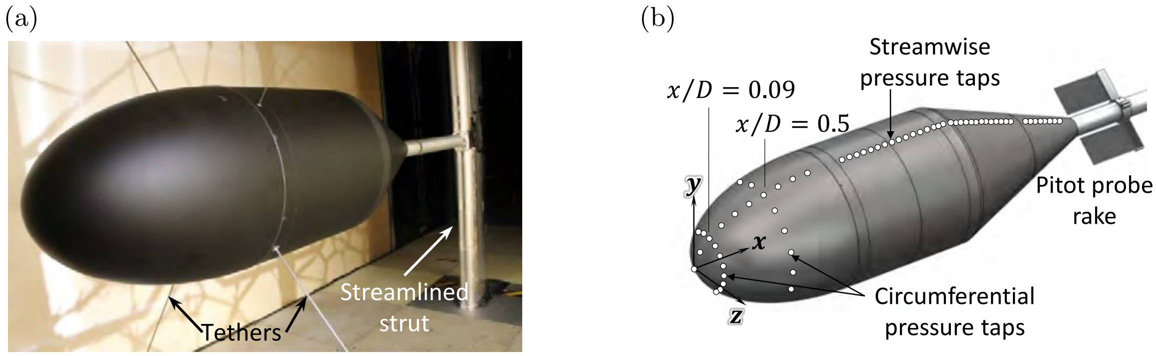

Figure 2: (a) Photograph of the BOR installed in test-section of Virginia Tech Stability Tunnel (b) Arrangement of 85 pressure taps on the body: 52 ports measuring the streamwise distribution, and 36 ports measuring the circumferential uniformity.

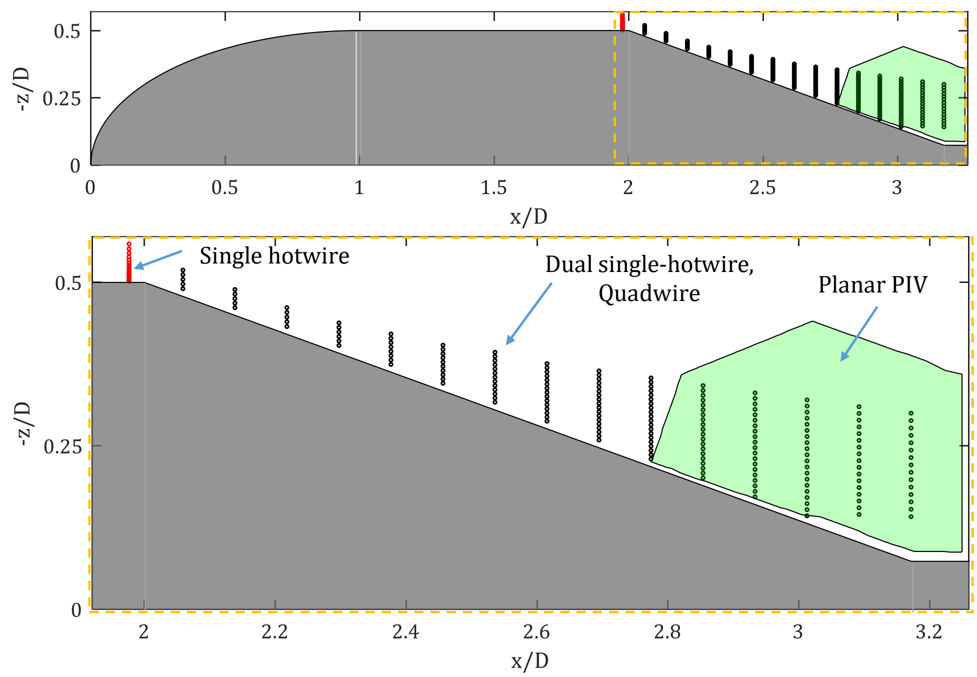

Figure 3: Schematic showing the various measurements of the turbulent velocity over the Body-of-Revolution.

measured upstream of the corner, at x/D=1.977, with a single hotwire anemometer, obtaining the single-point statistics and spectra; The streamwise evolution over the ramp was documented first by two single hotwires, followed by a four-sensor hotwire, acquiring 15 profiles for each, between x/D = 2.0 to 3.172, obtaining the statistics and temporal structure; Furthermore, a subset of the two-point space-time structure of the streamwise velocity at the BOR tail were made with two single wire probes, obtaining the radial and circumferential correlations at x/D=3.172. These measurements were supplemented by non-time-resolved, planar PIV, covering the rear-third of the ramp x/D=2.80 to 3.172, documenting the spatial structure of the ramp flow. Further information detailing the setup, acquisition and post-processing is discussed below.

2.4.1. *Constant temperature hotwire anemometry*

The inflow to the ramp was measured by a single-sensor hotwire manufactured by Auspex Corporation (type AHWU-100, with tungsten wire of length 1.2-mm and diameter 5-μm), documenting the streamwise velocity and turbulence intensity over a 30-point profile, at a single circumferential station upstream of the corner, at x/D=1.977 (figure 3). Similar measurements were made over the ramp using two similar single-sensor hotwire probes, separated by 18.5-mm along a 9.3° inclination to the body axis (figure 4(a)), while they were traversed over 15 streamwise stations on the ramp (x/D = 2.059 to 3.172). While this separation ensured the upstream probe was free from downstream probe interference – providing clean single point statistics – the dual probe arrangement was used to derive the turbulence convection velocity. The mean velocity and streamwise Reynolds stress from the upstream probe were validated against the PIV results described in § 2.4.2. The probes were calibrated frequently in the wind tunnel to account for the temperature variation, and corrections were made following the procedure of Bearman (1971). Though the statistical random uncertainty (for 20:1 odds) is acceptable at about 0.5% U_∞ for the mean velocity and 2%U_∞ for the turbulence intensity, the bias error from rectification and axial sensitivity could be significant especially near the wall, given a highly turbulent flow (Tutu & Chevray 1975). For example, as observed by Tutu & Chevray for a local turbulence intensity of 0.3 – which exist along the ramp in only the lower 10% of the boundary layer – the mean velocity can be overestimated by upto 3% and turbulence intensity can be underestimated by upto -5.7%; Therefore the near-wall results must be interpreted with special care.

Additionally, three-component velocity and six-component turbulence stress were measured with a four-sensor hotwire probe, with a measurement volume of 0.5-mm^3, manufactured by Auspex Corporation (type AVOP-4-100). Measurements were made precisely at all the points where the upstream single wire sensor was traversed, enabling cross-validation. The construction, angle and velocity calibration, and validation of the probes are discussed by Wittmer *et al.* (1998). While the mean velocity were found to be in agreement with PIV results the turbulent stresses were inconsistent, as expected from quad-wire limitations due to rectification and gradient errors, and are excluded from analysis. Furthermore, quadwire estimates are ignored at all positions with turbulent intensity greater than 20% (typically in the lower 40% of the boundary layer) due to significant bias from rectification and axial sensitivity; For example, for a cross-wire the errors were over 2.7% and -4% in the mean velocity and turbulence intensity respectively (Tutu & Chevray 1975).

The correlation structure of the boundary layer was measured at the BOR tail (x/D = 3.172) with two single hotwires, in the anchored probe - moving probe arrangement, shown in figure 4(b,c). Radial and circumferential correlations of unsteady streamwise velocity were measured at four anchor points in the boundary layer (40, 65, 75, 85% of boundary layer thickness from the surface). Furthermore, the radial correlations were consistent with planar PIV results, suggesting negligible probe interference even at small-separation.

All hotwire measurements were made in a horizontal plane (x - z) passing through BOR axis, away from the tether wake regions, with Dantec 90C10 Constant Temperature Anemometer (CTA) modules on a Dantec Streamline 90N10 frame with a flat response upto 10-kHz. The probes were positioned by a computer-controlled three-axis traverse system with a 0.0125-mm resolution. A National Instruments device (NI DAQ 9225-9191) sampled the anemometer output at 50 kHz obtaining 50 ensembles with 8192 samples

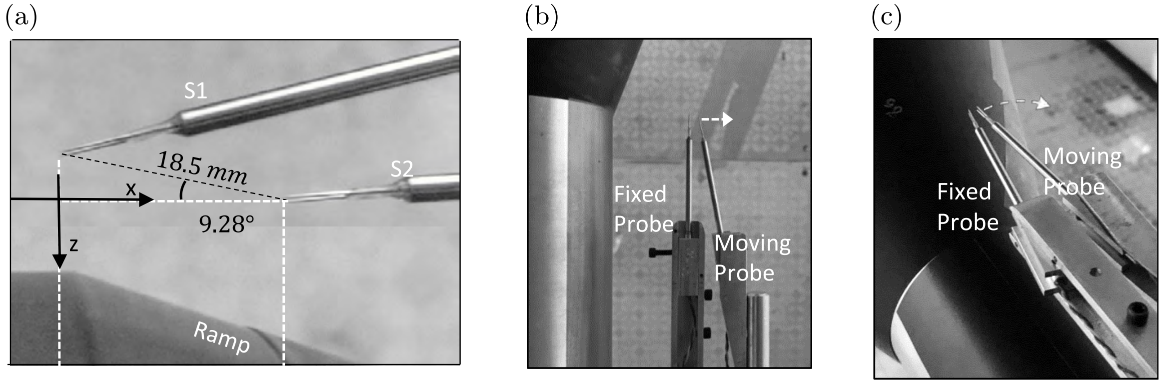

Figure 4: Velocity measurements on the BOR ramp with single hotwire (a) Dual probe arrangement on ramp to measure the single point statistics and large-scale convection velocity. (b) Radial correlations at the BOR tail ($x/D = 3.172$) measured with a moving and fixed single hotwire. (c) Arrangement to measure circumferential correlation at the tail.

in each. Ambient conditions including the tunnel inlet velocity, ambient pressure and temperature were acquired synchronously with hotwire measurements.

2.4.2. *Particle Image Velocimetry*

Planar PIV measurements were made over the rear $1/3^{rd}$ of the BOR ramp ($x/D =$ 2.80 - 3.17, see figure 3) to obtain the spatial structure of the turbulence non-intrusively, supplementing the hotwire measurements. The flow was seeded by a LaVision Aerosol Generator which atomizes Di-Ethyl-Hexyl-Sebacat (DEHS) liquid to produce particles on the order of 1 μm in diameter. The Stokes number for these particles in the low speed flow is much less than one, even for the smallest scales of interest. A Quantel Evergreen (EVG00200) double-pulsed 532-nm Nd-YAG laser pulsing at 7-Hz, illuminated the seed particles in the horizontal (x–z) plane passing through the BOR axis, shown in figure 5. A LaVision collimator along with a plano-convex lens of -50-mm focal length were used to shape the laser beam into a sheet. The region on the BOR illuminated by the laser was spray-painted with Kiton Red 620 dye to minimize the laser flare. Two LaVision Imager sCMOS cameras, each with a Sigma EX 105mm 1:2.8D DG Macro lens, were positioned in tandem outside the flow and synchronized with the laser pulses using a LaVision programmable timing unit, acquiring 6,000 image pairs. The dual cameras provided a combined larger field-of-view (with a 50% overlap) and were stitched during post-processing. A total of 4 such measurement sequences were used to capture the spatial structure over the rear-third of ramp. The raw images were processed in DaVis 8.4 with a 32 x 32 pixel interrogation window, yielding a vector field with 2-mm spatial resolution.

3. Results and Discussion

Results are discussed in the co-ordinate system (x, y, z) shown earlier in figure 1. The mean velocity along x, y, z axes will be identified by U, V, W respectively, with U_s implying the velocity in the main streamwise direction. The corresponding unsteady velocities are referred in the lower case - u, v, w and u_s. The tunnel reference velocity at the test-section inlet is U_∞. In the corresponding cylindrical co-ordinate system (x, r, θ), r is the radial distance from the x-axis and θ is the polar angle, measured from the vertical

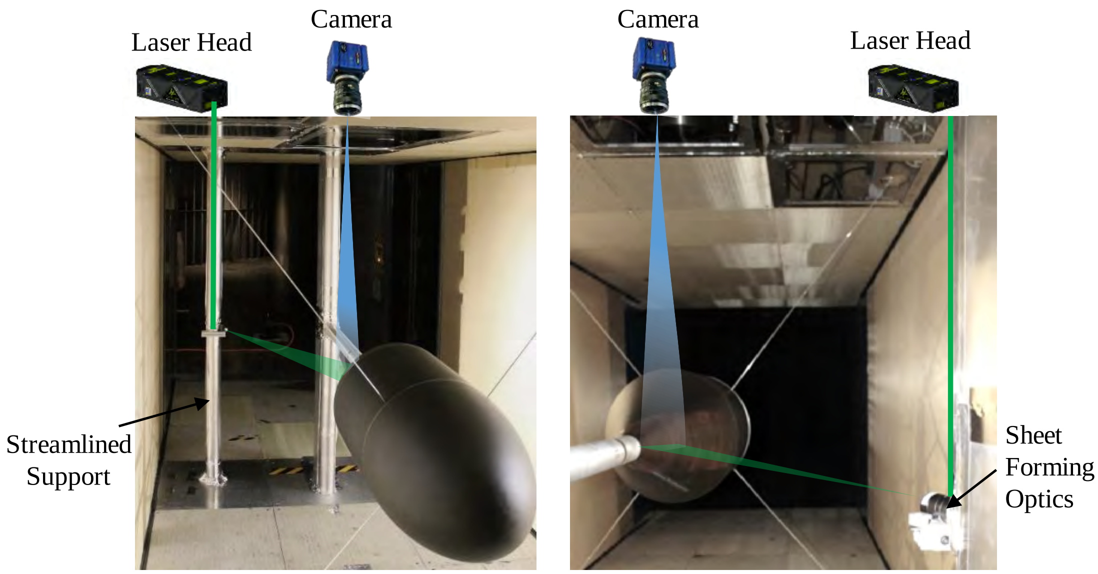

Figure 5: Setup for PIV measurements on the tail cone. Laser sheet - pulsed from a sufficiently downstream station - illuminated the tail cone boundary layer, and a single camera mounted directly above the field-of-view was traversed along the ramp.

(y-axis) by the right-hand rule. By such a convention, all measurements discussed from § 3.3 onwards were made at $\theta = 3\pi/2$.

3.1. *Axial symmetry, impact of tethers and trip height*

The axial symmetry of the flow was examined at two axial stations, in different flow quantities; Upstream, on the nose ($x/D = 0.5$), mean surface pressure was examined; Downstream, at the BOR tail ($x/D = 3.17$) stagnation pressure, mean velocity and turbulence intensity were examined. The circumferential ring of surface pressure taps on the nose ($x/D = 0.5$) suggested a residual $\pm 0.25°$ angle of attack. Contours of the stagnation pressure coefficient (C_{p_o}) at the BOR tail are shown in figure 6(a,b). Here $C_{p_o} = (p_o - p_\infty)/(p_{o,\infty} - p_\infty)$ where p_o is the stagnation pressure in the wake, $p_{o,\infty}$ is the stagnation pressure of the ambient free-stream, p_∞ is the static pressure of the tunnel ambient. Outside the wakes from the upstream tethers C_{p_o} is axisymmetric, varying within 9% from the circumferential average, with a standard deviation of 5%. Similarly, uniformity in both the mean velocity and turbulence intensity at the BOR tail were examined with a single hotwire, over a 200 point-grid spread across 15 radial profiles covering a quadrant (+y, +z). The mean velocity was axisymmetric to within 2% of the circumferential mean, and the turbulence intensity was axisymmetric to within 7%. Note that the tether wakes shown in figure 6 correspond to the original 1.6-mm tethers which were upgraded to 0.9-mm over the course of experiments. The wakes of upgraded tethers, measured outside the BOR boundary layer at $x/D = 3.17$, were found to be about 10° wide and were mild, with a $0.05U_\infty$ peak velocity deficit, and $0.015U_\infty$ peak turbulence intensity. Additionally, the impact of these tethers on the BOR boundary layer seems constrained, if not negligible, since the boundary layer velocity and turbulent intensity at the BOR tail, directly downstream of the tethers, indicated no explicit variation from the other circumferential stations. Regardless, all turbulence measurements, discussed in subsequent sections were made at a plane furthest away from the tethers ($\theta = 3\pi/2$).

The sensitivity of the flow to trip height was examined, by replacing the original 0.8-

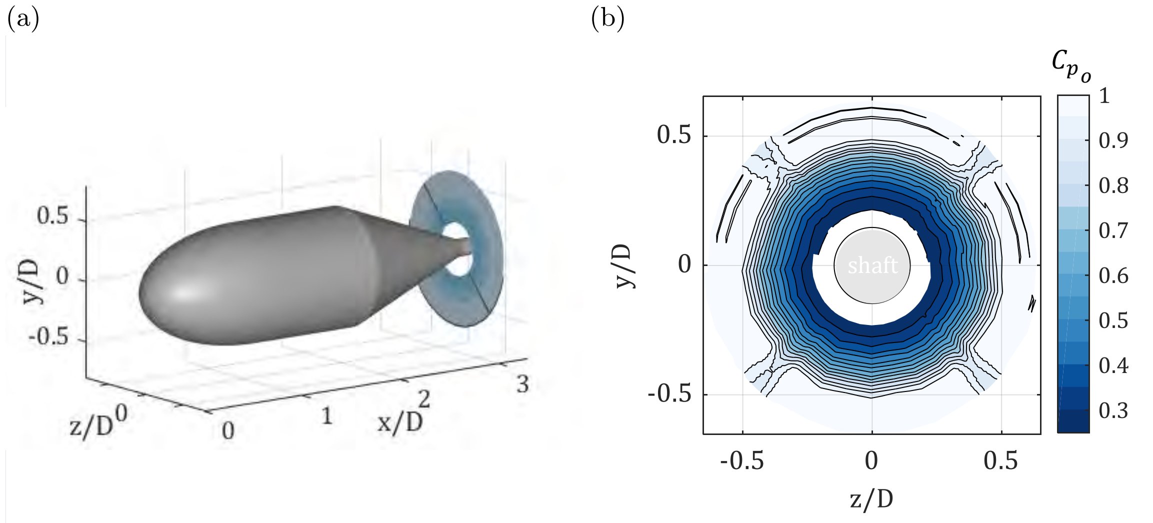

Figure 6: (a) Schematic showing the location of stagnation pressure cross-section measured to verify circumferential uniformity. (b) Contours of stagnation pressure coefficient (C_{p_o}) at BOR tail verifying circumferential uniformity.

mm one with a trip double the height, and comparing the stagnation pressure profiles at the BOR tail: The resultant wake was slightly stronger, with roughly 9% lower C_{p_o}, suggesting the turbulence structure is not overly sensitive to the trip.

3.2. *Characteristics of the inflow to the APG ramp*

The streamwise variation of mean pressure along the body is shown in figure 7. Estimates of the static-pressure coefficient (C_p) are consistent with potential flow calculations (using a doublet panel method for a body of revolution) and in turn with numerical simulations (Wall-modelled large eddy simulation, from Zhou *et al.* (2020)). The flow accelerates over the nose, passing the trip ring sandwiched between the nose and the constant diameter mid-body. Further downstream, the sharp corner between the mid-body and ramp generates an intense local acceleration as the flow enters the ramp. Hereafter, the flow decelerates rapidly over the 20° tail cone, with the boundary layer resisting a strong adverse pressure gradient.

The boundary layer approaching the ramp has been documented to understand the initial conditions for the APG region. The mean velocity and turbulence intensity about 10-mm upstream of the corner (x/D=1.977), sampled by a single hotwire, are shown in figure 8 (a,b). Here, vertical axis represents the position (z) relative to the surface (z_s), scaled on the BOR diameter, while the horizontal axis reveals the corresponding mean velocity (figure 8 a) and turbulence intensity (figure 8 b). Generally, the mean velocity (U_s) is higher compared to the tunnel inlet velocity due to the acceleration past the nose, and does not fully asymptote to a constant due to the local acceleration and curvature induced by the downstream corner. The boundary layer thickness – defined as the location from the surface with a turbulence intensity of 2% – is 7.8-mm, and is thin relative to the local radius (δ/r_s=0.04). The peak measured turbulence intensity is about 9%, occuring at 0.07δ from the surface and decays on moving further away. Additional characteristics of the layer such as the integral parameters are shown in table 1. The displacement and momentum thicknesses, δ_1 and δ_2 respectively, have been estimated using the planar definitions (equation 3.1), where the missing data very near the wall has been extrapolated by a cubic spline fit, constrained by a no-slip condition at the wall.

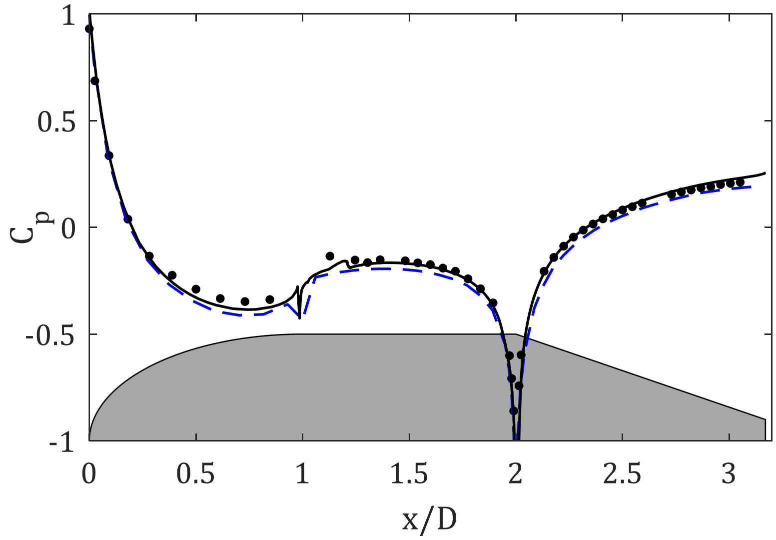

Figure 7: Streamwise pressure distribution on the BOR; (●) Measurement, - - - - Potential flow simulation, ——LES from Zhou *et al.* (2020)

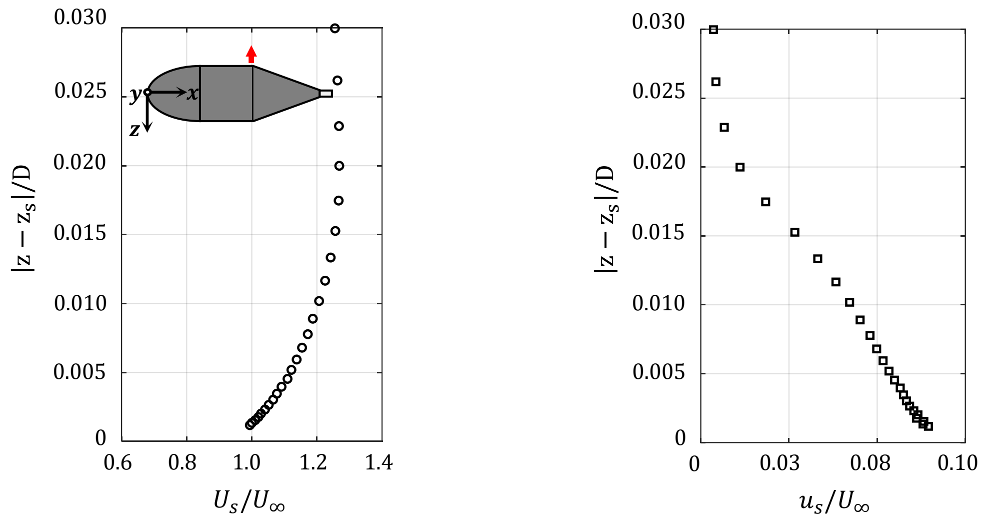

(a) (b)

Figure 8: (a) Mean velocity profile upstream of corner (x/D=1.977), U_∞ is the tunnel free-stream velocity (See table 1) (b) Turbulence intensity profile at x/D=1.977

The results were only mildly sensitive to the extrapolation process, varying within 5% of the spline estimates, when tried with linear, cubic, and quadratic extrapolations.

$$\delta_1 = \int_0^\delta (1 - U_s/U_e) d(|z - z_s|) \tag{3.1}$$

$$\delta_2 = \int_0^\delta (U_s/U_e)(1 - U_s/U_e) d(|z - z_s|)$$

Parameters	Tunnel inlet velocity	Edge velocity	Boundary layer thickness	Displacement thickness	Momentum thickness	Reynolds number	Curvature parameter
	U_∞ (ms^{-1})	U_e/U_∞	δ (m)	δ_1 (m)	δ_2 (m)	Re_{δ_2}	δ/r_s
	22.8	1.27	0.0078	0.0008	0.00053	926	0.04

Table 1: Boundary layer characteristics at inflow (x/D=1.977) to the BOR ramp

3.3. *Mean flow characteristics on the ramp*

Downstream of the corner, the mean flow decelerates significantly on the ramp with the boundary layer thickening, as seen from the streamwise mean velocity contours in figure 9. At the BOR tail (x/D=3.172) the boundary layer is 79.5-mm thick; growing about 10 times the thickness just upstream of the corner, over a distance of 1.2 D. The corresponding velocity at the edge of the boundary layer (U_e) decreases by over 40%, from $1.27U_\infty$ upstream to $0.89U_\infty$ at the tail. Despite such a strong deceleration, the flow is well-behaved, as seen from the velocity vectors in figure 9, diverging away from the wall and increasingly aligned with the BOR axis. The circumferential component in the outer region (0.4δ - 1.0δ) measured with a quad-wire was less then 5% of U_∞ in the first half of the ramp, decreasing to less than 2% towards the tail. This, combined with the circumferential uniformity in the stagnation pressure at the tail, indicates the flow has no appreciable swirl, and therefore is two-dimensional.

The flow appears to be out-of-equilibrium, as seen from the downstream evolution of boundary layer characteristics, shown partially in figure 10 (a-c) with full details in table 2. Note that all integral parameters have been estimated by integrating radially-outward instead of perpendicular to the surface; This is not expected to alter the interpretation of any result but may change the obtained factors through a simple co-ordinate transformation. The displacement thickness, shown in figure 10(a), (estimated according to equation 3.1), increases relative to the boundary layer thickness from 0.2δ to 0.5δ, suggesting a stronger wake component downstream and the corresponding shape-factor H ($=\delta_1/\delta_2$), shown in figure 10(b), increases by over 50%, from 2.14 upstream to 3.24 at the tail. The associated momentum thickness based Reynolds number Re_{δ_2} (table 2) rises by an order of magnitude, from some 2000 upstream to about 16,000 at the ramp tail. While the shear-stress at the wall was not measured, and since no universally accepted hypothesis exists to empirically estimate the value, we infer the trends in wall-friction from Reynolds-number matched LES of the BOR flow, borrowed from Zhou *et al.* (2020). Even after confirming the agreement in the mean surface pressure (figure 7), in the mean velocity as well as auto-spectra of unsteady surface pressure (refer to Zhou *et al.* (2020)), we rely on the estimates only for qualitative conclusions: here, that the skin-friction is not constant across the ramp (figure 10(c)). Therefore, a strongly varying H, Re_{δ_2}, and C_f suggest the non-equilibrium character of the flow, reminiscent of vehicle-relevant conditions.

The strength of the pressure gradient has been previously inferred from various parameters, with the most common being Clauser's $\beta_C = (\delta_1/\tau_w)dp/dx$ (Clauser 1954), where τ_w is shear stress at the wall; In our case, β_C (table 2) varies between 5 and 18, except at the tail ($\beta_C = -14.7$) due to the flow accelerating onto the support

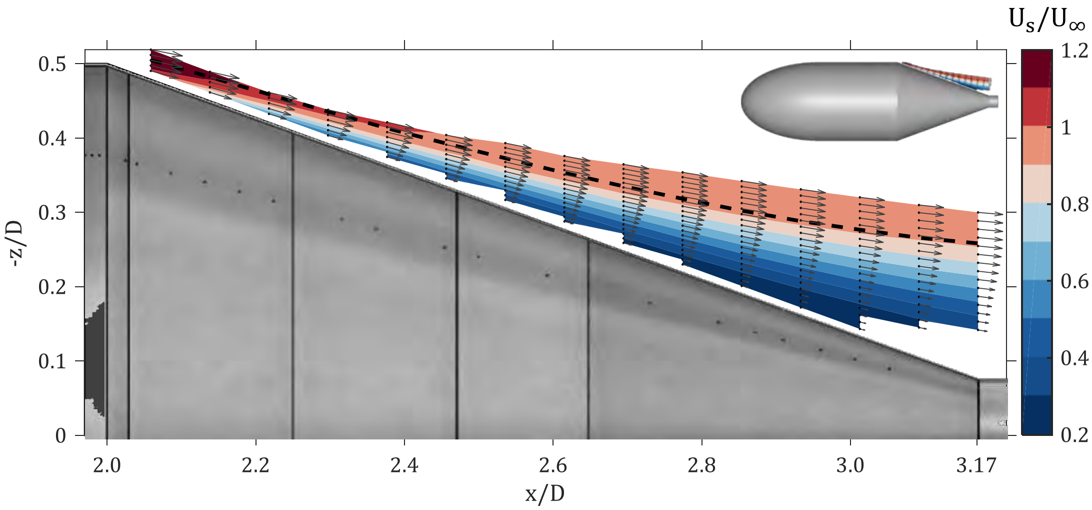

Figure 9: Contours of streamwise mean velocity (U_s) on the ramp from single hotwire measurements, scaled on the tunnel reference velocity (U_∞); Arrows at the measurement stations reveal the flow orientation as measured by quadwire. - - - - identifies the edge of the boundary layer. Inset to the top right shows the global position of the measurement.

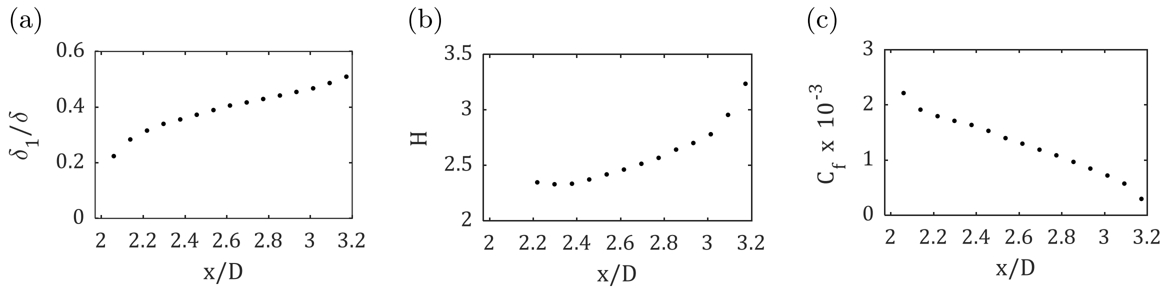

Figure 10: Characteristics of Boundary layer on ramp: (a) Displacement thickness (δ_1) as a fraction of the velocity thickness(δ) (b) Shape factor $H = \delta_1/\delta_2$ (c) Skin-friction coefficient (C_f) from LES Zhou *et al.* (2020)

shaft (see figure 1). However, β_C is not universally applicable, as it tends to infinity for separating boundary layers ($\tau_w \to 0$). More importantly, Maciel *et al.* (2018) argued that β_C and Re_{δ_2} do not form a consistent set of parameters that describe the flow; Specifically, these parameters have not been derived from the boundary layer equations using a consistent choice of length and velocity scales. As a remedy to this problem, they developed a set of parameters from the non-dimensional boundary layer equations, using a consistent choice of length and velocity scales, say L_o and U_o. The resulting parameters: $\beta_o = L_o/(\rho U_o^2) dp_e/dx$, $\alpha_o = U_e V_e/U_o^2$, and $Re_o = U_o L_o/\nu(U_o/U_e)$ were found to have a direct physical interpretation: they represented the ratio of the order of magnitude of forces, with the apparent turbulent force (Reynolds shear stress gradient) as the reference force. β_o, α_o and Re_o, represented the strength of the pressure gradient force, inertial and viscous force respectively, relative to the apparent turbulence force. Furthermore, on examining their DNS datasets, they observed that these parameters, with velocity scale $U_o = U_{zs} = U_e \delta_1/\delta$ and lengthscale $L_o = \delta$, accurately tracked the ratio of the forces. Here, U_{zs} represents the velocity defect of the bulk flow, first proposed by Zagarola & Smits (1998) for the pipe-flows, and later examined for APG layers first by Castillo & George (2001). The parameters β_{zs} and Re_{zs} on the BOR ramp, based on the

x/D	U_∞ (ms^{-1})	U_e/U_∞	δ (m)	δ_1 (m)	H $(=\delta_1/\delta_2)$	Re_{δ_2}	U_τ/U_∞	C_f	β_C	δ/r_s	${r_s}^+$
2.059	24.5	1.22	0.0114	0.0025	2.14	1981	0.0405	0.0022	5.0	0.06	11458
2.138	24.6	1.12	0.0140	0.0040	2.38	2593	0.0347	0.0019	7.7	0.07	9291
2.218	24.6	1.07	0.0164	0.0052	2.35	3260	0.0320	0.0018	7.2	0.09	8025
2.297	24.6	1.03	0.0189	0.0064	2.33	3927	0.0301	0.0017	7.3	0.11	7048
2.377	24.6	1.00	0.0217	0.0077	2.33	4597	0.0286	0.0016	11.2	0.14	6222
2.456	23.7	0.98	0.0254	0.0094	2.37	5325	0.0272	0.0015	14.7	0.18	5332
2.536	23.2	0.98	0.0293	0.0114	2.42	6280	0.0259	0.0014	12.5	0.22	4635
2.615	23.0	0.96	0.0333	0.0135	2.46	7190	0.0245	0.0013	13.2	0.28	3976
2.695	22.8	0.95	0.0380	0.0158	2.51	8133	0.0231	0.0012	17.3	0.36	3357
2.774	22.7	0.93	0.0432	0.0186	2.57	9191	0.0218	0.0011	18.4	0.46	2791
2.854	22.6	0.92	0.0488	0.0216	2.64	10298	0.0203	0.0010	15.2	0.60	2266
2.933	22.5	0.92	0.0552	0.0251	2.70	11638	0.0189	0.0008	14.2	0.80	1782
3.013	22.5	0.91	0.0627	0.0293	2.78	13175	0.0173	0.0007	15.6	1.11	1344
3.092	22.4	0.91	0.0706	0.0343	2.95	14434	0.0154	0.0006	11.7	1.60	929
3.172	22.4	0.91	0.0798	0.0406	3.24	15661	0.0110	0.0003	-14.7	2.51	477

Table 2: Boundary layer characteristics on the ramp. C_f, U_τ are obtained from large eddy simulations on the BOR at matched Reynolds number (Zhou *et al.* 2020).

characteristics in table 2, are shown in figure 11(a,b). For reference, β_{zs} is co-presented with Castillo's pressure gradient parameter, $\Lambda = (\delta/(U_e d\delta/dx))dU_e/dx$ in figure 11(a), while Re_{zs} is shown with Re_{δ_2} in figure 11(b). Three observations can be made; First, the flow is confirmed to be out of dynamic equilibrium since the parameters, representing the ratios of the fluid forces, vary strongly across the ramp; Second, the pressure gradient is strong relative to the turbulent force ((pressure gradient)/(turbulent force) $\approx \beta_{ZS}$) and decays downstream on the ramp; Third, the turbulent force is stronger than the viscous force, even more so downstream, implying that the pressure gradient dominates both the turbulent and therefore the viscous forces.

While this non-equilibrium boundary layer over the ramp suffers a strong adverse pressure gradient, the effect of transverse curvature appears to be mild. δ/r_s is mostly less than 1 (table 2), implying boundary layer is thinner than the local radius of curvature (r_s) except near the BOR tail. The radius based Reynolds number, $r_s^+ = r_s u_\tau/\nu$, although initially high about 11000, decreases to 477 at the BOR tail. Following the observations Piquet & Patel (1999); Snarski & Lueptow (1995) such a range of parameters may affect the mean flow moderately, but are not expected to strongly influence the character of the turbulence. The flow, therefore, corresponds to that of a high Reynolds number, strongly decelerating flow over a large cylinder.

3.4. *Turbulence statistics on the APG ramp*

The streamwise evolution of Reynolds normal stress (u_s^2/U_∞^2), measured with a single hotwire, is contoured in figure 12. Consistent with previous studies, u_s^2 develop an 'outer' peak as the flow decelerates, which is centered initially about 0.4δ from the surface, drifting further away downstream, reaching $\sim 0.55\delta$ at the tail. However, contrary to most studies on *planar* APG boundary layers where the peak intensified with the pressure gradient, we observe the peak to relax downstream, even if normalized on the edge velocity (U_e). This can be viewed as a response to transverse curvature combined with a decreasing local pressure gradient (see figure 11a). In an LES study of a body-of-revolution flow, Kumar & Mahesh (2018) observed the turbulence intensity away from

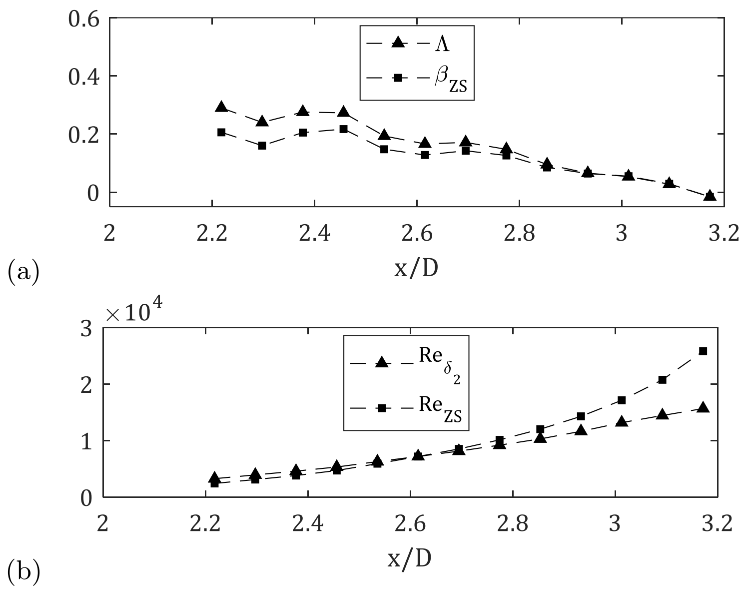

Figure 11: Flow parameters in APG region (a) Pressure gradient parameters, $\Lambda = (\delta/(U_e d\delta/dx))dU_e/dx$ and $\beta_{ZS} = (\delta/U^2{}_{zs})U_e dU_e/dx$ following the work of (Castillo & George 2001) and (Maciel *et al.* 2018) respectively. (b) Reynolds numbers, $Re_{\delta_2} = \delta_2 U_e/\nu$, and $Re_{Zzs} = U_{zs}\delta/\nu(U_{zs}/U_e)$.

the wall to decay faster than in a flat-plate flow under similar conditions, even for a modest δ/r_s of 0.3. This is also consistent with earlier work by Piquet & Patel (1999), who showed that the transverse curvature does not alter the turbulence production mechanism itself, but the reduction of turbulence activity compared to a planar boundary layer is merely due to a smaller surface area where the production occurs, and the corresponding vorticity per unit volume of the flow, introduced by this surface, is lower than in the planar boundary layer. However, if the stress profiles are scaled with the friction velocity, the expected trend of a magnifying peak is observed, suggesting that the turbulent motions responsible for the outer peak are not dictated by the near-wall shear-stress inducing motions.

The structure of the other in-plane Reynolds stresses, u_n^2 (resolved orthogonal to the streamline) and $u_s u_n$, is similar to that of the streamwise Reynolds stress discussed above. In fact, this is not just superficially true, since the various Reynolds stresses were found to be directly proportional to the in-plane turbulent kinetic energy, $E = 0.5(u_s^2 + u_n^2)$ through precise constants over the measured domain, as shown in figure 13. While the contours of E in figure 13(a) – obtained from planar PIV over the rear-third of the ramp – paint a picture consistent with the hotwire estimates of u_s^2 stress in figure 12, the ratios of u_s^2, u_n^2 and $u_s u_n$ to E, shown in figure 13 b, c and d, are invariant over the measured domain; u_s^2 and u_n^2 are consistently about $1.4E$ and $0.6E$, and the Reynolds shear stress $u_s u_n$ is invariant at $0.45E$. This behavior deviates only near the boundary layer edge, as seen about the white dashed line in figure 13(b,c), where u_n^2 dominates, as one might expect due to the oscillating turbulent – non-turbulent interface. In any case, apart from being a pleasant simplification in extracting the different components from just the TKE through simple RANS calculations, this is an interesting observation. While we do not have a definite explanation, there appears to be some sort of self-preserved structure of the turbulent motions, with a dominant, organized mode through which

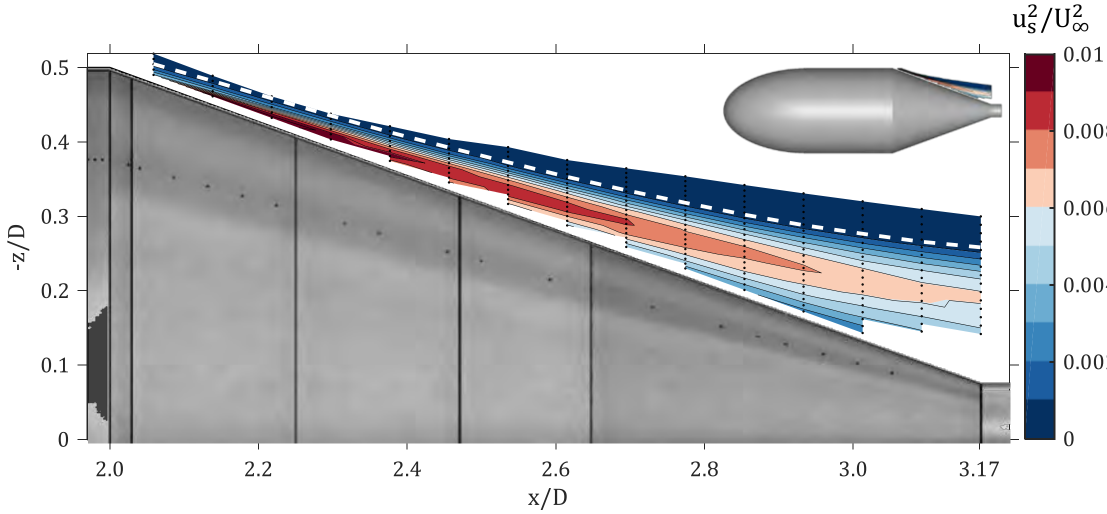

Figure 12: Contours of streamwise Reynolds normal stress on the ramp from single hotwire measurements, scaled on the tunnel reference velocity. Inset to the top right shows the global position of the measurement.

the streamwise turbulent energy is transferred into the other components. As a first step towards understanding this, we examine the mean flow and turbulence statistics for self-similarity in the following section, deriving the associated length and velocity scales, which will be further examined on the turbulence and correlation structure in subsequent sections.

3.5. *Self-similarity in the outer region along the ramp*

Figure 14(a,b) shows the profiles of streamwise velocity and Reynolds normal stress, obtained from single hotwire, that correspond to the contours in figures 9 and 12 discussed earlier. While the position from the wall is scaled with the boundary layer thickness, the mean velocity, figure 14(a), and turbulence stress, figure 14(b), are scaled with the edge velocity $U_e(x)$. Supporting the preliminary observations in § 3.3 - 3.4, the character of profile changes significantly as the flow decelerates downstream; The velocity deficit increases across the boundary layer and the outer peak in the Reynolds stress weakens as it drifts higher in the boundary layer, reaching 0.55δ at the tail. Much of this streamwise variation can be accounted for, when δ is replaced by δ_1 as the length scale, as shown in figure 15(a,b). In general, the mean velocity profiles form a tighter collapse while the Reynolds stress profiles realign such that the functional form, especially near the peak is somewhat consistent. Furthermore, the position of the outer peak is almost invariant at $(1.2 \pm 0.06)\delta_1$ (figure 15(c)) and we find that the mean velocity profiles suffer from an inflection point at this position. This is consistent with Kitsios *et al.*'s observation of an inflection point collocated with the outer turbulence peak, occurring at $1.3\delta_1$ and $1\delta_1$ for their mild ($\beta_C = 1$) and strong ($\beta_C = 39$) pressure gradient cases. Further confirming this, Maciel *et al.* (2018) observed the peak between $1.0 - 1.3\delta_1$ for a diverse range of numerical and experimental datasets of non-equilibrium layers. While the relationship between the outer turbulence peak and δ_1 is worth exploring, the success of the $U_e - \delta_1$ scaling is limited only to vicinity of the Reynolds stress peaks, as evident from the spread in the profiles at positions further away. On that note, by examining several scalings in the literature Maciel *et al.* argued that it is impossible to produce a complete collapse of the profiles, especially of the second-order statistics, and suggested the success of a

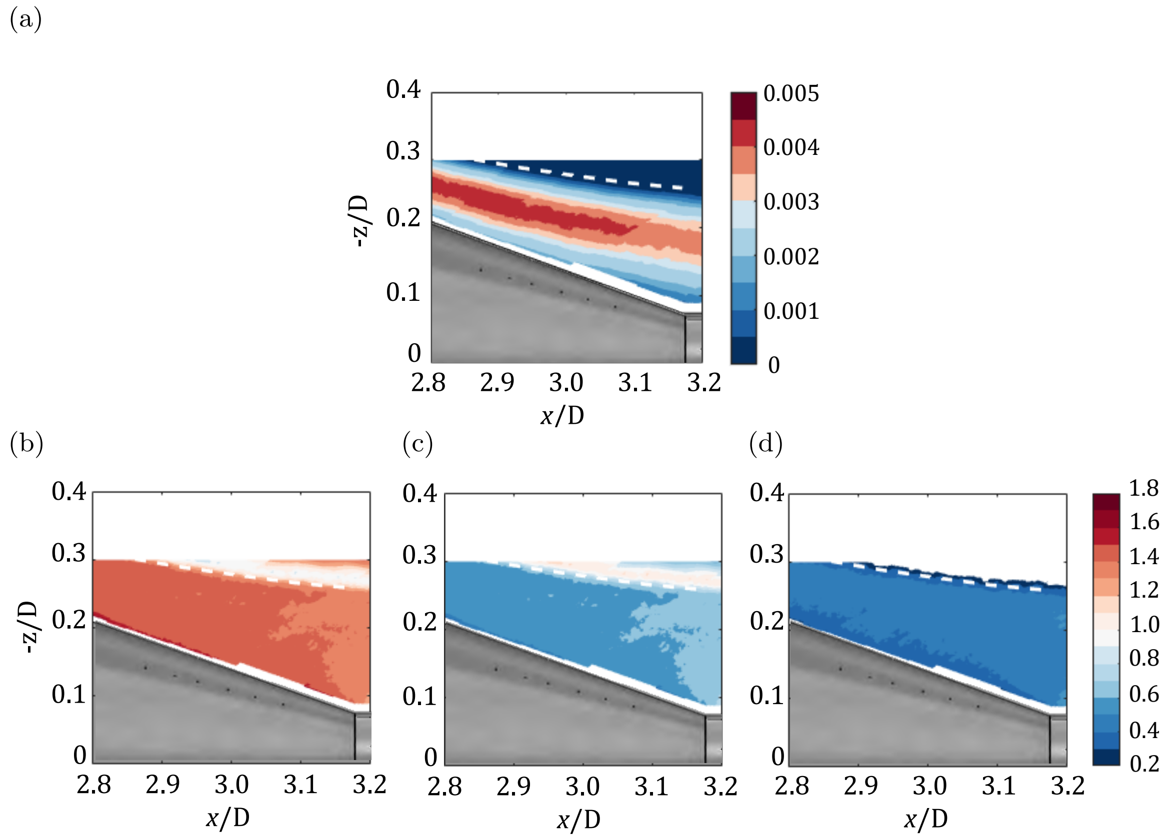

Figure 13: (a)Turbulence kinetic energy based on in-plane Reynolds normal stresses ($E/U_\infty^2 = 0.5(u_s^2 + u_n^2)/U_\infty^2$). (b) Ratio of streamwise normal stress to kinetic energy (u_s^2/E) ≈ 1.4. (c) $u_n^2/E \approx 0.6$. (d) $u_s u_n/E \approx 0.45$

scaling, over a broad range of APG, can only be judged by the order-of-magnitude of the resulting collapse. With such a view, they found $U_{zs} = U_e\delta_1/\delta$ and δ was the most successful scaling. Commonly referred to as the Zagarola-Smits scale, this scaling was originally proposed as an outer velocity scale for turbulent pipe flow by Zagarola & Smits (1998) and represents the bulk velocity defect of the flow. While Zagarola-Smits scaling may well be successful when considering a wide range of pressure gradients, for our relatively narrow spectrum of strong APG flow, the performance of $U_{zs} - \delta$ scaling is inferior to both $U_e - \delta_1$ and $U_e - \delta$ scalings. In any case, focusing on the larger picture, where we observe inflectional velocity profiles collocated with turbulence stress peak in the outer region, combined with a new peak in the turbulence production and transfer observed in other studies (Kitsios *et al.* 2017; Skåre & Krogstad 1994), suggests a fundamentally different mechanism for boundary layers under strong APG.

A promising proposal is that strong APG layers behave more like a free shear layer, developing inviscid instabilities in the outer regions, while the importance of near-wall turbulence weakens; For example, experimental studies by Song *et al.* (2000); Elsberry *et al.* (2000); Schatzman & Thomas (2017) as well as a numerical study by Kitsios *et al.* (2017) invoked the similarity with mixing layers. Through detailed investigation, Schatzman & Thomas gathered evidence for coherent spanwise-vorticity, centered about the inflection point. Via quadrant analysis of the shear stress profiles, they observed that the sweeping motions (Q4) were more frequent above the inflection point, while ejections (Q2) dominated below; At the inflection point both the motions were equally

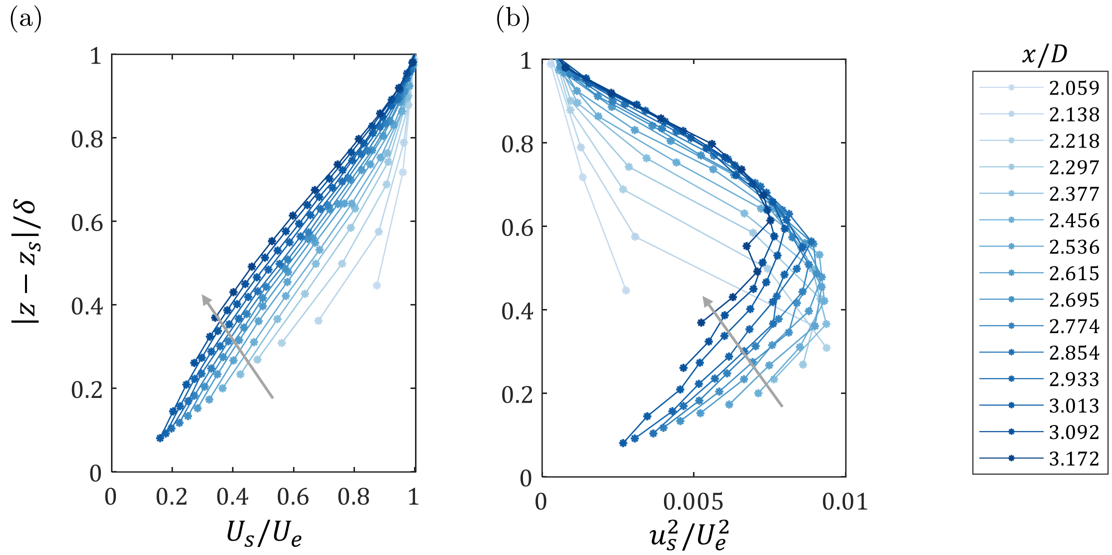

Figure 14: (a) Mean velocity profiles, with the vertical axis representing the distance from the surface scaled with δ and horizontal axis representing the velocity scaled with the edge velocity. (b) Profiles of the streamwise Reynolds stress with the $U_e - \delta$ scaling. Legend to the right shows the streamwise positions.

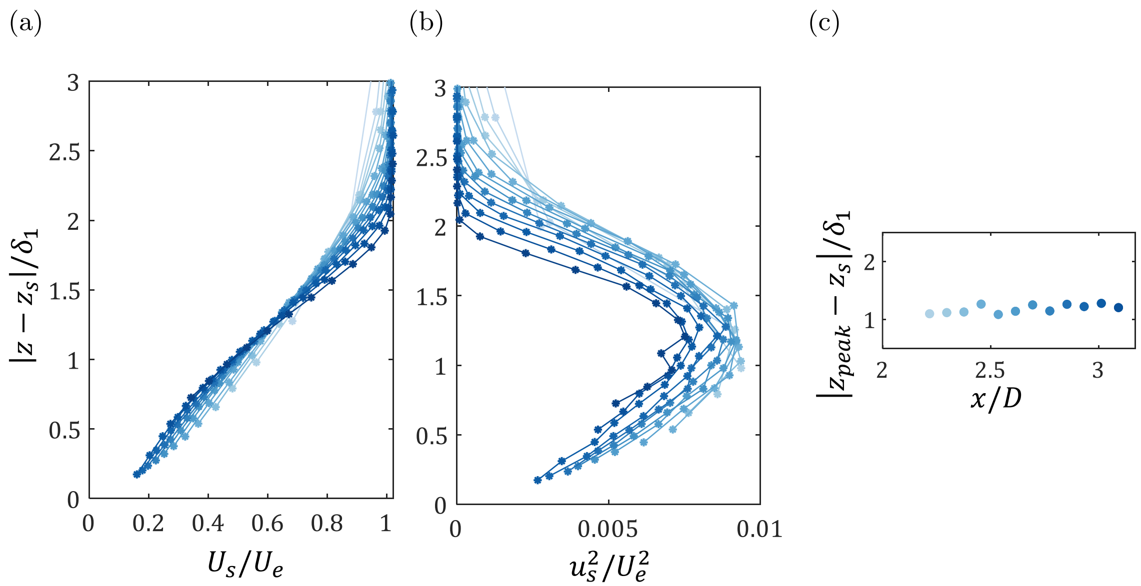

Figure 15: (a) Mean velocity profiles with $U_e = \delta_1$ scaling. (b) Profiles of the streamwise Reynolds stress with the $U_e - \delta_1$ scaling. (c) Location of the peak streamwise Reynolds stress scaled on δ_1. See figure 14 for legend.

likely. Invoking the Rayleigh-Fjørtoft theorem they attributed this observation to inviscid instabilities, and hypothesized an 'embedded shear layer' (ESL) in the boundary layer, centered about the inflection point. Inspired from self-similarity in free shear layers, they proposed the embedded shear layer scaling, with the length scale as the vorticity thickness,

$$\delta_\omega = (U_e - U_{IP})/(dU/dz)_{IP} \tag{3.2}$$

where IP refers to the outer inflection point and $(dU/dz)_{IP}$ is the slope of the velocity profile at the inflection point. The associated velocity scale is the velocity defect at the inflection point,

$$U_d = U_e - U_{IP} \tag{3.3}$$

With these length and velocity scales, and a co-ordinate system centered about the inflection point (equation 3.4), they observed the mean velocity and Reynolds normal and shear stress to collapse, despite not being in equilibrium.

$$\eta = (z - z_{IP})/\delta_\omega \tag{3.4}$$

$$U^* = (U_e - U)/U_d \tag{3.5}$$

For our case, the mean velocity and turbulence stress profiles with the ESL scaling are shown in figure 16(a,b). In order to minimize the numerical errors related to finding the inflection point, we centered the co-ordination system about the location of peak u_s^2. The velocity-defect profiles, figure 16(a), collapse well, and the functional form away from the wall ($\eta > -1$) is accurately described by the complementary error function (*1 - erf(η)*), which is commonly used for planar mixing layers. But, the collapse in the turbulence stress profiles, figure 16(b), appears no better than the $U_e - \delta_1$ scaling, particularly on the low-speed side ($\eta < 0$, figure 15(b)). However, a lack of any immediately obvious trend in the spread suggests significant uncertainty, arising from the discretized profiles used to estimate the scaling. Despite a wide spread, the peak magnitude of the turbulence intensity $\sqrt{u_s^2}$ is centered about 0.023 U_d, close to the 0.021 observed by Schatzman & Thomas.

Examining the shear layer parameters, we observe the vorticity thickness δ_ω to grow almost linearly along the ramp (figure 16(c)), at a rate $d\delta_\omega/dx \approx 0.046$, in the range commonly observed in free shear layer studies (such as Oster & Wygnanski (1982)). Furthermore, consistent with the condition for similarity, we observe that the embedded shear layer length and velocity scales are proportional to the boundary layer thickness and edge velocity respectively as,

$$\delta_\omega/\delta = U_d/U_e = 0.4 \pm 0.05 \tag{3.6}$$

While these observations certainly advocate the success of embedded shear layer scaling for an axially-symmetric boundary layer, some fundamental questions remain open, as described in § 1 and summarized here. The idea that the instantaneous flow can feel the mean velocity profile, and therefore the inviscid instabilities from inflection points is debatable. While Schatzman & Thomas observe the Rayliegh - Fjørtoft theorem to be valid for their flow, which is regarded a necessary and sufficient condition for inviscid instability, Maciel *et al.* (2017) in their DNS study could not deduce any coherent structures relevant to inviscid instability, in their sharply decelerated boundary layer. Additionally, the hypothesis is inconsistent with the observation of an outer turbulence peak despite the absence of inflectional profiles. One could therefore speculate that inflectional velocity profiles and the amplified turbulence activity in the outer regions are just correlated without sharing a cause-effect relationship. Further investigation into this aspect is needed before the scaling can be definitively attributed to inviscid instabilities. Subsequently, some work is also needed to develop a rigorous framework for strong APG layers. We must establish the conditions under which the ESL scaling is valid, and how this ties into the layer structure of the boundary layer including the near-wall layer.

While the questions raised above must certainly be addressed to illuminate the fundamental physics and develop a rigorous framework for strong APG layers, we are interested

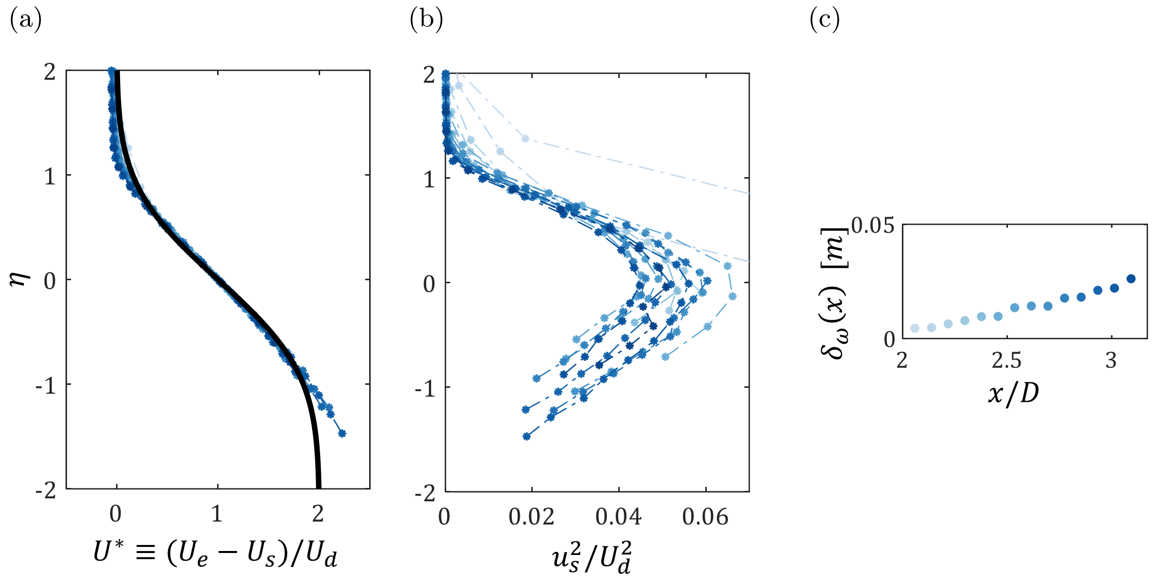

Figure 16: Embedded shear layer scaling for mean flow. (a) Mean velocity defect profiles, with (——) representing the complementary error function, 1-erf(η). (b) Streamwise Reynolds normal stress profiles (c) Streamwise growth of vorticity thickness (δ_ω) of the shear layer. See figure 14 for legend.

in the examining the turbulence structure and the implications of the shear layer scaling on the length and time-scales of the turbulence. This is expected to provide significant input for the aeroacoustic predictions where the integral length scales and the turbulence quantities are a direct input to the estimate the far-field spectrum, for example when a fan is ingesting the boundary layer.

3.6. *Turbulence structure of streamwise velocity*

The spectral structure of streamwise turbulence along the ramp, measured with a single hotwire, is shown at representative axial stations in figure 17(a-d). In each figure, contours of the pre-multiplied spectra $f'G_{u_s u_s}/U_\infty^2$ are presented, with the vertical axis showing the position in the boundary layer in terms of δ, and the horizontal axis showing the frequency normalized with the reference scale $f' = fU_\infty/D$. In general, the structure of the turbulence resonates with the character of the Reynolds stress profiles discussed in § 3.5. At all locations on the ramp, the most active region, across the frequency range, is centered about the outer turbulence peak that drifts further away from the wall downstream (following the dashed line from figure 17 (a) to (d)). Consistent with the stress profiles the peak level reduces downstream, by about 30%, from over 0.0025 upstream (x/D=2.3) to just over 0.0018 at the BOR tail (x/D=3.17). Furthermore, the approximate centroid of the active region shifts to lower frequency, sliding from $f' \sim 7$ at x/D=2.3, figure 17(a), to $f' \sim 1.8$ at x/D=3.17, figure 17(d), suggesting an amplification in the low-frequency motions in the outer region. This amplification of the large-scale motions can be visualized clearly by comparing the structure at each axial station, with that at a reference station, say at the BOR tail, as shown in figure 18. Here, the turbulence structure at various upstream stations (figure 17(a,b,c)) is scaled with that of the BOR tail (figure 17(d)), with the contour level representing the ratio of the spectra in dB-scale. Compared to the BOR tail, the energy is generally weaker at low frequency (blue contours) but stronger at higher frequency (red contours). This

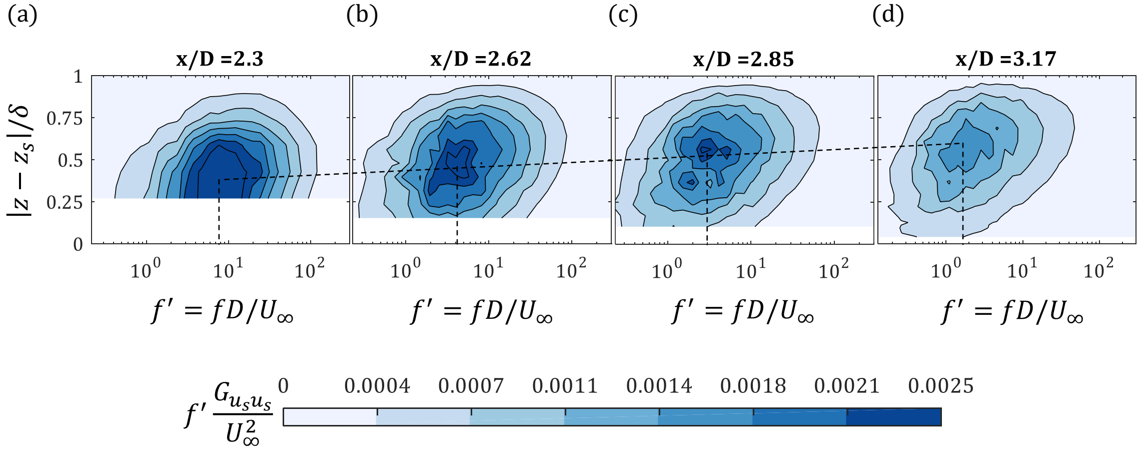

Figure 17: Contours of the pre-multiplied spectra of the streamwise velocity, $f'G_{u_s u_s}/U_\infty^2$, at representative streamwise stations on the ramp. Frequency $f' = fD/U_\infty$, where D is body diameter (D = 0.4318 m) and U_∞ is tunnel free-stream velocity. (a) $x/D = 2.3$ (b) $x/D = 2.62$ (c) $x/D = 2.85$, (d) $x/D = 3.17$. Dashed lines indicate the position of the peak levels, relative to the surface, and the corresponding frequency.

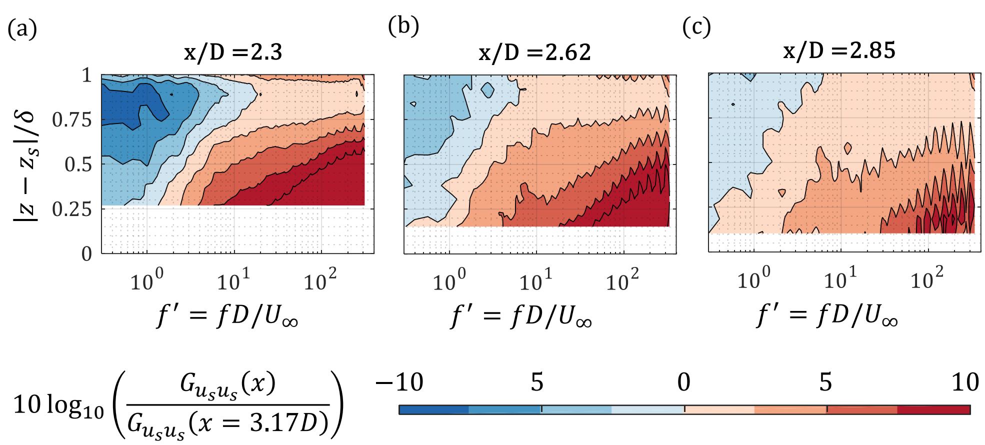

Figure 18: Comparison of the turbulence structure at various upstream stations, with that at the downstream BOR tail (x/D=3.17). Contours level represent the ratio of the pre-multiplied power spectra to that at the BOR tail, on a dB-scale. (a) $x/D = 2.3$ (b) $x/D = 2.62$ (c) $x/D = 2.85$

difference intensifies upstream, with the maximum difference on the order of 10-dB at x/D=2.3. For example, in figure 18(a), at $z - z_s$=0.25δ, the energy is lower for $f' < 2$ and higher for $f' > 2$, by over 10-dB. While this amplification of the large-scale motions is a generic feature of APG flows (Harun *et al.* 2013), the presence of lateral curvature is expected to further assist the amplification, as observed by Snarski & Lueptow (1995).

Figure 19(a-d) shows the turbulence structure plotted in terms of the ESL scaling. When the premultiplied spectra are plotted in the ESL coordinate system as $f'G_{u_s u_s}/U_d^2$ where $f' = f\delta_\omega/U_e$, the spectral structure appears similar along the ramp. Here U_d is chosen as the velocity scale, δ_ω/U_e is chosen as the timescale since $U_e \propto U_d$ (equation 3.6). The success of the ESL scaling was found to be superior to other related timescales δ/U_e, δ_1/U_e and δ/U_{zs}. The geometrical features are consistent, with the peak levels centered about η=0, and about frequency $f' = f\delta_\omega/U_e \sim 0.18$. The consistency along the ramp

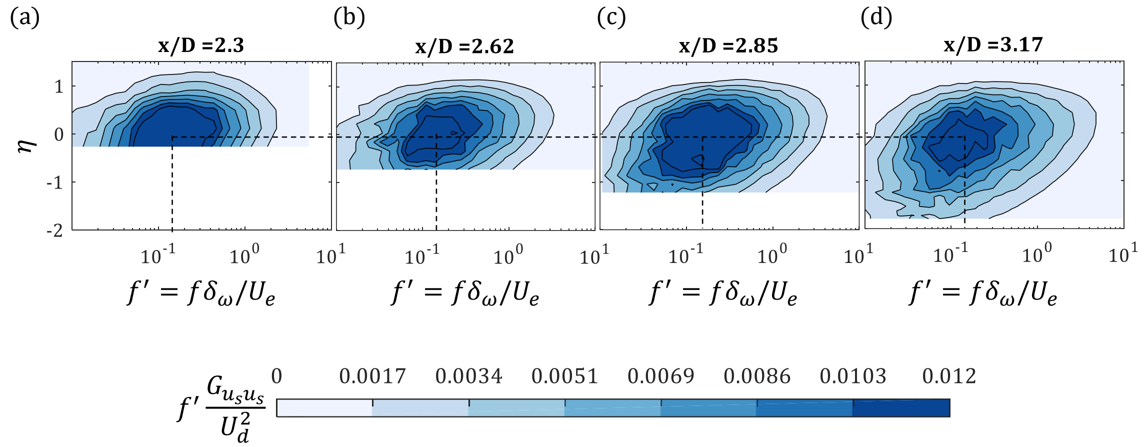

Figure 19: Contours of the pre-multiplied spectra of the streamwise velocity, $f'G_{u_s u_s}/U_d^2$, at different streamwise stations on the ramp. Frequency $f' = f\delta_\omega/U_e$, where $\delta_\omega(x)$ is vorticity thickness and $U_e(x)$ is edge velocity. (a) $x/D = 2.3$ (b) $x/D = 2.62$ (c) $x/D = 2.85$ (d) 3.17. Horizontal dashed lines indicate the position of the peak levels in the shear layer, and vertical dashed lines indicate the center-frequency of the broad peaks

can be visualized better in figure 20. Similar to figure 18, the spectra at each station are normalized with the that of the BOR tail, with the contour levels representing the ratio of the spectra in dB-scale. With the ESL scaling, the streamwise variations are typically within $\pm$ 2 dB as compared to $\pm$ 10 dB for the original spectra. Furthermore, for frequencies $f' < 1$ the streamwise variations are within ± 1 dB, corresponding to a 25% change. This can be seen in the premultiplied line-spectra extracted from the contours in figure 19, corresponding to various representative locations in terms of, η, shown for all streamwise locations on the ramp, in figure 21. While, the functional form of the spectra changes with the distance from the wall consistent with the expected inhomogeneity, the spectra from various streamwise stations are consistent at each η particularly for $f' < 1$ suggesting that the low-frequency (large scale) motions are consistent along the APG region. One can expect this from a boundary layer with an embedded shear layer, where the large scale motions primarily driven by the shear layer are superposed on the underlying boundary layer turbulence.

To summarize, the structure of streamwise turbulence is significantly modified by the strong APG and lateral curvature: The most active region continuously drifts higher in the boundary layer and is centered about the inflection point, consistent with the turbulence stress. As observed in previous studies, the importance of large-scale motions increases as they increasingly energize across the layer while small-scale motions weaken significantly. These large-scale motions appear to be driven by the embedded shear layer, with the spectra below $f\delta_\omega/U_e < 1$ retaining its functional form along the ramp. Additionally, the performance of other scalings, based on the Zagarola-Smits velocity scale ($U_{zs} - \delta$) and on displacement thickness ($U_e - \delta_1$) was inferior to the ESL scaling. In the next section, the impact of APG on the spatial characteristics of the streamwise turbulence, including the evolution of length scales, two-point correlations, and convection velocities are investigated.

3.7. *Correlation structure of streamwise velocity*

The integral time-scale of the streamwise velocity on the ramp Γ_{u_s}, estimated from single hotwire results, is shown in figure 22(a). The time-scale is obtained by directly integrating

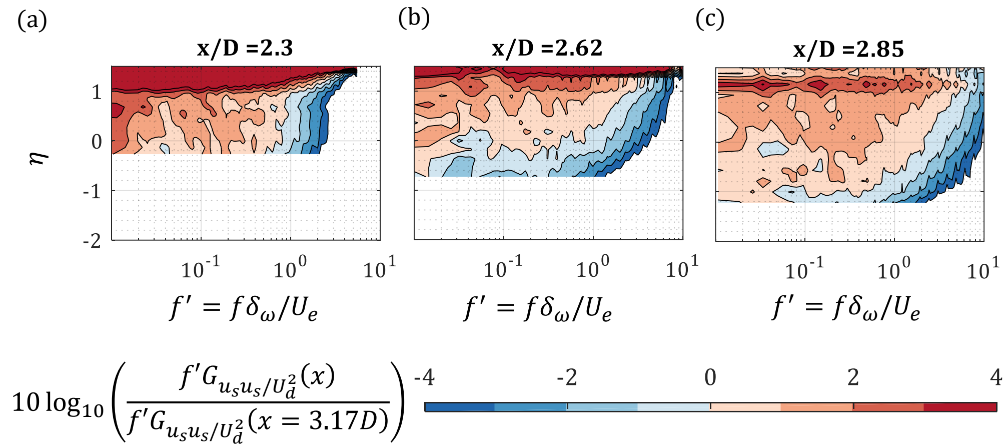

Figure 20: Contours of the pre-multiplied spectra of the streamwise velocity, $f'G_{u_su_s}/U_d^2$, at different streamwise stations on the ramp. Frequency $f' = f\delta_\omega/U_d$, where $\delta_\omega(x)$ is vorticity thickness and $U_e(x)$ is edge velocity. (a) $x/D = 2.3$ (b) $x/D = 2.62$ (c) $x/D = 3.17$.

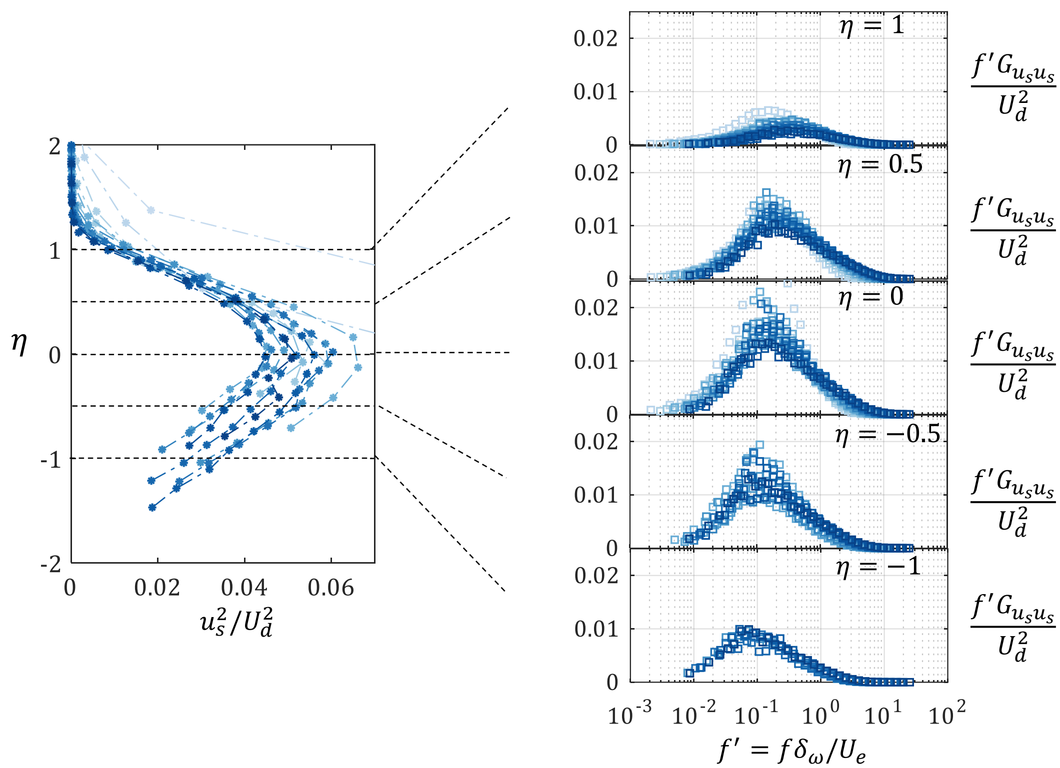

Figure 21: Pre-multiplied spectra of the streamwise velocity based on shear layer parameters. Line spectra in each plot are shown for a particular location in the shear-layer based co-ordinate system. Line spectra shown for η = -1, -0.5, 0, 0.5, 1, moving from bottom to top.

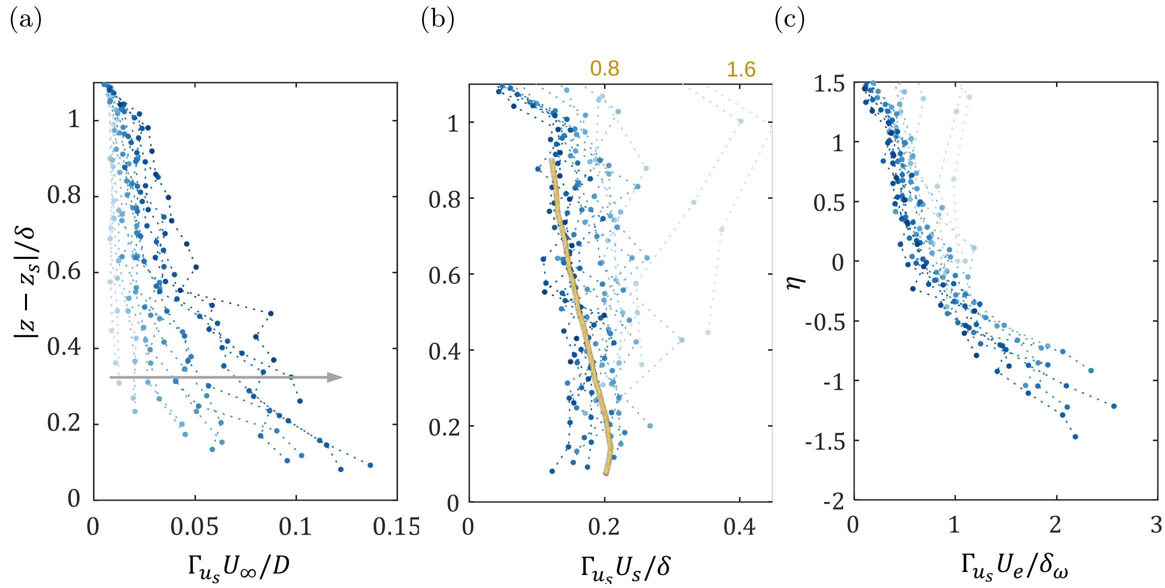

Figure 22: Integral timescale of the streamwise velocity, on the ramp boundary layer. (a) Time-scales normalized on constant reference velocity and BOR diameter, grey arrows shown the variation in the downstream directino. (b) Integral scales from (a) normalized on δ/U_s; orange curve represents the corresponding integral scales from a planar, zero-pressure gradient boundary layer, at a Re_{δ_2}=15,000 (Morton *et al.* 2012); Corresponding x-axis shown on top. (c) Integral scales normalized on the shear layer time-scale (δ_ω/U_e). For legend see Figure 14.

the time-delay correlation coefficient ($\rho_{u_s u_s}$):

$$\Gamma_{u_s}(x,z) = \int_0^\infty \rho_{u_s u_s}(x,z,\tau)d\tau$$

where τ is the time delay. As seen in figure 22(a) the time-scale increases moving into the boundary layer (for $|z - z_s| > 0.1\delta$) at all streamwise stations, and is consistent with both ZPG and APG studies in the past (Glegg & Devenport 2017; Lee 2017). Moving downstream along the ramp, the integral time-scales – that represent large-scale motions – elongate as the mean flow expands, and at $|z - z_s| = 0.5\delta$ are about eight times longer at the BOR tail (x/D =3.172) compared to upstream ($x/D = 2.059$). When normalized with the local boundary layer time-scale δ/U_s (figure 22(b)) it can be seen that time-scales grow roughly proportional to the boundary layer, and the overall form of the profile is somewhat preserved (within the uncertainty). Interestingly, this functional form resembles that of a planar, zero-pressure-gradient boundary layer at $Re_{\delta_2} \approx 15,000$ (Morton *et al.* 2012). While the organization is similar, the time-scales of the BOR flow are about four times shorter than the ZPG layer, in proportion to the respective δ/U_s, highlighting the importance of pressure-gradient and flow history. The integral time-scales normalized on the ESL time-scale (δ_ω/U_e) are shown in figure (figure 22(c)); The tighter collapse indicates that the flow feels the presence of an embedded shear layer.

The corresponding streamwise integral length-scales can be derived from the normalized time-scale $\Gamma_{u_s} U_s/\delta$, shown in figure 22(b). In general, it is very common to estimate the turbulence length-scales from single-point measurements such as described above. The typical assumption is to regard the turbulence as it were frozen and simply convected by the mean flow, as hypothesized by Taylor (1938) for homogeneous and low turbulence

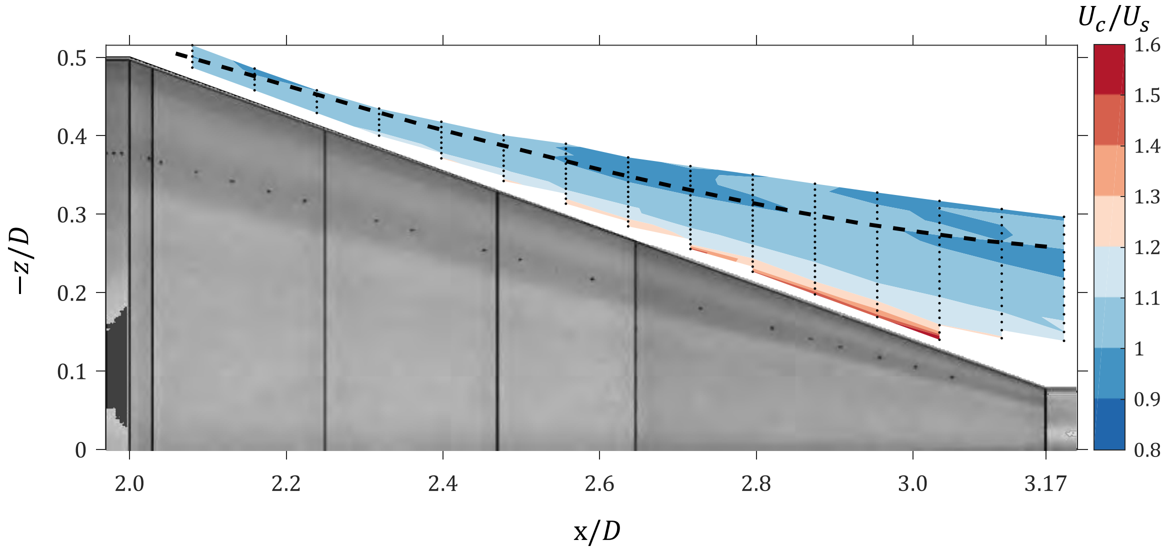

Figure 23: Contours of convection velocity, normalized on the local mean streamwise velocity, measured from dual single-hotwire measurements. Dashed black line represents the boundary layer edge on ramp

flows. However, Taylor's hypothesis has been found to extend for APG flows too, except near the wall where the turbulence structures travelled much faster than the local mean velocity, by as much as a factor of 2 in the buffer region (Drozdz & Elsner 2017). This has been attributed to the growing importance of the large-scale motions in the outer region, which modulate the near-wall motions (Harun *et al.* 2013). To verify this assumption for our flow, we measured the convection velocity along the ramp, with a pair of single hotwires, separated along the streamwise direction. The phase convection velocity, estimated from the slope of the phase-spectrum between the single hotwire probes, are shown in figure 23. Consistent with earlier studies, the convection velocity (U_c) is generally equal to the local mean velocity (U_s) along the ramp, and closer to wall turbulence appears to convect significantly faster than the local mean, by as much as $1.6U_s$ at locations closer than 0.1δ from the wall. While this may instill confidence in using Taylor's hypothesis, the results are not fully reliable, as these measurements were made with a fixed separation between the probes, at all positions on the ramp, and may not represent the true convection velocity of large-scale motions.

Instead, Taylor's hypothesis can be directly examined by comparing the two-point correlation from PIV measurements, against the single-point time-delay correlation from hotwire measurements. In the following analysis, we will first introduce the two-point correlation function of the streamwise velocity in the BOR boundary layer, followed by a comparison with the Taylor's hypothesis estimates of the correlation function, deduced from the single-point measurement. The comparisons will then be used to reveal the validity of the Taylor's hypothesis, highlighting the importance of non-linear effects due to the highly turbulent flow.

The two-point, spatial correlation coefficient for the streamwise velocity is defined as

$$\rho_{u_s u_s}(x, z; x', z') = \frac{\langle u_s(x, z) u_s(x', z')\rangle}{\sqrt{\langle u_s^2(x, z)\rangle \langle u_s^2(x', z')\rangle}} \tag{3.7}$$

where (x', z') is the reference location with respect to which the correlation is computed

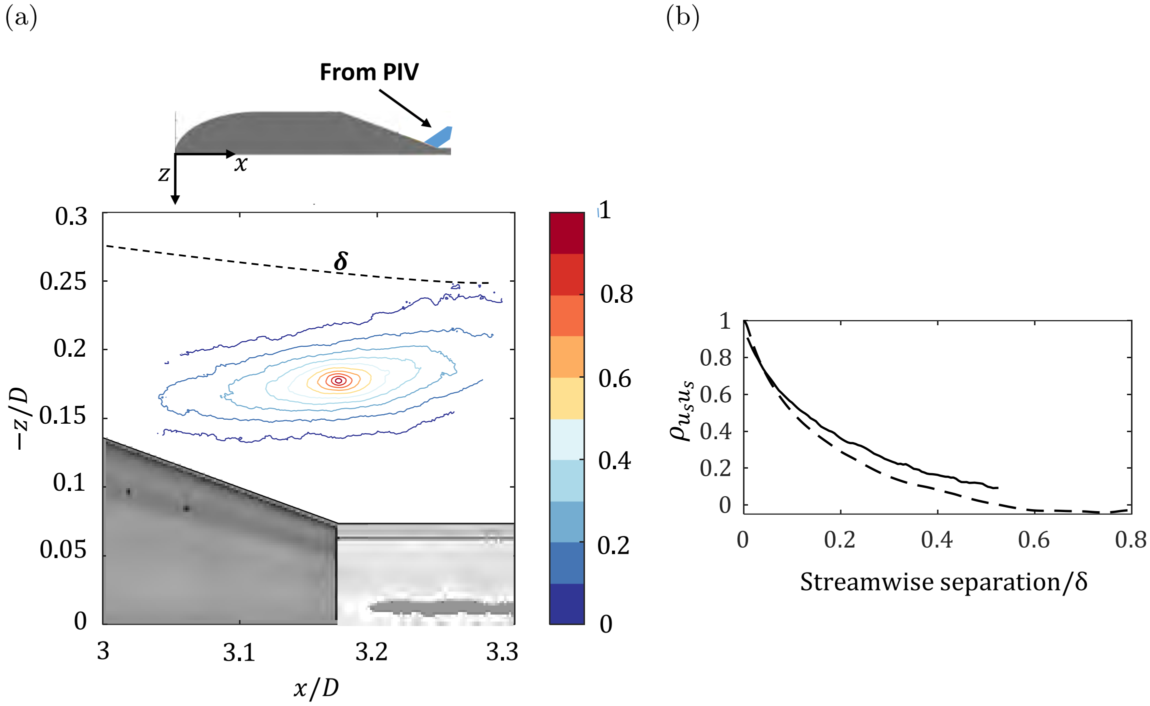

Figure 24: (a) Two point correlation of the streamwise velocity from PIV ($\rho_{u_s u_s}(\Delta x, \Delta r)$), with anchor point at $x/D = 3.172$ and $-z/D = 0.177$ (corresponds to 0.56δ from surface). (b) Spatial correlation from (a) as a function of streamwise separation from PIV, (——) $\rho_{u_s u_s}(x, z, \Delta x_s)$, compared with hotwire estimates via Taylor's hypothesis (- - - -) $\rho_{u_s u_s}(x, x - U_s\tau)$.

by averaging over time. For illustration, figure 24(a) shows the two-point correlation for a reference point at the BOR tail, located 0.56δ from the surface, corresponding to the outer peak in Reynolds stress. The horizontal and vertical axes are to scale in order to ensure accurate interpretation, and the contour lines radiate outward for every 0.1 drop in the correlation coefficient. The average eddy structure appears elliptic, with the major axis (connecting $\rho_{u_s u_s} = 0.2$) inclined to the surface by 27°; While these geometric details are slightly sensitive to streamwise and radial position of the reference point, the structure is generally more compact (in proportion to δ) and further tilted from the horizontal in comparison with high Reynolds number ZPG layers (7° - 12° Tutkun *et al.* (2009); This is consistent with our observation earlier in that the streamwise integral scales of the BOR flow were four-times shorter than the ZPG layer, in comparison to the respective δ.

A slice of the correlation structure from figure 24(a), drawn in the streamwise direction is shown in figure 24(b); This is compared to the single-hotwire estimate obtained through Taylor's hypothesis, defined as

$$\rho_{T,u_s u_s}(x', z'; \Delta x_s) = \frac{\langle u_s(x', z') u_s(x', z', x' - U_s\tau)\rangle}{\sqrt{\langle u_s^2(x, z)\rangle \langle u_s^2(x', z', x' - U_s\tau)\rangle}} \tag{3.8}$$

where x', z' is the reference location (where the probe is positioned), $\Delta x_s (= x' - U_s\tau)$ is the separation along the streamwise direction, assuming that the turbulence is frozen and convecting at the local mean speed U_s. Clearly, the dashed line representing the Taylor's hypothesis estimate (equation 3.8) decays faster than the solid line representing

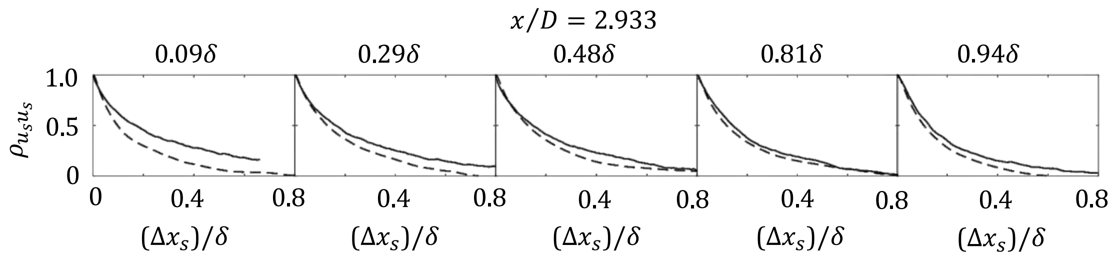

Figure 25: Two-point correlation from PIV compared to spatial correlation obtained from single-point hotwire measurements using Taylor's hypothesis

the true two-point correlation (equation 3.7), decaying to 10% at 0.33δ, nearly twice as fast compared to 0.53 δ for the two-point estimate. This inconsistency exists at all other streamwise stations, and there appears to a definite pattern in the wall-normal direction, shown in figure 25. Here the two-point correlation and Taylor's hypothesis estimate are compared for various locations in the boundary layer at a slightly upstream position ($x/D = 2.933$). While $\rho_{T,u_s u_s}(x', z', \Delta x_s)$ generally decays faster than the two-point estimates, the discrepancy intensifies further inside the boundary layer. To quantify this systematic deviation, we evaluate the integral length-scales by integrating the correlation coefficient, with the true lengthscale defined as,

$$L(x', z') = \int_0^\infty \rho(x', z', \Delta x_s) dx_s \tag{3.9}$$

And for the length-scale estimate from time-delay correlations (through Taylor's hypothesis)

$$L_s(x', z') = \int_0^\infty \rho(x', z'; x' - U_s\tau) d(x' - U_s\tau) = \Gamma(x', z') U_s(x', z') \tag{3.10}$$

Similarly, the length-scale estimates via Taylor's hypothesis using the measured convection velocity(U_c)

$$L_c(x', z') = \int_0^\infty \rho(x', z', x' - U_c\tau) d(x' - U_c\tau) = \Gamma(x', z') U_c(x', z') \tag{3.11}$$

Estimates of the integral length scales at $x/D = 2.933$ obtained through equations 3.9 - 3.11 are shown in figure 26(a). Generally speaking, Taylor's hypothesis seems to reasonably predict the length-scale the outer half of the boundary layer ($> 0.6\delta$), where we see that the various length-scale estimates are consistent, at about 0.2δ. However, in the lower 40% of the boundary layer, Taylor's hypothesis significantly underpredicts the lengthscale. Based on the local mean velocity, the length-scale estimates are about 60% smaller at $|z - z_s|$=0.1δ, while the measured convection velocity (U_c) based estimates are closer to the true length scale. This suggests that for this highly turbulent flow, where the local turbulence intensity is as high as 30% U_s near the wall, the non-linear interactions could be significant, and the turbulence appears to be convecting itself. Therefore, significant corrections are required when estimating the length-scale from Taylor's hypothesis, which is an important input for predictions of far-field noise spectrum, for example of a rotor ingesting such highly turbulent flows. In this case, though an ingesting rotor sees the turbulence at a fixed location just like the fixed hotwire, the fact that this inferred lengthscale is inaccurate may complicate the extrapolation of this estimate into the full multi-dimensional correlation function, increasing the error of using

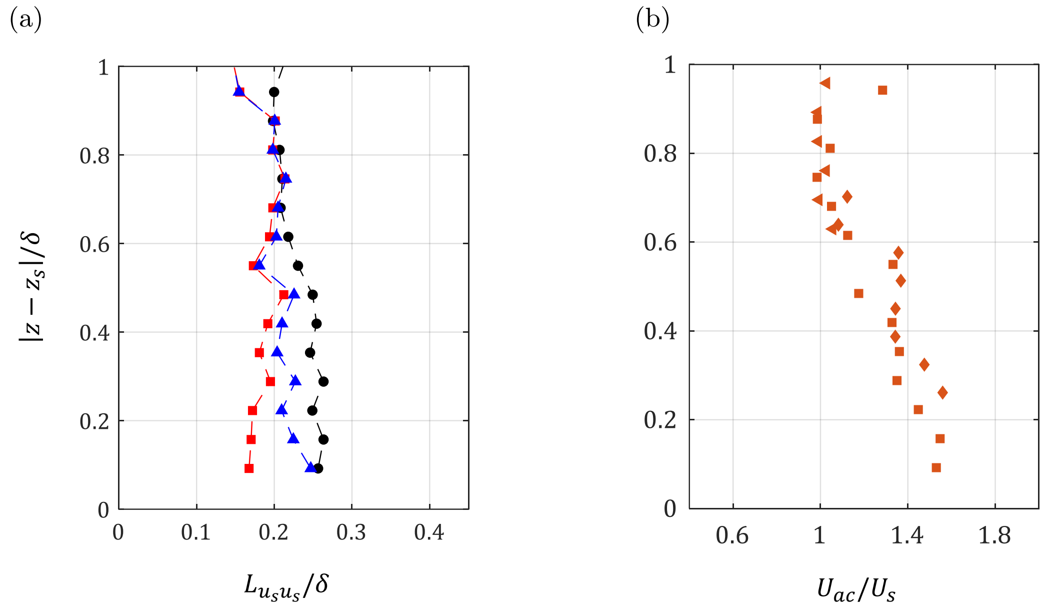

Figure 26: (a) Integral length scales in the boundary layer at $x/D = 2.933$; (●) $L_{u_s u_s}/\delta$ (PIV), (■) $\Gamma_{u_s u_s} U_s/\delta$ (Taylor's hypothesis with local mean velocity), (▲) $\Gamma_{u_s u_s} U_c/\delta$ (Taylor's hypothesis with measured convection velocity); (b) Apparent convection velocity ($U_{ac} = L_{u_s u_s}/\Gamma_{u_s u_s}$) at representative streamwise stations; (◀) $x/D = 2.854$; (■) $x/D = 2.933$; (◆) $x/D = 3.092$;

standard forms such as from the homogeneous turbulence. To contain such a potential error, simple corrections can be proposed, by assuming that the turbulence is still frozen as it convects, and estimating the apparent convection velocity (U_{ac}) of the integral turbulence structures, based on the measured length and time scales,

$$U_{ac}(x', z') = L_{u_s u_s}(x', z')/\Gamma_{u_s u_s}(x', z') \tag{3.12}$$

The apparent convection velocity U_{ac} normalized on the local mean velocity, is shown in figure 26(b). Results are shown for available data at various streamwise stations, and are consistent. The frozen turbulence actually convects at the local mean speed only in the outer portions of the boundary layer ($> 0.6\delta$). Below 0.6δ, the turbulence apparently convects at over 40% above the local mean speed. Closer to the wall even significant corrections are expected. This is an important result for aeroacoustics community.

To fully document the average eddy structure of streamwise velocity in order to provide quantitative inputs for turbulence modelling and aeroacoustic predictions, we measured a subset of the radial and circumferential correlation with a single-hotwire at the BOR tail (x/D=3.172). With the conventional anchor-probe and moving-probe arrangement, the correlations were measured at four anchor points in the boundary layer, represented in figure 27(a) with the turbulence intensity contours in the background; While the circumferential correlations were measured about the vertical axis, the radial correlations were measured about the horizontal, anchored at 0.40, 0.65, 0.75, and 0.85δ. As the trends were more or less consistent at all anchor points, results are shown for just the 0.4δ case in figure 27(b), along with the streamwise correlation for comparison. Here, the correlation coefficient $\rho_{u_s u_s}$ is shown on the vertical axis, with separation (normalized on δ) on the horizontal axis (separation implies $x' - x_s$ for streamwise, $r' - r$ for radial, $r'(\Delta\theta)$ for circumferential). Furthermore, to cross-validate measurements, the corresponding results from PIV (solid lines) are included with the hotwire estimates (dashed lines): While

(a) (b)

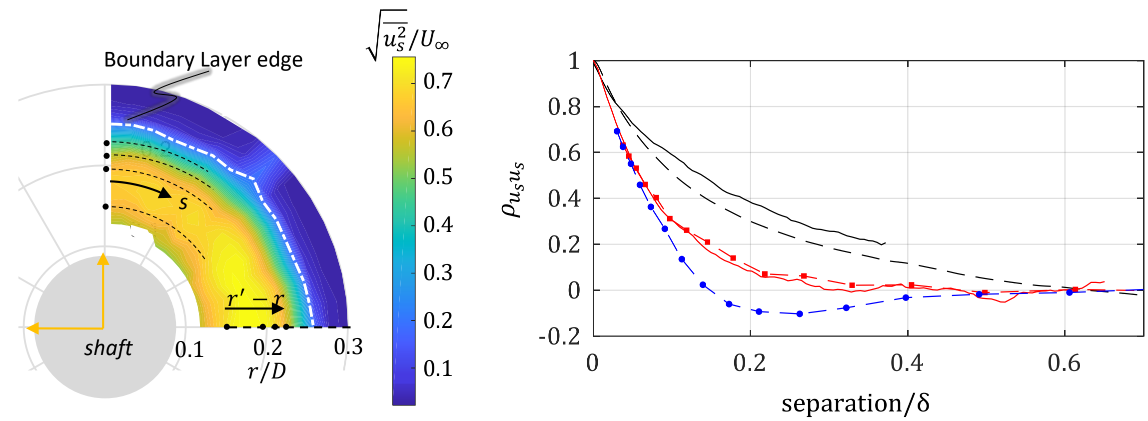

Figure 27: (a) The cross-section at Ramp tail (x/D=3.17), showing the measurement grid for circumferential and radial correlation measurements. Circumferential correlations were measured about the vertical axis and radial correlations along the horizontal axis. The contour levels in the background reveal the turbulence intensity; (b) Correlation coefficient of the streamwise velocity: solid lines indicate PIV results, dashed line indicate hotwire results. Streamwise correlation in black, radial in red, and circumferential in blue.

$-z/D$	$\lvert z - z_s \rvert/\delta$	$L_{u_s u_s}(r)/\delta$	$L_{u_s u_s}(c)/\delta$	L_r/L_c
0.147	0.40	0.089	0.060	1.48
0.194	0.65	0.081	0.055	1.47
0.212	0.75	0.079	0.055	1.44
0.231	0.85	0.078	0.043	1.80

Table 3: Integral length scales of the streamwise velocity, in the radial and circumferential direction, at the BOR tail

the disagreement in the streamwise correlation has been attributed to the inaccuracy of Taylor's hypothesis as discussed above, the agreement in the radial correlations suggests an absence of hotwire probe interference effects.

Similar to the streamwise correlation, the radial correlation (red) decays monotonically with increasing separation, but decays about twice as fast, reaching 10% level at a separation of 0.2δ. The circumferential correlations (blue) decay even faster, reaching 10% level in just about 0.12δ (depending slightly on the anchor position), and develop a negative tail (-5%) at larger separation. The corresponding integral length-scales, calculated by integrating the area under the correlation curve (including the negative excursions), and considered to represent the large-scale features, are shown in table 3 for the four anchor positions. Consistent with the correlations in figure 27(b) the radial length-scale is 0.09δ, about 40% of the streamwise length-scale. The associated circumferential length-scale at this position is even smaller at 0.06δ, roughly a quarter of the streamwise scale. This anisotropy of the length-scales is not too different in the outer boundary layer as all the length-scales shorten slightly, and are organized at a $1 : 0.6 : 0.3$ ratio (between the streamwise, radial and circumferential scales) at 0.85δ.

4. Conclusions

This study describes the experiments performed over a body-of-revolution at Reynolds number, based on the length and free-stream velocity, of 1.9 million. The transverse curvature parameters were moderate ($\delta/r_s < 0.2, r_s^+ > 500$), but the pressure gradient was increasingly adverse towards the tail ($\beta_C \rightarrow 5, 20$): reminiscent of the vehicle-relevant conditions. The dataset for this non-equilibrium boundary layer is publicly available at DOI (will be included after revisions).

The combined response to the adverse pressure gradient and the transverse curvature is evaluated on the mean flow, turbulence structure and correlation structure. Important results include:

(i) The mean velocity and turbulence intensity profiles appear self-similar with the embedded shear layer scaling (Schatzman & Thomas 2017). Based on the inflection points in the boundary layer, located at 1.2 displacement thickness from the surface, the velocity defect served as the velocity scale while the vorticity thickness served as the length scale. The functional form of the velocity profile was well-described by error function (commonly used for planar mixing layer flows). While the collapse in the turbulence intensity was not as perfect, the peak turbulent stress is about $0.023U_d$, close to the value of 0.021 observed by Schatzman & Thomas.

(ii) The vorticity thickness was found to grow linearly along the streamwise direction, at a rate consistent with free-shear layer flows. Furthermore, as expected the length and velocity scales are directly proportional to the boundary layer edge velocity and thickness respectively, by a factor of 0.4. However, it is not definitive whether the inviscid instabilities drive the embedded shear layer motions, rather it appears as if the existence of mean velocity inflection points and the embedded shear layer are correlated but not causal.

(iii) The turbulence structure of the streamwise velocity reflects the observations from the mean flow. The flow becomes increasingly turbulent, with the large-scale motions amplifying and grow roughly proportional to the boundary layer thickness. In the low frequency regions, the pre-multiplied spectra scale with the embedded shear-layer timescale (δ_ω/U_e), emphasizing the direct influence of the embedded shear layer motions in the large-scale activity.

(iv) Analysis of the correlation structure revealed that the non-linear interactions in the turbulence could be significant since the Taylor's hypothesis severely underpredicted the integral lengthscales. Comparisons of the two-point correlations and the single-point estimates (using Taylor's hypothesis) revealed that the apparent convection velocity is about 1.4 times the local mean velocity in the inner half of the boundary layer, and even higher close to the wall. It appears as if the turbulence may be convecting itself, provided the turbulence intensity was higher than 20% of the local mean velocity. These corrections must be factored in when single-point measurements are used to derive the length-scales, which is a common practice in the aeroacoustics far-field noise predictions.

Acknowledgments

We acknowledge the support from the Office of Naval Research, particularly Drs. Ki-Han Kim and John Muench, in supporting this work under grants N00014-17-1-2698 and N00014-20-1-2650. We are grateful to Drs. Stewart Glegg, Meng Wang, William Blake and Jason Anderson, and Mr. Michael Marcolini, for their helpful advice and support on this work. We wish to thank the Aerospace and Ocean Engineering Machine Shop staff headed by Mr. James Lambert, in leading the fabrication and instrumentation hardware efforts. We also thank the Virginia Tech Wind Tunnel staff Dr. Aurélien Borgoltz, Bill Oetjens; And all the graduate research assistants, particularly Mr. Anthony Millican, for assistance during experiments.

Declaration of interests

The authors report no conflict of interest.

REFERENCES

Bearman, P.W. 1971 Corrections for the effect of ambient temperature drift on hot-wire measurements in incompressible flow. *DISA Information* **11**, 25–30.

Bobke, A., Vinuesa, R., Örlü, R. & Schlatter, P. 2017 History effects and near equilibrium in adverse-pressure-gradient turbulent boundary layers. *Journal of Fluid Mechanics* **820**, 667–692.

Castillo, Luciano & George, William K. 2001 Similarity analysis for turbulent boundary layer with pressure gradient: Outer flow. *AIAA Journal* **39** (1), 41–47.

Cipolla, K. M. & Keith, W. L. 2003 High reynolds number thick axisymmetric turbulent boundary layer measurements. *Experiments in Fluids* **35** (5), 477–485.

Clauser, Francis H 1954 Turbulent boundary layer in adverse pressure gradient. *J. Aero. Sci.* **21**, 91–108.

Devenport, William J., Burdisso, Ricardo A., Borgoltz, Aurelien, Ravetta, Patricio A., Barone, Matthew F., Brown, Kenneth A. & Morton, Michael A. 2013 The kevlar-walled anechoic wind tunnel. *Journal of Sound and Vibration* **332** (17), 3971–3991.

Drozdz, A. & Elsner, W. 2017 Amplitude modulation and its relation to streamwise convection velocity. *International Journal of Heat and Fluid Flow* **63**, 67–74.

Elsberry, K, Loeffler, J, Zhou, MD & Wygnanski, I 2000 An experimental study of a boundary layer that is maintained on the verge of separation. *Journal of Fluid Mechanics* **423**, 227–261.

Glauert, MB & Lighthill, Michael James 1955 The axisymmetric boundary layer on a long thin cylinder. *Proc. R. Soc. Lond. A* **230** (1181), 188–203.

Glegg, Stewart & Devenport, William 2017 *Aeroacoustics of low Mach number flows: fundamentals, analysis, and measurement*. Academic Press.

Gungor, A. G., Maciel, Y., Simens, M. P. & Soria, J. 2016 Scaling and statistics of large-defect adverse pressure gradient turbulent boundary layers. *International Journal of Heat and Fluid Flow* **59**, 109–24.

Hammache, M, Browand, FK & Blackwelder, RF 2002 Whole-field velocity measurements around an axisymmetric body with a stratford–smith pressure recovery. *Journal of Fluid Mechanics* **461**, 1–24.

Harun, Z., Monty, J. P., Mathis, R. & Marusic, I. 2013 Pressure gradient effects on the large-scale structure of turbulent boundary layers. *Journal of Fluid Mechanics* **715**, 477–98.

Jordan, Stephen A. 2014 On the axisymmetric turbulent boundary layer growth along long thin circular cylinders. *Journal of Fluids Engineering* **136** (5).

Kitsios, Vassili, Sekimoto, Atsushi, Atkinson, Callum, Sillero, Juan A, Borrell, Guillem, Gungor, Ayse G, Jiménez, Javier & Soria, Julio 2017 Direct numerical simulation of a self-similar adverse pressure gradient turbulent boundary layer at the verge of separation. *Journal of Fluid Mechanics* **829**, 392–419.

Kumar, Praveen & Mahesh, Krishnan 2018 Large-eddy simulation of flow over an axisymmetric body of revolution. *Journal of Fluid Mechanics* **853**, 537–563.

Lee, Jae Hwa 2017 Large-scale motions in turbulent boundary layers subjected to adverse pressure gradients. *Journal of Fluid Mechanics* **810**, 323–61.

Lueptow, Richard M., Leehey, Patrick & Stellinger, Thomas 1985 The thick, turbulent boundary layer on a cylinder: Mean and fluctuating velocities. *The Physics of Fluids* **28** (12), 3495–3505.

Maciel, Yvan, Simens, Mark P. & Gungor, Ayse G. 2017 Coherent structures in a non-equilibrium large-velocity-defect turbulent boundary layer. *Flow, Turbulence and Combustion* **98** (1), 1–20.

Maciel, Y., Tie, Wei, Gungor, A. G. & Simens, M. P. 2018 Outer scales and parameters of adverse-pressure-gradient turbulent boundary layers. *Journal of Fluid Mechanics* **844**, 5–35.

Morton, M.A., Devenport, W.J. & Glegg, S. 2012 Rotor inflow noise caused by a boundary layer: Inflow measurements and noise predictions.

Nagano, Yasutaka, Tsuji, Toshihiro & Houra, Tomoya 1998 Structure of turbulent boundary layer subjected to adverse pressure gradient. *International Journal of Heat and Fluid Flow* **19** (5), 563–572.

Neves, João C., Moin, Parviz & Moser, Robert D. 1994 Effects of convex transverse curvature on wall-bounded turbulence. part 1. the velocity and vorticity. *Journal of Fluid Mechanics* **272**, 349–382.

Oster, D. & Wygnanski, I. 1982 The forced mixing layer between parallel streams. *Journal of Fluid Mechanics* **123**, 91–130.

Piquet, J. & Patel, V. C. 1999 Transverse curvature effects in turbulent boundary layer. *Progress in Aerospace Sciences* **35** (7), 661–672.

Rao, G. N. V. 1967 The law of the wall in a thick axisymmetric turbulent boundary layer. *Journal of Applied Mechanics* **34** (1), 237–238.

Schatzman, D. M. & Thomas, F. O. 2017 An experimental investigation of an unsteady adverse pressure gradient turbulent boundary layer: embedded shear layer scaling. *Journal of Fluid Mechanics* **815**, 592–642.

Skåre, Per Egil & Krogstad, Per-Åge 1994 A turbulent equilibrium boundary layer near separation. *Journal of Fluid Mechanics* **272**, 319–348.

Snarski, Stephen R. & Lueptow, Richard M. 1995 Wall pressure and coherent structures in a turbulent boundary layer on a cylinder in axial flow. *Journal of Fluid Mechanics* **286**, 137–171.

Song, Simon, DeGraaff, David B & Eaton, John K 2000 Experimental study of a separating, reattaching, and redeveloping flow over a smoothly contoured ramp. *International Journal of Heat and Fluid Flow* **21** (5), 512–519.

Taylor, Geoffrey Ingram 1938 The spectrum of turbulence. *J Proceedings of the Royal Society of London. Series A-Mathematical Physical Sciences* **164** (919), 476–490.

Tutkun, M., George, W. K., Delville, J., Stanislas, M., Johansson, P. B. V., Foucaut, J. M. & Coudert, S. 2009 Two-point correlations in high reynolds number flat plate turbulent boundary layers. *Journal of Turbulence* **10**, N21.

Tutty, O. R. 2008 Flow along a long thin cylinder. *Journal of Fluid Mechanics* **602**, 1–37.

Tutu, Narinder K. & Chevray, Rene 1975 Cross-wire anemometry in high intensity turbulence. *Journal of Fluid Mechanics* **71** (4), 785–800.

Vila, Carlos Sanmiguel, Örlü, Ramis, Vinuesa, Ricardo, Schlatter, Philipp, Ianiro, Andrea, Discetti, Stefano & combustion 2017 Adverse-pressure-gradient effects on turbulent boundary layers: statistics and flow-field organization. *Flow, Turbulence and Combustion* **99** (3-4), 589–612.

Wittmer, K. S., Devenport, W. J. & Zsoldos, J. S. 1998 A four-sensor hot-wire probe system for three-component velocity measurement. *Experiments in Fluids* **24** (5), 416–423.

Zagarola, Mark V. & Smits, Alexander J. 1998 Mean-flow scaling of turbulent pipe flow. *Journal of Fluid Mechanics* **373**, 33–79.

Zhou, Di, Wang, Kan & Wang, Meng 2020 *Large-Eddy Simulation of an Axisymmetric Boundary Layer on a Body of Revolution*. American Institute of Aeronautics and Astronautics.

Chapter 4

Wall pressure signature of an axisymmetric boundary layer under a strong adverse pressure gradient

This chapter presents a manuscript to be submitted to the Journal of Fluid Mechanics and is presented in a format prescribed by the journal.

Wall pressure signature of an axisymmetric boundary layer under strong adverse pressure gradient

N. Agastya Balantrapu[1]†, W. Nathan Alexander[1], and William Devenport[1]

[1]Department of Aerospace and Ocean Engineering, Virginia Tech, Blacksburg, VA 24060, USA

(Received xx; revised xx; accepted xx)

Measurements of fluctuating wall pressure in a high Reynolds number flow over a body-of-revolution are described in combination with large eddy simulation. With a strong axial pressure gradient and moderate lateral curvature, this non-equilibrium flow is relevant to marine applications as well as short-haul urban transportation. The wall pressure spectrum and its scaling are discussed along with its relation to the space-time structure. As the flow decelerates downstream, the root-mean-square level of the pressure drops together with the wall shear-stress (τ_w) and is consistently about $7\tau_w$. While the associated dimensional spectra see a broadband reduction of over 15-dB per Hz, they appear to attain a single functional form, collapsing to within 2-dB when normalized with the wall-wake scaling where τ_w is the pressure-scale and U_e/δ is the frequency scale. Here δ is the boundary layer thickness and U_e is the local free-stream velocity. The general success of the wall-wake scaling, including in the viscous f^{-5} region, suggests that the large-scale motions in the outer layer play a predominant role in the near-wall turbulence and wall-pressure. On investigating further, we find that the instantaneous wall pressure fluctuations are characterized by a quasi-periodic feature that appears to convect downstream at speeds consistent with the outer-peak in the turbulence stresses. The conditional structure of this feature estimated through wavelet transform, resembles that of a roller, supporting the embedded shear layer hypothesis Schatzman & Thomas (2017); Balantrapu *et al.* (2021). Therefore, the outer region shear-layer type motions may be important when devising strategies for flow-control, drag and noise reduction for decelerating boundary layers.

Key words: [TBD]

1. Introduction

The pressure signature of turbulent boundary layers on the underlying surfaces are under active study for their relevance to structural vibrations and noise. In particular, the pressure fluctuations determine the source terms for the far-field noise produced by the

† Email address for correspondence: balantrapu@vt.edu

flow past an airfoil trailing edge. Similarly, the low wave-number components of the pressure spectrum determine the structural vibrations and noise in an aircraft or marine vehicle (Blake 2017). Fundamentally, the pressure fluctuations on the surface are an integrated effect of the turbulent velocity field across the boundary layer, as seen from the solution to the incompressible pressure-Poisson equation,

$$p(\boldsymbol{x}, t) = -\frac{\rho}{2\pi} \oint_V \left[2 \frac{\partial \overline{U_i}}{\partial x_j} \frac{\partial u_j}{\partial x_i} + \frac{\partial}{\partial x_i x_j} \left(u_i u_j - \overline{u_i u_j} \right) \right]_{(\boldsymbol{y}, t)} \frac{dV(\boldsymbol{y})}{|\boldsymbol{x} - \boldsymbol{y}|} \tag{1.1}$$

The fluctuating pressure at a point $\boldsymbol{x}$ on the surface depends on a complex combination of the mean flow ($U_i, \overline{u_i u_j}$; where $i, j = 1, 2, 3$) and turbulent fluctuations (u_i) in the boundary layer, weighted by the inverse of the distance from that point $|\boldsymbol{x} - \boldsymbol{y}|$. The first term of the integrand incorporates the mean velocity gradient and is thought to respond immediately to changes in the mean flow, therefore known also as the rapid-term. The second term is non-linear in the fluctuating velocity and is known as the slow term as it is thought to respond indirectly to changes in the mean flow as it modifies the convective turbulence. Substantial efforts over the past few decades, directed at the canonical case of a planar, zero pressure gradient (ZPG) flow, have lead to an improved understanding of the wall pressure mechanisms, and consequently well-accepted models for the wall pressure spectrum (Goody 2004), and the full wavenumber-frequency spectrum (Corcos 1964; Chase 1980; Smol'yakov 2006). Some outstanding issues such as the lack of consensus in the acoustic and sub-convective ranges of the wavenumber–frequency spectrum require very carefully designed experiments and expensive simulations, and are beginning to be addressed.

For axisymmetric bodies, the effect of lateral curvature on pressure fluctuations has been briefly studied by considering axial flow past a circular cylinder. The importance of lateral curvature on the flow and therefore the wall-pressure has been characterized by two parameters: δ/r_s which measures the boundary layer thickness (δ) relative to the radius of curvature of the surface (r_s), and $r_s^+ = r_s u_\tau/\nu$, the curvature Reynolds number where u_τ is the friction velocity and ν is the dynamic viscosity. Flows with low δ/r_s and high r_s^+ that represent a high Reynolds number flow over a large cylinder (Piquet & Patel 1999) are of interest here as they represent the vehicle-relevant conditions. In this case, previous studies (see Snarski & Lueptow (1995)) have shown that while the mean velocity profiles are fuller with a corresponding increase in the skin-friction as compared to the flat-plate case, the fundamental turbulence mechanisms in terms of the production and transport are preserved. In an early experimental study by Willmarth & Yang (1970) the space-time structure of the wall pressure was examined on an axial cylinder with $\delta/r_s = 2$ and $r_s^+ = 4500$ and they observed that the spectral organization of the fluctuating pressure was mostly similar to a flat-plate case with consistent mean-square levels, but the high frequency regions ($\omega\delta_1/U_e > 10$) amplified by about $\sim$ 2-dB while the low frequency fluctuations weakened to compensate the increase. This shift towards the high-frequency content was consistent with their observation of a decreased correlation length-scale in both longitudinal and lateral directions. While the length-scales were smaller, they observed the convection velocity to be similar to flat-plate flow. This prompted them to suggest that the pressure-producing motions are smaller and located closer to the wall, but convected at equivalent speeds due to the fuller mean velocity profiles for the cylinder flow. At higher curvatures, the flow regime corresponds to that of a long slender rod (or an axisymmetric wake with an inner layer), representing applications relevant to towed-array sensor systems and the corresponding impacts on the wall-pressure are more severe, and are discussed by Willmarth *et al.* (1976); Neves & Moin (1994); Bokde *et al.* (1998).

Pressure fluctuations in axially-symmetric boundary layers under mean pressure gradient are much more complex and have not been investigated to the authors' knowledge. The impact of pressure-gradient even on planar boundary layer flows is inherently complex as the flow is sensitive to the pressure-gradient history in addition to the local conditions, posing a prohibitively large parameter space. In an early experimental study of mild adverse pressure gradient (APG) flow, Schloemer (1966) observed an increase in the low-frequency spectrum, with a corresponding net increase in the mean-square energy in comparison with a ZPG layer at otherwise similar conditions. Examining the space-time correlations, he observed that the convection velocity, at similar non-dimensional separations and frequencies, was smaller than the ZPG case as a result of larger velocity defect throughout the boundary layer, and is consistent with the findings of Bradshaw (1967). For stronger APG flows approaching separation, Simpson *et al.* (1987) observed the mean-square energy to increase monotonically, scaling with the maximum turbulent shear stress in the outer region, as opposed to τ_w for ZPG layers (Bull 1996). However, as summarized by Cohen & Gloerfelt (2018) much of the early experimental work is reliable only in the low-frequency regions due to large diameter transducers that suffered from inadequate spatial resolution, preventing an accurate estimation of the higher frequency content.

More recent work investigating the fluctuations in planar APG boundary layers has considered a wider range of configurations including non-equilibrium flows over airfoils and wedges (Rozenberg *et al.* 2012; Catlett *et al.* 2015; Kamruzzaman *et al.* 2015; Lee 2018; Hu & Herr 2016). The major focus of these works has been on development of models for the wall pressure spectrum, by extending Goody's model for ZPG flows (Goody 2004). Several parameters have been proposed to accommodate the strength and history of the pressure gradient, generally based on the Clauser's parameter $\beta_C = \delta_1/\tau_w dp/dx$, and/or the shape-factor $H = \delta_1/\delta_2$. As summarized by Lee (2018), none of the models are universally successful; This is not totally unexpected since the convective turbulence in the grazing flow – the source of these pressure fluctuations – is not yet fully characterized for pressure gradient flows. Recently, Grasso *et al.* (2019) showed that the pressure spectrum for APG flows (obtained from the solution to Poisson equation) was sensitive to the assumed analytical form of the two-point turbulence. Therefore the development of well-accepted models requires a systematic study covering a broad range of pressure-gradient histories, examining both the evolution of turbulence and the corresponding wall pressure spectrum.

For the particular case of strong APG flows – the focus of this paper – recent research (Kitsios *et al.* 2017; Schatzman & Thomas 2017; Krogstad & Skare 1995) has suggested a fundamental change in the character of boundary layers that develop inflectional mean velocity profiles in the outer region, which correspond to a secondary peak in the turbulence production and transfer. Examining the conditional velocity structure, the sweep motions were observed to dominate just above the inflection point, while ejections dominated below. Schatzman & Thomas, through further analysis, suggested the presence of an embedded shear layer with coherent spanwise-oriented vorticity centered about the inflection points. The impact of these findings on the turbulence structure and consequently on the fluctuating wall pressure must be examined.

The object of our research is to provide an understanding of the strong-adverse pressure gradient axisymmetric boundary layers, in particular of its turbulence structure and the associated wall pressure fluctuations. The companion paper (Balantrapu *et al.* (2021), hereafter referred to as BHAD) presents the measurements of the mean flow and turbulence structure of a boundary layer over a body-of-revolution. BHAD found that the axisymmetric boundary layer behaved as if there is an embedded shear layer in the outer region; Despite being out-of-equilibrium and evolving significantly, the mean velocity and turbulence statistics were self-similar with a free shear layer type scaling (proposed by Schatzman & Thomas), where the velocity-defect at the inflection point was the velocity scale and the vorticity thickness was the length-scale. Furthermore, while the large-scale activity in the outer regions energized as the flow decelerated, the spectral distribution of the streamwise velocity was roughly self-similar with the embedded shear layer scaling, suggesting the importance of the embedded shear layer motions.

In this paper we present the associated wall pressure spectrum and its scaling, along with its relation to the space-time structure. The work is organized as follows. First, we describe the apparatus and instrumentation in § 2. Then we present the results and discussion (§ 3), summarizing the flow parameters (§ 3.1) as required to follow the detailed discussion of the wall-pressure spectrum and its scaling in § 3.2. We then describe the associated space-time structure as it relates to the observations made in the wall-pressure spectrum. One principal conclusion is that the wall pressure spectrum collapses at all frequencies with the wall-wake scaling, where τ_w is the pressure scale and U_e/δ is the frequency scale. This broadband success, including the f^{-5} regions suggests that outer region motions play a dominant role in near-wall turbulence and wall-pressure. Particularly, we detect a quasi-periodic feature in the instantaneous wall pressure with a signature similar to that of a roller-eddy, and this appears to convect downstream at speeds matching that at the outer peak of the turbulence stresses.

2. Apparatus and Instrumentation

The apparatus and instrumentation, except the wall pressure microphones, is largely similar to those detailed in BHAD and are briefly presented here. All measurements were performed in the anechoic test-section of the Virginia Tech stability wind tunnel, designed and documented by Devenport *et al.* (2013). The test-section is 1.85 m x 1.85 m wide and 7.3 m long and features side walls formed by tensioned Kevlar, that contain the flow while remaining acoustically transparent, minimizing the acoustic reflections. Sound passing through the walls is absorbed into anechoic chambers on either side, that are lined with acoustic foam wedges, designed to minimize reflections down to 190-Hz. The floor and ceiling are similarly treated with perforated metal panels lined with Kevlar and backed by 0.457-m acoustic foam wedges. Additionally, the entire circuit is acoustically treated to minimize background acoustic reflections.

The body-of-revolution (BOR), shown in figure 1, has a characteristic length D = 0.4318 m and has a forebody comprised of a 2:1 ellipsoid nose joined to a constant diameter body, each 1D long. A 0.8 mm x 0.8 mm ring sandwiched between the nose and centerbody (at $x/D = 0.98$) is used to trip the flow. The aft body is a 20 degree tail cone, which is truncated at $1.172D$ to facilitate installation in the test-section. The BOR is positioned via a hollow-sting cantilevered from a streamlined strut positioned which is 0.91-m downstream from the tail to ensure the hydrodynamic perturbation was less than 0.5% of the free-stream velocity U_∞; While the strut was streamlined to McMaster Henderson airfoil to mitigate trailing edge shedding (Glegg & Devenport 2017), some acoustic contamination was observed in the downstream mics, but was tonal (at about 2000 Hz) and weak compared to the underlying hydrodynamic content (see §3.2 for

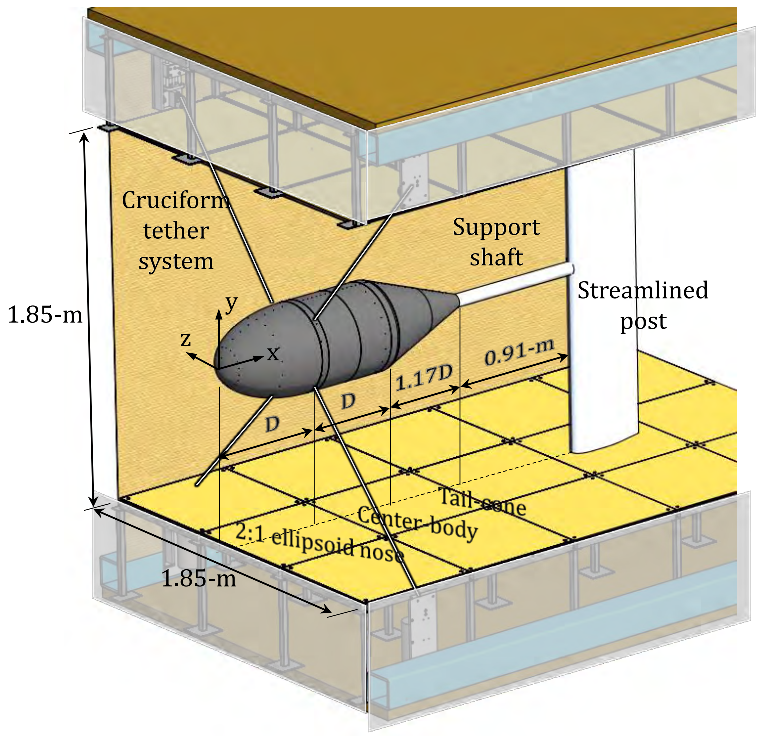

Figure 1: Schematic of the test-section, showing the BOR geometry and experimental arrangement.

treatment of this data). While the BOR was positioned with the downstream sting, it was suspended in the test-section via a cruciform 0.9 mm tethers running through center-body, just downstream of the 0.8-mm trip ring forming clean cylinder-body junctions at the BOR surface. These cruciform tethers are cleated to the internal structure of the BOR, and run diagonally across the test-section shown in figure 1. Outside the test-section, the tethers are connected to a manual slide on each side of the ceiling and stabilized under the floor by 14.5-kg weights. The characteristics of the tether wake and its highly-constrained influence on the BOR boundary layer was discussed in detail by BHAD. Additionally, the acoustic contamination to the surface mics was tonal at about 4500-Hz (corresponding to a Strouhal number of 0.19) and its harmonics. While this was removed from the wall-pressure spectrum, the discussion in §3 is limited to frequencies less than 4000-Hz further ensuring the disturbance does not impact the conclusions.

The BOR was positioned to a $0 \pm 0.25°$ angle-of-attack with the circumferential uniformity in the mean surface pressure confirmed with a ring of pressure taps on the nose, followed by the stagnation pressure measurements at the BOR tail (see figure 6 of BHAD). When positioned at a zero angle-of-attack, the BOR installation poses a 4.3% blockage in the tunnel. The flow structure on the tail cone were documented extensively, using a combination of hotwire anemometry and particle Image velocimetry (PIV). Using a single hotwire, fifteen profiles were obtained documenting statistics and temporal structure of the streamwise velocity, detailed in §2.4 in BHAD. Though most profiles are not directly over the surface microphones, the flow parameters required to examine the wall pressure structure are estimated from simple interpolation due to adequate resolution.

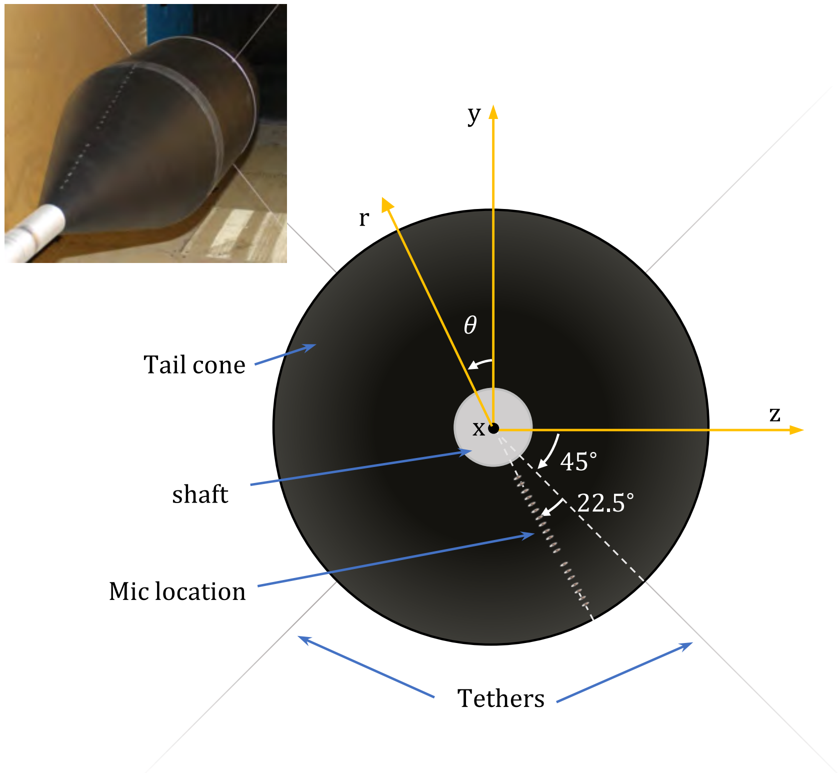

Figure 2: Schematic showing the circumferential location of the surface mics on the tail cone with respect to the tethers. The view corresponds to as seen by an observer located downstream of the BOR and viewing directly downstream.

2.1. *Fluctuating wall pressure measurements*

The fluctuating wall pressure was measured on the BOR tail with a linearly-spaced and longitudinally arranged array of 15 Sennheiser electret microphones (type KE-4-211-2). Shown in figure 2 the microphones were installed 67.5° away from the horizontal (or $\theta = 292.5°$), such that the array was circumferentially separated from the closest tether by about 22.5°. This ensured that the microphones were free from any hydrodynamic interference as the half-width of the wake outside the tail boundary layer (x/D=3.172) was less than 5° (discussed by BHAD). Furthermore, the boundary layer statistics in the BOR boundary layer directly downstream of the tether showed no explicit variation from other circumferential stations suggesting that the turbulence contributing to the wall pressure is independent of the tether wakes.

Figure 3 shows the exact longitudinal arrangement on the tail, where the mics nominally by 12.7-mm arranged between $x/D = 2.53$ to 3.08, capturing the longitudinal structure of the wall pressure over the second-half of the tail. Each mic was fitted with 1-mm pinhole cap, yielding a flat frequency response between 50-20,000 Hz. Primary measurements were made at the design Reynolds number based on the BOR length of Re_L=1.92×10^6, matching that of the turbulence measurements. Additional pressure measurements were made across Reynolds numbers ranging from Re_L=1.12 x 10^6 to 2.40 x 10^6 (in steps of 0.16 x 10^6). All measurements were made with a 24-bit Bruel & Kjaer LAN-XI acquisition system sampling at 65,536 Hz for 32 seconds, and anti-alias filtered at 25,600 Hz. The one-sided spectral density was estimated using the fast-Fourier transform algorithm in

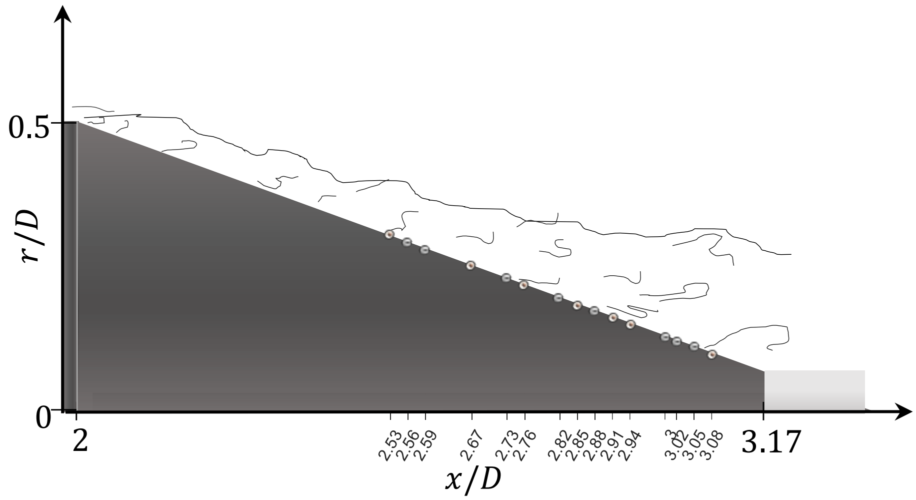

Figure 3: Longitudinal arrangement of the surface mics on the BOR tailcone. The microphones are arranged on the rear-half of the tail with a nominal spacing of 12.5-mm

MATLAB by segmenting the time series into 511 blocks of 8192 samples in each block, along with a 50% overlap and Hanning window.

3. Results and Discussion

Results are discussed in the co-ordinate system (x, y, z) centered at the BOR nose as shown earlier in figure 1, where x is along the axis of symmetry or the approach flow, y-axis points vertically upward and z-axis completing a right-handed system. In the corresponding cylindrical co-ordinate system (x, r, θ), r is the radial distance from the x-axis and θ is the polar angle, measured from the vertical (y-axis) by the right-hand rule (see figure 2).

3.1. *Flow characteristics and parameters*

The structure of boundary layer on the tail was the object of BHAD where they investigated the combined effects of a strong adverse pressure gradient and lateral curvature on the outer regions of the boundary layer. The flow was characterized as a rapidly decelerating flow over a large-cylinder where the axial pressure gradients primarily drive the turbulence evolution. The mean-flow was axisymmetric to within 2% in the streamwise velocity and to within 7% in the turbulence intensity. Though the flow was attached to the wall, it was increasingly diverging and aligned with the BOR axis as it decelerated under the adverse gradient (figure 9 in BHAD). Furthermore, the flow was found to be in disequilibrium, with the skin-friction coefficient (C_f), the shape-factor (H), and the momentum thickness based Reynolds number (Re_{δ_2}) significantly varied along the tail. One important feature was the development of inflection points in the velocity profiles at a position that corresponded to the turbulence stress peak in the outer region. Drawing similarity with a free-shear layer type behavior, it was observed that the mean flow statistics were self-similar with the embedded shear layer scaling proposed by Schatzman & Thomas (2017). Further, they also conjectured that the non-linear interactions could be important, particularly closer to the wall due to high local turbulence intensity (∼30%) where the convection velocity was found to be much greater than the local mean speed.

x/D	U_∞ (ms^{-1})	U_e	δ (m)	δ_1 (m)	H $(=\delta_1/\delta_2)$	Re_{δ_2}	U_τ/U_∞	Re_τ	C_f	β_C
2.53	21.7	21.22	0.0271	0.0105	2.42	5429	0.0243	896	0.0014	11.02
2.56	21.7	21.12	0.0287	0.0113	2.43	5783	0.0239	931	0.0014	11.17
2.59	21.7	20.99	0.0302	0.0121	2.45	6122	0.0235	964	0.0013	11.47
2.67	21.7	20.69	0.0346	0.0143	2.50	7043	0.0223	1052	0.0012	14.42
2.73	21.7	20.45	0.0384	0.0162	2.54	7814	0.0215	1123	0.0011	16.18
2.76	21.7	20.32	0.0404	0.0173	2.56	8229	0.0210	1158	0.0011	16.63
2.82	21.7	20.15	0.0445	0.0194	2.61	9028	0.0201	1218	0.0010	15.18
2.85	21.7	20.07	0.0466	0.0205	2.64	9420	0.0196	1242	0.0010	14.08
2.88	21.7	20.01	0.0489	0.0218	2.66	9908	0.0191	1272	0.0009	13.71
2.91	21.7	19.96	0.0513	0.0232	2.69	10410	0.0186	1301	0.0009	13.43
2.94	21.7	19.91	0.0238	0.0245	2.71	10922	0.0180	1325	0.0008	13.33
3.00	21.7	19.85	0.0593	0.0276	2.77	12013	0.0170	1373	0.0007	14.28
3.02	21.7	19.83	0.0612	0.0287	2.80	12360	0.0166	1385	0.0007	14.16
3.05	21.7	19.80	0.0641	0.0306	2.87	12841	0.0160	1397	0.0007	12.82
3.08	21.7	19.76	0.0671	0.0325	3.93	13323	0.0152	1396	0.0006	11.48

Table 1: Flow parameters at the mic locations. C_f, U_τ are obtained from large eddy simulations on the BOR at matched Reynolds number (Zhou *et al.* 2020).

Table 1 presents the various flow parameters that will be used to examine the characteristics of the wall pressure. Note that the parameters are interpolated estimates based on the hotwire measurements from approximately close streamwise positions. Here, U_∞ is the tunnel free-stream velocity which is a constant at 21.7-ms^{-1}, corresponding to a Reynolds number $U_\infty L/\nu = 1.2{\times}10^6$ based on the BOR length ($L = 1.369$ m). The boundary layer thickness δ was defined as the radial distance from the surface where the turbulence intensity (of the streamwise velocity U_s) has decayed to 2% of U_∞; The velocity at this location corresponds to the edge velocity U_e. The table also shows other parameters including the displacement thickness δ_1, shape-factor, and the momentum thickness Reynolds number $Re_{\delta_2} = U_e\delta_2/\nu$ which varies from about 5400 at the upstream mic to about 13300 at the downstream mic.

Since friction velocity is a critical parameter associated with the wall-pressure and since we do not have either direct measurements or any established hypothesis for APG flows, we rely on Reynolds-number matched wall-resolved large-eddy simulations (Zhou *et al.* 2020). While this could be a bold decision, detailed comparisons of the mean pressure (figure 7 of BHAD) and fluctuating surface pressure (figure 12, Zhou *et al.*) between the measurement and simulations were in agreement. In particular, the auto-spectrum of the fluctuating pressure were generally consistent to within 2-dB and in the viscous f^{-5} regions – where the viscous scales are expected to define the behavior – the agreement was even closer, to within 1 dB. Furthermore, we also observed that the viscous-scaling, (with $f\nu/u_\tau^2$ and τ_w as the pressure-scale) collapsed the viscous roll-off regions from all the streamwise locations to within 2 dB which otherwise showed about a variation of about 20-dB. Table 1 contains the estimates of friction-velocity, and other derived parameters: skin-friction coefficient, and Re_τ and Clauser's pressure gradient parameter $\beta_C = \delta_1/\tau_w(dp_s/dx)$. The variations in each of the parameters further confirm the non-equilibrium character of the flow.

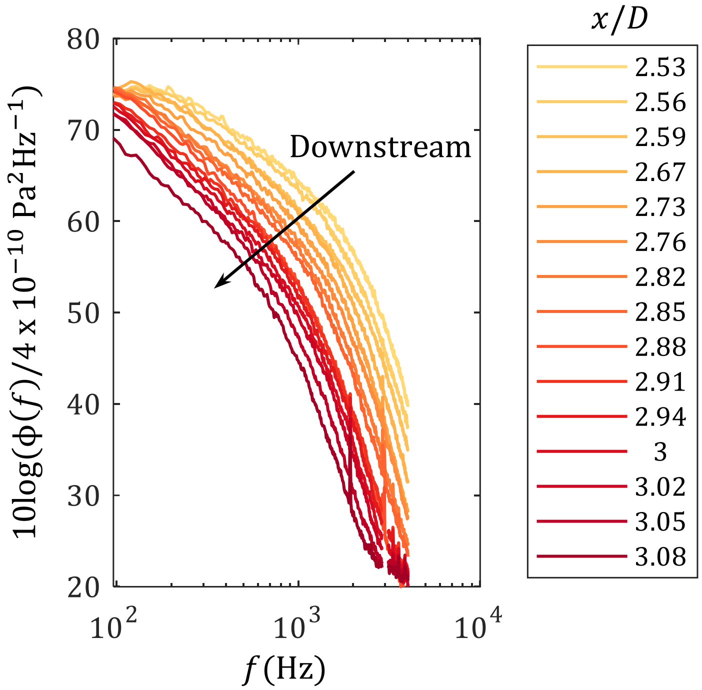

Figure 4: Dimensional auto-spectra of the wall pressure fluctuations $\phi(f)$ for various streamwise positions on the tail. The spectra is normalized with $p_{ref} = 20\mu Pa$ to show te sound pressure level (SPL). Legend shown towards the right of the figure, where the color shifts from bright to dark on going downstream

3.2. *Wall pressure spectrum: trends and scaling*

The dimensional autospectra for various streamwise stations are shown in figure 4, with frequency on the horizontal axis and spectral density $\phi(f)$ normalized on $p_{ref} = 20\mu Pa$ on the vertical axis, shown as sound pressure level. Before any interpretation, data for frequencies $f < 100$-Hz is excluded due to potential contamination from the facility-noise (Meyers *et al.* 2015), in addition to data at $f > 4000$ Hz since the signal-to-noise ratio was less than 10-dB. This automatically excludes the acoustic tones from the tethers (at $f \approx$4500-Hz and its harmonics) from the subsequent analysis. Additionally, the residual sharp spikes $f \sim 2$ kHz and 4 kHz, visible only for the most downstream mics, correspond to the acoustic tones due to the streamlined strut and are left since they are not expected to alter the interpretation of results.

Another important aspect is the high-frequency attenuation due to the finite size of sensor which could be important for non-dimensional sensing diameter $d^+ = du_\tau/\nu > 18$ (Gravante *et al.* 1998; Schewe 1983). For example, for a sensing diameter of $d^+ = 26$, Gravante *et al.* observed a 2-dB attenuation at $f^+_{2dB} = f\nu/u^2_\tau = 2.2$. In our case d^+ varies between 20 to 35, moderately close to the threshold of 18. However, assuming that the 2-dB attenuation frequency varies inversely with the pinhole diameter, following the arguments of Meyers *et al.* (2015), the highest observed d^+ of 35 yields a frequency of about 23 kHz, which exceeds the already adopted 4-kHz cut-off; Therefore no corrections to the measured spectra are performed.

Observing the spectrum as the flow decelerates downstream (color changes from bright to dark) there is a broadband reduction in the sound pressure level which intensifies with frequency. For example, from x/D =2.53 to 3.08, which is 0.51-m or about 9δ, there is about a 10-dB reduction at $f \sim$200-Hz that increases to over 30-dB at $f \sim$2000-Hz. This general weakening of the pressure signature, which is enhanced for higher frequency, is in contrast to Willmarth & Yang (1970)'s work on lateral curvature effects; They observed a general redistribution of the energy from larger scales to smaller ones, with the total energy remaining similar to the flat-plate case. This could imply that the broadband reduction is primarily driven by the adverse mean pressure gradient and is consistent with the APG studies of Catlett *et al.* (2015) and Hu & Herr (2016). Investigating non-equilibrium flows, they observed the spectrum to shift towards lower frequencies as the flow decelerated downstream, such that the low frequency content ($f <$500-Hz) amplified while the high frequency content weakened. This is consistent with the trends in figure 4 except the low-frequency amplification, which is very likely for frequencies not shown here, as hinted by the spectrum from various locations converging near 100-Hz.

Despite a significant reduction in the sound pressure levels, it is interesting to see that the functional form of the spectra appears to remain somewhat similar; To investigate this quantitatively, we examine the non-dimensional spectra through various scales for pressure and frequency. First, we examine the familiar mixed-scaling, with τ_w as the pressure-scale and U_e/δ as the frequency scale, referred to here as the wall-wake scaling and shown in figure 5(a). Interestingly, the resulting non-dimensional spectrum from all locations, across the measured frequency range ($0.1 < f\delta/U_e < 10$), collapse to within 2-dB. Furthermore, while the data at lower frequencies is inadequate to examine the slope of the rise, the mid-frequency region appears to decay roughly as $f^{-1.5}$ with some streamwise dependence. This significant deviation from the theoretical f^{-1} decay for ZPG flows – where the log-layer motions are expected to contribute (Panton & Linebarger 1974) – is consistent with the results of Hu & Herr (2016) and Cohen & Gloerfelt (2018). However, the spectra decay as f^{-5} in the viscous roll-off region is consistent with the ZPG studies, suggesting that both APG and lateral curvature have little influence on the energy-transfer mechanisms at the viscous scales.

We would like to draw particular attention to two major counter-intuitive aspects of the wall-wake scaling in figure 5. First, τ_w appears to be the pressure-scale notwithstanding a strong APG where previous works have proposed outer scales such as the maximum Reynolds shear stress τ_M (Simpson *et al.* 1987; Abe 2017) or the free-stream dynamic pressure $Q = \frac{1}{2}\rho U_e^2$ (Hu & Herr 2016; Cohen & Gloerfelt 2018). However, the root-mean-square pressure along the tail, despite dropping by over 60%, appears to be scale best with the wall-shear stress as shown in figure 5(b), plateauing at $\sim 7\tau_w$. Similar charts based on τ_M and Q showed significant variations, dropping from $4\tau_M$ to $1\tau_M$ and from $0.01Q$ to $0.004Q$. This suggests that as long as the flow attached, the skin-friction producing motions are an important source of the fluctuating wall-pressure even for a strong APG flow. However, it is possible that Q or τ_M may be more successful in scaling the pressure spectra from multiple studies with different flow histories, as suggested by Cohen & Gloerfelt (2018).

The second confounding aspect is the broadband success of the wall-wake scaling that extends to even the viscous regions, where one expects the viscous-scale u_τ^2/ν to dictate the behavior. While the viscous scaling indeed produces a similar collapse in the high-frequency roll-off regions as shown in figure 6(a), it appears to be influenced by the outer timescale δ/U_e. Figure 5(c) shows the viscous-time scale ν/u_τ^2 along the tail, plotted as a function of the outer time-scale δ/U_e; Shown in a log scale, the viscous timescale appears to rise exponentially with δ/U_e. This coupling between the outer and viscous scales is consistent with recent works, which examine the interactions between the outer-region

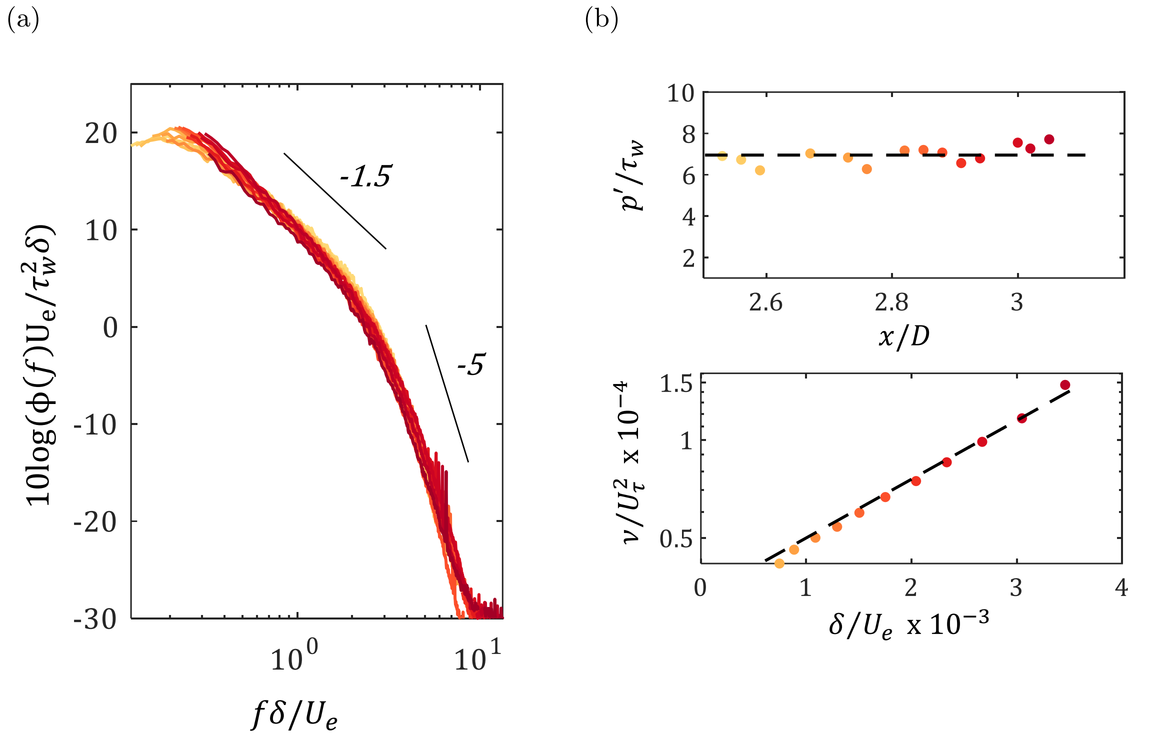

Figure 5: (a) Non-dimensional auto spectra of the fluctuating pressure with frequency normalized on the outer-scale (U_e/δ) and pressure scaled with shear stress at the wall (τ_w). (b) Root mean square of the fluctuating pressure along the tail scaled on τ_w. (c) The viscous time-scale along the ramp shown as a function of the outer scale of the flow.

large scale motions and the near-wall turbulence. For example, Harun *et al.* (2013) and Dróżdż & Elsner (2013) used scale decomposition analysis to show that the modulation of the near-wall turbulence (in both frequency and amplitude) by the large-scale motions in moderate APG flows was stronger than in a ZPG layer at similar Re_τ. Furthermore, Yoon *et al.* (2018) observed that the contribution of large-scale motions ($\mathcal{O}(\delta)$) to the skin-friction was enhanced by APG (with β_C=1.45 in their case). These effects are only expected to be stronger in our case, due to much stronger APG, by an order of magnitude.

Recent work in strong APG flows (Balantrapu *et al.* 2021; Schatzman & Thomas 2017; Kitsios *et al.* 2017; Skåre & Krogstad 1994) has presented evidence for a fundamental change in the structure of the boundary layer, with an increased turbulence activity in the outer-regions that correspond to inflection points in the mean velocity profile, hypothesizing a free-shear layer like behavior. Building on the work of Schatzman & Thomas (2017), Balantrapu *et al.* (2021) showed that the mean flow and turbulence structure of the current BOR flow was roughly similar with an embedded shear layer (ESL) scaling, which is based on the properties at the inflection point; With the velocity defect at the inflection point ($U_d = U_e - U_{IP}$) as the velocity scale and the vorticity thickness (δ_ω) as the length-scale. The wall-pressure spectrum normalized with the ESL scaling is shown in figure 6(b). Here, the frequency is scaled with U_e/δ_ω while the pressure is scaled with τ_w. While the collapse is poor ($\sim$ 4 dB) in comparison to that of wall-wake scaling ($\sim$ 2 dB), this appears to be associated with the higher uncertainty in the estimation of ESL parameters as discussed by BHAD; Fundamentally, the ESL time-scales, δ_ω and U_e were shown by BHAD to be directly proportional to the outer scales,

(a) (b)

(c) (d)

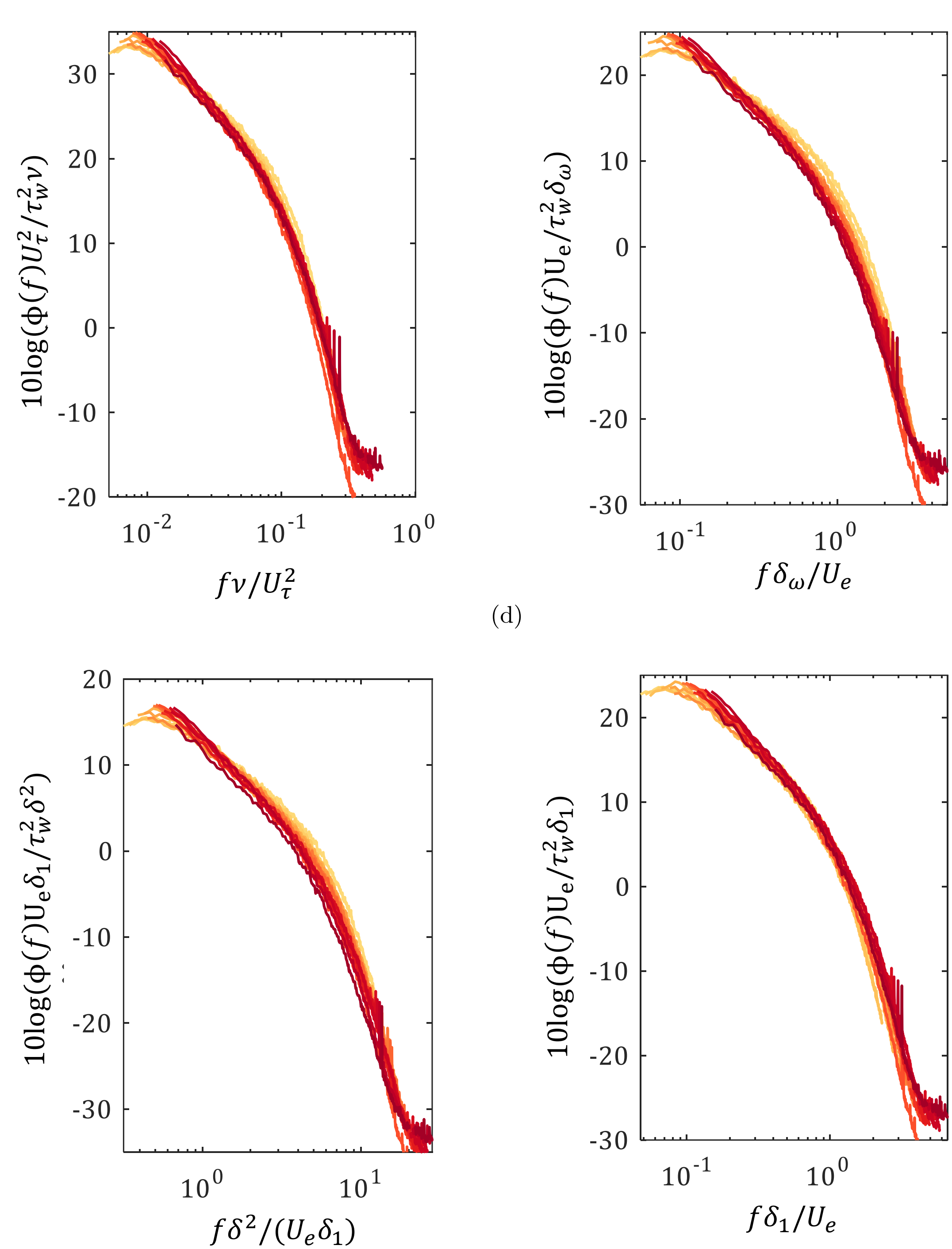

Figure 6: Non-dimensional wall pressure spectra with other candidate time-scales, where τ_w is the pressure-scale.(a) Viscous scaling with $f\nu/u_\tau^2$ (b) Embedded shear layer scaling, with $f\delta_\omega/U_e$. (c) Zagarola-Smits scaling fU_{zs}/δ where $U_{zs} = U_e\delta_1/\delta$. (d) Displacement thickness scaling $f\delta_1/U_e$.

δ and U_e respectively, with

$$\delta_\omega/\delta = U_d/U_e = 0.4 \pm 0.05 \tag{3.1}$$

suggesting that the success of the ESL scaling should in principle be equivalent to the wall-wake scaling. Note that τ_w is retained as the pressure-scale since the collapse with the dynamic pressure based on the defect-velocity $Q_d = \frac{1}{2}\rho U_d^2$ resulted in a much weaker collapse, with a spread of over 8-dB per Hz, confirming that τ_w is the clear pressure scale. As a side-note, we examine the non-dimensional spectra with other recently proposed outer time scales for APG flows: the Zagarola-Smits scaling, δ/U_{zs} where $U_{zs} = U_e\delta_1/\delta$ (Maciel *et al.* 2018) and the displacement-thickness scaling δ_1/U_e (Kitsios *et al.* 2017), shown in figure 6(c-d). Generally, it appears that δ is the appropriate length-scale while U_e is the most suitable velocity scale.

To investigate the importance of the outer-region turbulence on the wall pressure spectrum, we consider the space-time structure of the wall pressure in the following section, examining the intermittent features and their relation to the corresponding flow structure.

3.3. *Space-time structure and relation to spectral scaling*

Figure 7 shows a subset of the instantaneous structure of the wall pressure along the tail. Here, contours of the pressure normalized on the p_{RMS} of the original signal are shown with the vertical axis representing the location on the tail, and the horizontal axis representing a 0.4 second time interval. These contours are characterized by forward leaning ridges which appear to alternate in the sign, with positive ridges (red) often succeeded by negative ones (blue). This is particularly evident in the top half of the chart (x/D = 2.8 to 3.1) due to a better spatial resolution. The forward inclination of the structure is consistent with the expected downstream convection of the pressure-producing motions with time. This is a particularly interesting and unexpected feature, as the convective features appear to be quasi-periodic, albeit appearing occasionally strong, and tend to remain coherent for extended distance, for $\Delta x \sim 0.55D$ (or 0.24 m) which translates to about 9δ.

Investigating these unexpected, quasi-periodic ridges and their relation to the structure of the flow may provide additional insight into the findings in § 3.2, specifically on the broadband success of the wall-wake scaling ($\tau_w; \delta/U_e$) on the wall pressure spectrum. Below we explore this feature beginning with an outline of the procedure used to extract the conditionally averaged structure through wavelet transform. We then examine the resulting structure and its characteristics such as the scaling, convection velocity, and differences when compared to a ZPG layer. Finally, we attempt to relate this feature to the time-varying structure of the overlying flow.

The continous wavelet transform is a suitable technique to study time-dependent and intermittent features of a random signal; It has been occasionally employed in the fluids research community, to identify the intermittent features in turbulent boundary layers (Camussi *et al.* 2008; Baars *et al.* 2015), reattaching flows (Lee & Sung 2002), and jet flows (Cavalieri *et al.* 2010; Grassucci *et al.* 2015). As the technique is well documented (Addison 2018; Farge 1992), it will only be briefly reviewed here. The principle is similar to Fourier-transform, where a localized wave-like function, known as the mother wavelet, forms the basis function instead of the harmonic functions used in Fourer-transform. The process involves convolution of the signal under study with a series of manipulated wavelets, decomposing the parent signal as a function of both frequency and time. This manipulations of the wavelet include a range of translations (along the time-axis) and

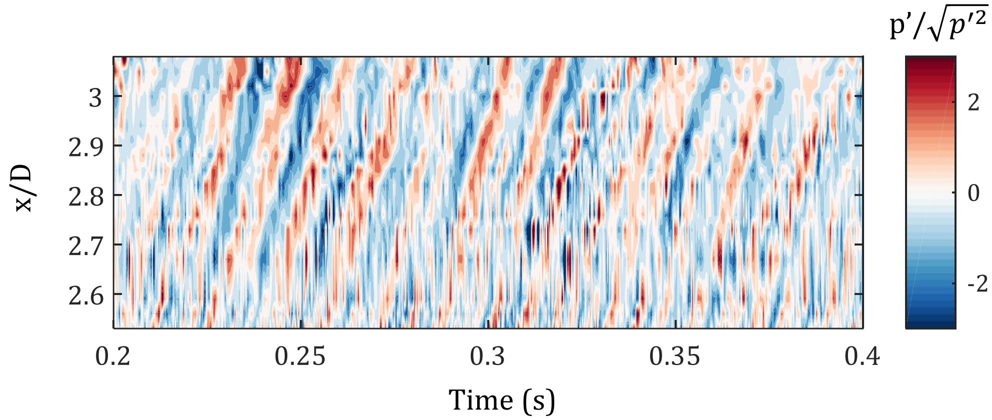

Figure 7: Snapshot of the instantaneous pressure along the ramp, with time on the horizontal axis, and position on the tail on the vertical axis. Contours represent the pressure normalized with the corresponding root-mean-square values. The snapshot corresponds to 0.2-seconds of a total of 32-seconds.

dilations (stretching and squeezing) of the mother wavelet, represented mathematically as

$$w(f,t) = C_{\psi}^{-1/2} \int_{-\infty}^{+\infty} \psi^* \left(\frac{t-\tau}{r} \right) p(\tau) d\tau \tag{3.2}$$

Where $\psi^*(\frac{t-\tau}{r})$ is the conjugate of the mother wavelet $\psi(t)$, that is translated by τ and is scaled by r, a factor representative of the inverse of frequency. $C_{\psi}^{-1/2}$ is the weighting function that ensures conservation of the energy, such that the inverse wavelet transform of $w(f,t)$ returns the parent signal $p(t)$. All work presented here has been performed in MATLAB with the Wavelet toolbox, using the generalized Morse wavelet (Olhede & Walden 2002). However, the following analysis has been shown to be independent of the chosen mother wavelet (Grassucci *et al.* 2015).

Figure 8(a) shows the pressure signal from a single location on the tail, x/D=3.0, showing a 0.2-second snapshot from a full 32-second block, with figure 8(b) revealing the associated wavelet transform output. With frequency on the vertical axis and time on the horizontal axis (with a resolution equal to the sampling interval), the contour levels in the frequency-time map represent the magnitude of the wavelet-coefficient, $|w(f,t)|$. This instantaneous spectral content of the parent signal clearly demonstrates the intermittent character of the pressure, represented by the high amplitude (red) spots occurring typically in the 100-Hz – 2000-Hz band.

In order to quantitatively analyse the intermittent, energetic features of the signal we use the so-called local intermittency measure (LIM; Farge (1992); Camussi *et al.* (2010)) defined as

$$LIM(f,t) = \frac{w(f,t)^2}{\langle w(f,t)^2 \rangle_t} \tag{3.3}$$

Here, $w(r,t)^2$ is a measure of the instantaneous energy of the signal which when integrated yields the energy spectrum as obtained in the Fourier-space. When normalized with the time-averaged energy $\langle w(r,t)^2 \rangle_t$, the resulting LIM accentuates the localized and significant contributions to the mean signal. Figure 9 shows the obtained result for the signal discussed above in figure 8(a-b). Here we can see that the larger LIM events occur occasionally, about 4 times in this case, and correspond to the high amplitude regions of

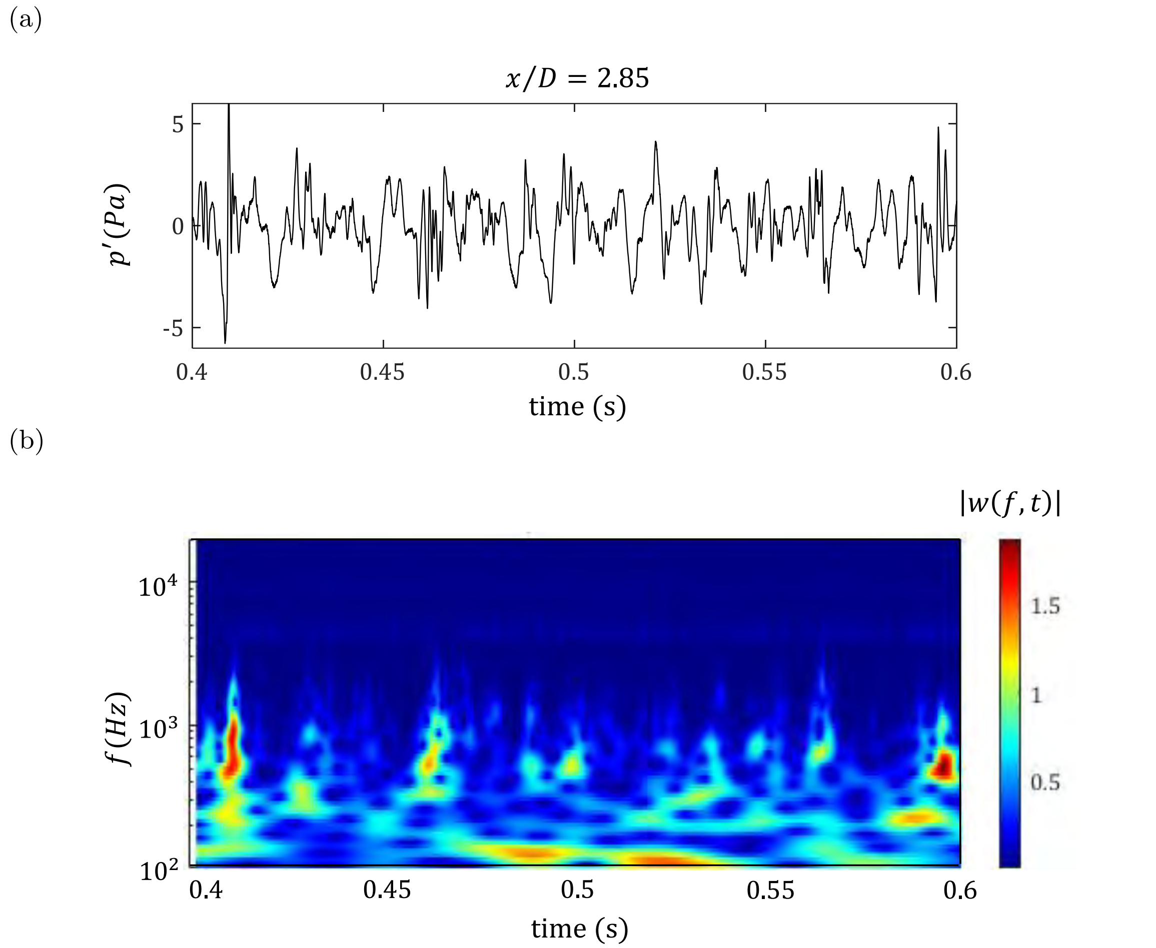

Figure 8: (a) Snapshot of the pressure signal at x/D=2.85 (b) Magnitude of the wavelet transform corresponding to the signal in (a)

the wavelet transform in figure 8. Furthermore, the high LIM events are not restricted to a particular scale but are stretched out between 300-Hz and 4000-Hz reflecting the broadband character of the turbulence. In order to extract these features and understand their structure we use a threshold to qualify a 'high' amplitude event and then determine the conditional structure from the ensemble average of all recorded significant events.

The choice of threshold must be high enough to distinguish the significant event from the general background, and low enough such that it is identified a number of times sufficient to ensure statistical convergence. From a quick study we determined that a threshold $\Gamma \approx 10$ satisfies this requirement, with no appreciable difference in the end-result for 9 - 12. However, for $\Gamma < 9$, background events start to corrupt the average structure while above 12, the number of events detected is increasingly insufficient for a statistically converged average. This observation is consistent with the more quantitative analysis of Grassucci *et al.* (2015). Through the prescribed threshold we are able to detect approximately 800 events in about 2×10^6 samples measured, and to check if the events are uncorrelated, one could verify an exponentially decaying tail in the probability density function of the time-delay between consecutive events ($t_o^i - t_o^{i-1}$). Every instance where LIM exceeds the threshold at any frequency f, an event is considered to have been detected and the start time of the event t_o^i is documented. Then the original pressure signal $p(t)$ is centered about t_o^i resulting in a conditional time series $p_i(t - t_o^i)$; Therefore

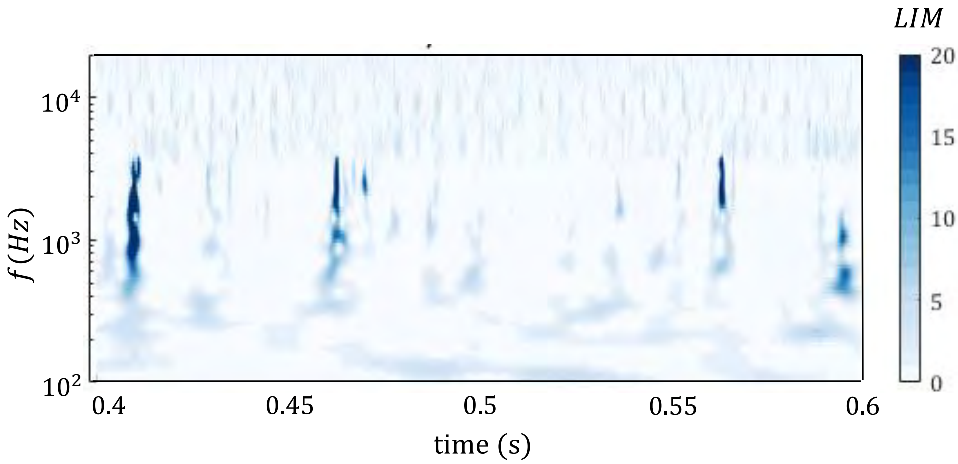

Figure 9: Contours of the large intermittency measure for a 0.2-second snapshot of the pressure signal at x/D=2.85, estimated from equation 3.3 based on the wavelet transform of the signal shown in figure 8(a-b).

the event identification is not limited to a particular frequency, preserving the original broadband character of the feature. This process is similarly repeated for all N identified events, and then ensemble averaged to yield the conditional structure

$$p_c(t - t_o) = \frac{1}{N}\sum_{i=1}^{N} p_i(t - t_o^i) \tag{3.4}$$

The resultant pressure structure at a single location on the tail, x/D=2.85, is shown in figure 10(a) with the vertical axis representing the pressure in Pascal and the horizontal axis showing the time-delay $t-t_o$. The conditioned pressure has a definite character, with a negative-trough that is immediately followed by a positive peak of a roughly equal magnitude, reflecting the instantaneous signature shown earlier in figure 7. At larger time-delay the signal, though slightly noisy, decays towards zero suggesting statistical convergence. This behavior, observed at all measured locations, is quite different from conditional studies in ZPG flows; The large-amplitude events of ZPG flows were associated with the buffer and log-region turbulence, with convection velocities corresponding to the local mean velocity, and positive peaks associated with an ejection and a negative trough with downward sweeping motion (Johansson *et al.* 1987; Schewe 1983). However, the conditional structure on the BOR tail is fundamentally different, with a strongly coupled trough and peak, which appears more like a coupled sweep-ejection or rather the pressure-footprint of a convecting roller eddy. Furthermore, the signatures from all streamwise stations are shown in figure 10(b) with the pressure normalized on τ_w and the time on δ/U_e. The amplitude of this signature appears to scale with the wall-shear stress, yielding a peak-magnitude of 2 - 3.5 τ_w and the time-period appears to be about $4\delta/U_e$. This is consistent with the success of the wall-wake scaling in collapsing the wall pressure spectrum.

This feature is also reflected in the space-time correlations shown in 11(a-c), obtained without any conditioning, defined as

$$R_{pp} \equiv E[p(x,t)p(x+\xi, t+\tau)] \tag{3.5}$$

where ξ is the longitudinal separation along the tail, and τ corresponds to the time-

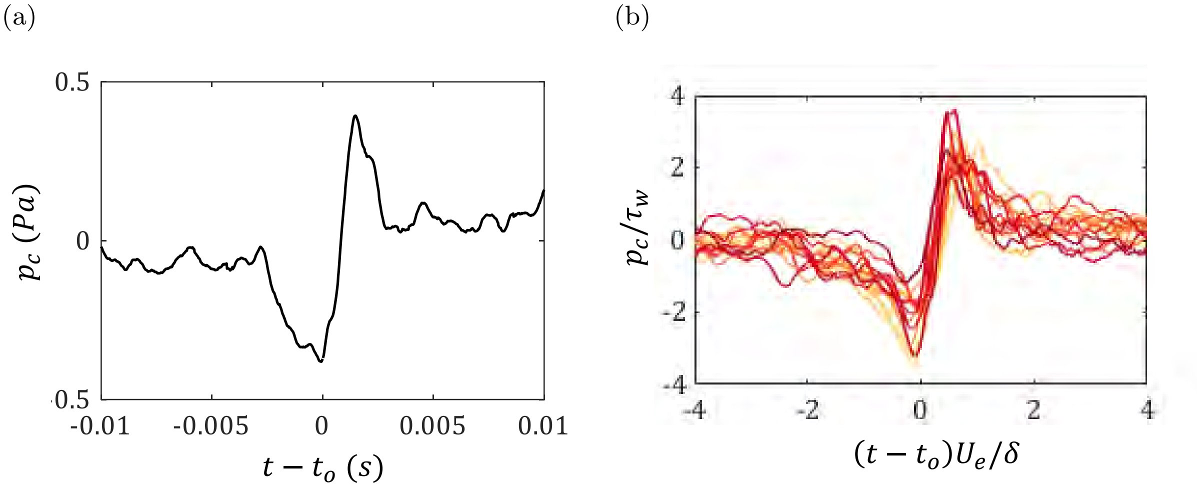

Figure 10: (a) The conditional structure of the wall pressure at $x/D = 2.88$ (b) Conditional structure from all streamwise stations, with the pressure normalized on the local wall shear-stress τ_w and the time-delay normalized with the outer-time scale δ/U_e.

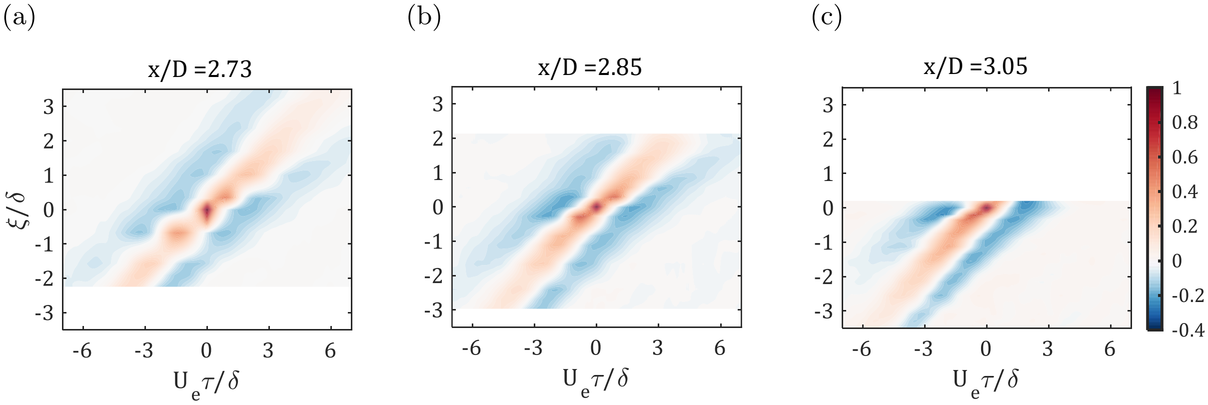

Figure 11: Space-time correlation function of the wall pressure show at representative locations on the tail. See equation 3.5 for definition. (a) x/D = 2.73, (b) x/D = 2.85, (c) x/D = 3.05.

delay. Results are shown for representative stations along the tail, with x/D of 2.73, 2.85, 3.05, in figure 11 a, b, and c respectively. Furthermore, in each case correlation is normalized by the corresponding mean-square value resulting in a maximum of 1 that corresponds to the auto-correlation ($\xi = \tau = 0$). Such maps are generally characterized by a narrow diagonal band along which most of the energy is concentrated. This is often referred to as the convective ridge, it implies that the pressure-producing motions, despite evolving, remain correlated as they convect downstream with time. In addition to the convective ridge observed in ZPGTBL flows (Choi & Moin 1990), we observe negative off-diagonal bands with peak levels of -0.4. This is consistent with our observation of the wave-like conditional structure where a negative lobe was clearly coupled to a positive one. Furthermore, at zero spatial separation, i.e along the horizontal line corresponding to $\xi/\delta = 0$ the time-delay corresponding to a decayed correlation is close to the time-scale of the conditional structure.

Now assuming that the pressure-producing motions are convecting at the local mean velocity, we can ascertain their tentative location in the boundary layer if we know the

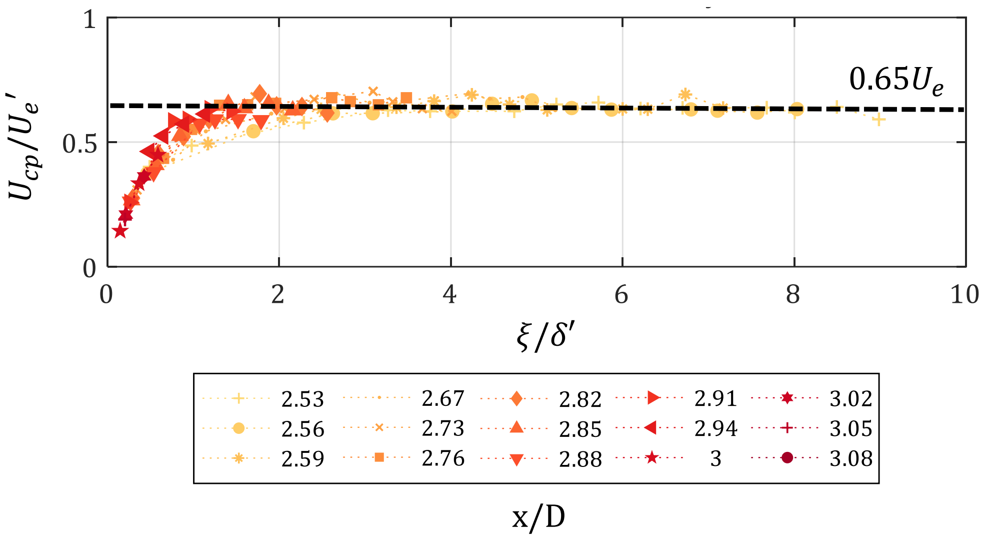

Figure 12: Phase convection velocity of the wall pressure shown as a function of spatial separation between the probes, normalized on the boundary layer thickness. Each curve corresponds to an anchor microphone position, with the corresponding color and symbols shown in the legend above.

convection velocity of the quasi-periodic feature; A rudimentary estimate based on the slope of the forward-leaning ridges seen in the instantaneous structure (figure 7) is about $0.6U_e$, which corresponds to the outer regions in the layer, specifically the location of the inflection points in the mean velocity profiles. However, to confirm the preliminary estimates of the convection speed, we consider the phase-convection velocity estimated from the slope of the phase-spectrum between two mics as

$$U_{cp} = \frac{\xi}{\tau} \tag{3.6}$$

where $\xi = x - x'$ is the separation between the mics with x' corresponding to the anchor mic, and τ is the slope of the phase-spectrum which corresponds to the slope of the phase-spectrum between the microphones. This process is then repeated with respect to all mics, providing the convection velocity as a function of spatial separation, as shown in figure 12. While the vertical axis represents the convection velocity U_{cp} normalized with the edge velocity at the anchor microphone U_e', the horizontal axis represents the spatial separation ξ normalized on δ . Here, the results obtained for various anchor positions along the tail are included, with a darker color representing a downstream anchor location (see associated legend below). Generally, the convection velocity increases with separation and asymptotes to about $0.65U_e$ for $\xi/\delta > 2$; For smaller separations one would expect the small-scale turbulence occurring near the wall to dominate the correlations, resulting in a lower convection velocity consistent with the lower mean speeds near the wall. However, these small scale fluctuations appear to decorrelate at larger separations, such that the large-scale motions dominate the correlation, which are centered away from the wall and convect at relatively faster speeds. Furthermore, the $0.65U_e$ asymptote is consistent with the rudimentary, ruler-based estimate from figure 7 suggesting that the motions, with the quasi-periodic pressure footprints, are centered in the outer regions, specifically where the inflection points in the mean velocity, and the Reynolds stress peaks are located (see figure 15 in BHAD).

The existence of these quasi-periodic motions that track the inflection point provides evidence in favor of embedded shear layer hypothesis for strong adverse pressure gradient boundary layers. Furthermore, it is clear that the shear-layer motions play a significant role in the near-wall turbulence and on the wall pressure, supporting the broadband success of the wall-wake scaling on the wall-pressure spectrum. However, if the outer-layer motions are such significant sources for the wall pressure one would expect an outer region scale – such as the maximum shear stress or the dynamic pressure – to dictate the wall pressure amplitude instead of τ_w as observed. One likely explanation stems from a scenario where the large-scale shear-layer motions are superposed on the underlying boundary layer turbulence with its associated near-wall cycle. In this case, the shear-layer motions would drive the wall pressure dynamics not by directly slapping the wall but instead by playing a strong but indirect role through modulation of the near-wall boundary layer turbulence and therefore influencing both the skin-friction and wall-pressure. Further investigation into these aspects can be performed by rigorous examination of the source terms in the pressure-Poisson equation, including the pressure-gradient terms in the mean-shear terms, in addition to the non-linear terms. An alternate and simpler approach is to examine the contribution of the shear-layer motions to the wall pressure spectrum analytically, with a mathematical model that captures the essential features of the convecting roller eddies, similar to the work of Dhanak *et al.* (1997) on the contribution of hair-pin vortices.

4. Conclusions

This work presents the wall pressure signature of an axisymmetric boundary layer under a strong adverse pressure gradient. Measurements were made on the tail of a body-of-revolution with a longitudinal array of surface mounted microphones, documenting the fluctuating pressure imposed by a sharply decelerating non-equilibrium boundary layer. The wall pressure spectrum, and its scaling are discussed along with the space-time structure to reveal the combined effects of adverse pressure gradient and lateral curvature. The dataset is publicly available at (will be included after revisions)

As the flow decelerates downstream, the mean-square pressure drops together with the wall-shear stress (τ_w), and is consistently about $7\tau_w$. The associated dimensional spectrum weakened significantly, with a broadband reduction of over 15 dB per Hz. Much of this variation seems to be tracked by the wall-wake scaling, where τ_w is the pressure scale and δ/U_e is the timescale. Here δ is the boundary layer thickness and U_e is the edge velocity.

The reasons for broadband success of the wall-wake scaling, even in the viscous f^{-5} regions were examined by considering the space-time structure of the wall pressure. Preliminary examination of the instantaneous fluctuations revealed the presence of a quasi-periodic feature that appeared to remain correlated over measured longitudinal extent, which was over 9δ. Detailed investigation through wavelet transform revealed a conditional structure, with a strongly coupled negative trough followed by a positive peak: indicative of a convective roller. Furthermore, the amplitude and time-scale of this feature appeared to be scale with τ_w and δ/U_e reminiscent of the success of the wall-wake scaling on the pressure spectrum.

Furthermore, these features were observed to convect at speeds matching those at the inflection point in the mean velocity profile and the outer turbulence stress peak, providing evidence to the embedded shear layer hypothesis for strong adverse pressure gradient flows. However, the success of τ_w despite the evident role of the outer layer motions is discussed with reference to a scenario where the large-scale embedded layer turbulence is superposed on the underlying near-wall boundary layer turbulence; It is hypothesized that the shear-layer motions play a strong but indirect role by modulating the near-wall turbulence and consequently the wall-friction and pressure. Suggestions are made as to further investigation to evaluate the hypothesis.

Acknowledgments

The authors acknowledge the Office of Naval Research, in particular Drs. Ki-Han Kim and John Muench for providing financial support through grants N00014-17-1-2698 and N00014-20-1-2650. The authors also recognize the crucial contributions of Christopher Hickling and Anthony Millican with CAD and wind tunnel testing. The authors would like to thank Di Zhou and Dr. Meng Wang at University of Notre Dame for sharing the data from their large eddy simulations. We would also like to thank Drs. Stewart Glegg, William Blake, Jason Anderson, and Mr. Michael Marcolini for helpful discussions and advice on the project. Thanks also go to the AOE machine shop headed by James Lambert, the wind-tunnel staff Dr. Aurilien Borgoltz and Bill Oetjens, and all graduate assistants towards the preparation and measurements.

Declaration of interests

The authors report no conflict of interest.

REFERENCES

Abe, Hiroyuki 2017 Reynolds-number dependence of wall-pressure fluctuations in a pressure-induced turbulent separation bubble. *Journal of Fluid Mechanics* **833**, 563–598.

Addison, Paul S. 2018 Introduction to redundancy rules: the continuous wavelet transform comes of age **376** (2126), 20170258.

Baars, WJ, Talluru, KM, Hutchins, N & Marusic, I 2015 Wavelet analysis of wall turbulence to study large-scale modulation of small scales. *Experiments in Fluids* **56** (10), 188.

Balantrapu, N. Agastya, Hickling, C., Alexander, William N. & Devenport, William J. 2021 The structure of a highly-decelerated axi-symmetric turbulent boundary layer. *Journal of Fluid Mechanics* ((under review)).

Blake, William K 2017 *Mechanics of flow-induced sound and vibration, Volume 2: Complex flow-structure interactions*. Academic press.

Bokde, Arun L. W., Lueptow, Richard M. & Abraham, Bruce 1998 Spanwise structure of wall pressure on a cylinder in axial flow. *Physics of Fluids* **11** (1), 151–161.

Bradshaw, P. 1967 'inactive' motion and pressure fluctuations in turbulent boundary layers. *Journal of Fluid Mechanics* **30** (2), 241–258.

Bull, M.K. 1996 Wall pressure fluctuations beneath turbulent boundary layers: Some reflections on forty years of research. *Journal of Sound and Vibration* **190** (3), 299–315.

Camussi, R., Grilliat, J., Caputi-Gennaro, G. & Jacob, M. C. 2010 Experimental study of a tip leakage flow: wavelet analysis of pressure fluctuations. *Journal of Fluid Mechanics* **660**, 87–113.

Camussi, R., Robert, G. & Jacob, M. C. 2008 Cross-wavelet analysis of wall pressure fluctuations beneath incompressible turbulent boundary layers. *Journal of Fluid Mechanics* **617**, 11–30.

Catlett, M Ryan, Anderson, Jason M, Forest, Jonathan B & Stewart, Devin O 2015 Empirical modeling of pressure spectra in adverse pressure gradient turbulent boundary layers. *AIAA Journal* **54** (2), 569–587.

Cavalieri, André V. G., Jordan, Peter, Gervais, Yves, Wei, Mingjun & Freund, Jonathan B. 2010 Intermittent sound generation and its control in a free-shear flow. *Physics of Fluids* **22** (11), 115113.

Chase, D. M. 1980 Modeling the wavevector-frequency spectrum of turbulent boundary layer wall pressure. *Journal of Sound and Vibration* **70** (1), 29–67.

Choi, Haecheon & Moin, Parviz 1990 On the space-time characteristics of wall-pressure fluctuations. *Physics of Fluids A: Fluid Dynamics* **2** (8), 1450–1460.

Cohen, Elie & Gloerfelt, Xavier 2018 Influence of pressure gradients on wall pressure beneath a turbulent boundary layer. *Journal of Fluid Mechanics* **838**, 715–758.

Corcos, G. M. 1964 The structure of the turbulent pressure field in boundary-layer flows. *Journal of Fluid Mechanics* **18** (3), 353–378.

Devenport, William J., Burdisso, Ricardo A., Borgoltz, Aurelien, Ravetta, Patricio A., Barone, Matthew F., Brown, Kenneth A. & Morton, Michael A. 2013 The kevlar-walled anechoic wind tunnel. *Journal of Sound and Vibration* **332** (17), 3971–3991.

Dhanak, Manhar R., Dowling, Ann P. & Si, Chao 1997 Coherent vortex model for surface pressure fluctuations induced by the wall region of a turbulent boundary layer **9** (9), 2716–2731.

Dróżdż, Artur & Elsner, Witold 2013 Amplitude modulated near-wall cycle in a turbulent boundary layer under an adverse pressure gradient. *Archives of Mechanics* **65** (6), 511–525.

Farge, Marie 1992 Wavelet transforms and their applications to turbulence **24** (1), 395–458.

Glegg, Stewart & Devenport, William 2017 *Aeroacoustics of low Mach number flows: fundamentals, analysis, and measurement*. Academic Press.

Goody, Michael 2004 Empirical spectral model of surface pressure fluctuations. *AIAA Journal* **42** (9), 1788–1794.

Grasso, G., Jaiswal, P., Wu, H., Moreau, S. & Roger, M. 2019 Analytical models of the wall-pressure spectrum under a turbulent boundary layer with adverse pressure gradient. *Journal of Fluid Mechanics* **877**, 1007–1062.

Grassucci, Daniele, Camussi, Roberto, Jordan, Peter & Grizzi, Silvano 2015 Intermittency of the near pressure field induced by a compressible coaxial jet. *Experiments in Fluids* **56** (2), 23.

Gravante, S. P., Naguib, A. M., Wark, C. E. & Nagib, H. M. 1998 Characterization of the pressure fluctuations under a fully developed turbulent boundary layer. *AIAA Journal* **36** (10), 1808–1816.

Harun, Z., Monty, J. P., Mathis, R. & Marusic, I. 2013 Pressure gradient effects on the large-scale structure of turbulent boundary layers. *Journal of Fluid Mechanics* **715**, 477–98.

Hu, Nan & Herr, Michaela 2016 Characteristics of wall pressure fluctuations for a flat plate turbulent boundary layer with pressure gradients. In *22nd AIAA/CEAS Aeroacoustics Conference*, p. 2749.

Johansson, Arne V., Her, Jen-Yuan & Haritonidis, Joseph H. 1987 On the generation of high-amplitude wall-pressure peaks in turbulent boundary layers and spots. *Journal of Fluid Mechanics* **175**, 119–142.

Kamruzzaman, M., Bekiropoulos, D., Lutz, Th., Würz, W. & Krämer, E. 2015 A semi-empirical surface pressure spectrum model for airfoil trailing-edge noise prediction. *International Journal of Aeroacoustics* **14** (5-6), 833–882.

Kitsios, Vassili, Sekimoto, Atsushi, Atkinson, Callum, Sillero, Juan A, Borrell, Guillem, Gungor, Ayse G, Jiménez, Javier & Soria, Julio 2017 Direct numerical simulation of a self-similar adverse pressure gradient turbulent boundary layer at the verge of separation. *Journal of Fluid Mechanics* **829**, 392–419.

Krogstad, P. A. & Skare, P. E. 1995 Influence of a strong adverse pressure gradient on the turbulent structure in a boundary layer. *Physics of Fluids* **7** (8), 2014–24.

Lee, Inwon & Sung, Hyung Jin 2002 Multiple-arrayed pressure measurement for investigation of the unsteady flow structure of a reattaching shear layer. *Journal of Fluid Mechanics* **463**, 377–402.

Lee, Seongkyu 2018 Empirical wall-pressure spectral modeling for zero and adverse pressure gradient flows. *AIAA Journal* pp. 1818–1829.

Maciel, Y., Tie, Wei, Gungor, A. G. & Simens, M. P. 2018 Outer scales and parameters of adverse-pressure-gradient turbulent boundary layers. *Journal of Fluid Mechanics* **844**, 5–35.

Meyers, Timothy, Forest, Jonathan B & Devenport, William J 2015 The wall-pressure spectrum of high-reynolds-number turbulent boundary-layer flows over rough surfaces. *Journal of Fluid Mechanics* **768**, 261–293.

Neves, João C. & Moin, Parviz 1994 Effects of convex transverse curvature on wall-bounded turbulence. part 2. the pressure fluctuations. *Journal of Fluid Mechanics* **272**, 383–406.

Olhede, S. C. & Walden, A. T. 2002 Generalized morse wavelets. *IEEE Transactions on Signal Processing* **50** (11), 2661–2670.

Panton, Ronald L. & Linebarger, John H. 1974 Wall pressure spectra calculations for equilibrium boundary layers. *Journal of Fluid Mechanics* **65** (2), 261–287.

Piquet, J. & Patel, V. C. 1999 Transverse curvature effects in turbulent boundary layer. *Progress in Aerospace Sciences* **35** (7), 661–672.

Rozenberg, Yannick, Robert, Gilles & Moreau, Stéphane 2012 Wall-pressure spectral model including the adverse pressure gradient effects. *AIAA Journal* **50** (10), 2168–2179.

Schatzman, D. M. & Thomas, F. O. 2017 An experimental investigation of an unsteady adverse pressure gradient turbulent boundary layer: embedded shear layer scaling. *Journal of Fluid Mechanics* **815**, 592–642.

Schewe, Günter 1983 On the structure and resolution of wall-pressure fluctuations associated with turbulent boundary-layer flow. *Journal of Fluid Mechanics* **134** (1), 311–328.

Schloemer, H. H. 1966 Effects of pressure gradients on turbulent boundary-layer wall-pressure fluctuations. Report.

Simpson, Roger L., Ghodbane, M. & McGrath, B. E. 1987 Surface pressure fluctuations in a separating turbulent boundary layer. *Journal of Fluid Mechanics* **177**, 167–186.

Skåre, Per Egil & Krogstad, Per-Åge 1994 A turbulent equilibrium boundary layer near separation. *Journal of Fluid Mechanics* **272**, 319–348.

Smol'yakov, A. V. 2006 A new model for the cross spectrum and wavenumber-frequency spectrum of turbulent pressure fluctuations in a boundary layer. *Acoustical Physics* **52** (3), 331–337.

Snarski, Stephen R. & Lueptow, Richard M. 1995 Wall pressure and coherent structures in a turbulent boundary layer on a cylinder in axial flow. *Journal of Fluid Mechanics* **286**, 137–171.

Willmarth, W. W., Winkel, R. E., Sharma, L. K. & Bogar, T. J. 1976 Axially symmetric turbulent boundary layers on cylinders: mean velocity profiles and wall pressure fluctuations. *Journal of Fluid Mechanics* **76** (1), 35–64.

Willmarth, W. W. & Yang, C. S. 1970 Wall-pressure fluctuations beneath turbulent boundary layers on a flat plate and a cylinder. *Journal of Fluid Mechanics* **41** (1), 47–80.

Yoon, Min, Hwang, Jinyul & Sung, Hyung Jin 2018 Contribution of large-scale motions to the skin friction in a moderate adverse pressure gradient turbulent boundary layer. *Journal of Fluid Mechanics* **848**, 288–311.

Zhou, Di, Wang, Kan & Wang, Meng 2020 *Large-Eddy Simulation of an Axisymmetric Boundary Layer on a Body of Revolution*. American Institute of Aeronautics and Astronautics.

Chapter 5

Space-time structure of an axisymmetric boundary layer ingested by a rotor

This chapter describes the measurements of the turbulence structure made with a tail-mounted rotor documenting the aerodynamic influence of the rotor on the upstream flow. The chapter is presented in the format of this dissertation and will be ultimately submitted to the Journal of Fluid Mechanics with the present author as the principal author, after further analysis.

Abstract

This study describes the spatio-temporally resolved measurements of turbulence in the vicinity of an unshrouded-rotor operating at the tail of an axisymmetric body. This is an idealized example of rotors operating at the hull or fuselage of a vehicle. While previous work [6] discuss the boundary layer structure along the tail without an embedded rotor, this study considers the impact of the rotor on the upstream flow as a function of thrust. Modifications in the mean flow, turbulence and correlation structure of the axial velocity, which drives the aeroacoustics of the rotor, are described for a set of advance ratios including zero-thrust, moderate-thrust and braking scenarios. The measurements were made in an axial-radial plane perpendicular to the rotor disc, with high-speed particle image velocimetry. At nominally zero thrust, the time-averaged flow and the turbulence structure appear to be minimally impacted by the rotor. At non-zero thrust, the mean flow and turbulence structure are distorted in a manner comparable with a variable axial pressure gradient. When thrusting, the effect of rotor is to impose a favorable pressure-gradient such that the mean flow is accelerated, the velocity profiles are fuller and the turbulence structure weakens as the boundary layer contracts. Conversely, for braking scenario the mean velocity defect increases, and the turbulence structure intensifies as the boundary layer expands. However, the fundamental mechanism of the strong adverse pressure gradient appears to be preserved as the mean velocity structure was invariant with the embedded shear layer scaling, where the primary effect of the rotor was to redistribute the turbulence across the individual components while not significantly affecting the net energy across the measured range of conditions.

5.1 Introduction

Rotors embedded in turbulent shear flows – common to a range of applications such as wind-turbines, marine-vehicles, pusher-type aircraft – are known to generate broadband and tonal noise - termed as turbulence ingestion noise. The aeroacoustics of such rotors has been studied for various configurations, from the early ones ingesting homogeneous and isotropic turbulence off of an upstream grid [51, 65, 68, 76, 77] to more recent ones ingesting zero-pressure gradient boundary layers [3, 25, 54, 55, 75] as well as wakes [4, 10, 30, 52, 53] with inhomogeneous and anisotropic turbulence. Consequently, several noise prediction methodologies and tools exist [4, 23, 25], covering both time-domain and frequency domain approaches. One important input to such methods is the correlation structure of the ingested flow which determines the acoustic character, including the tonal features generated as a result of correlated blade-to-blade loading, referred to as haystacks.

Since the correlation structure is a particularly complex function of spatial and temporal dimensions for inhomogeneous and anisotropic flows, the inputs are generally derived from subsets measured at upstream locations in the absence of the rotor. The distortion of the turbulence by the rotor, and other objects such as an adjacent wall, can significantly change the character of the turbulence and corrections are generally performed through the use of rapid distortion theory before estimating the far-field sound spectrum. Performing such corrections generally requires several simplifying assumptions which may not be applicable for practical configurations. Recent studies have tried to examine the ingested flow more directly, using blade-mounted instruments to determine the source-terms for rotors operating in idealized configurations such as flat-plate boundary layers and cylinder wakes [3, 30, 53].

The object of our research is to directly examine the distortion of the mean flow and turbulence structure of the inflow in a vehicle-relevant configuration. Specifically, we consider a rotor immersed in the boundary layer at the tail of a body-of-revolution and examine the aerodynamic influence of a rotor on the upstream flow. In an earlier study, Balantrapu et al. examined the evolution of flow along the tail without a rotor, documenting the impact of adverse-pressure gradient and lateral curvature on the mean flow, turbulence and correlation structure. In this study, the impact of a rotor on the tail flow is examined through measurements of the space-time structure in both thrusting and braking scenarios, with a goal of documenting the distortion of the flow. In addition to providing a physical insight into the rotor-flow interaction, the results are expected to serve in the validation of advanced turbulence distortion theories [24].

The paper is organized as follows. The apparatus and instrumentation is described in the following section (§ 5.2) with the results described in § 5.3. First, § 5.3.1 presents the comparisons of the zero-thrust measurements to those made without the rotor, which is followed by § 5.3.2 and § 5.3.3 that discuss the impact of thrust on the mean flow and turbulence respectively.

5.2 Apparatus and Instrumentation

All measurements presented here were made in the Virginia Tech Stability wind tunnel, in its anechoic configuration, which is detailed and documented by Devenport et al. [17]. The side-walls of this 1.83 m x 1.83 m wide and 7.6 m long test-section are formed by tensioned Kevlar that contain the flow while remaining transparent to the sound. The sound passing through the walls is further absorbed in the anechoic chambers that are lined by acoustic foam wedges. Similarly the wall and ceiling are made with perforated metal panels that are lined with Kevlar, and backed with 0.457 m foam wedges to futher minimize the tunnel reflections. The free-stream turbulence in the test-section is low, about 0.02% at 20 ms^{-1} and rising to about 0.035% at 50 ms^{-1}.

Figure 5.1 shows the experimental setup consisting of the body-of-revolution (BOR) and a five-bladed rotor mounted at the BOR-tail, that is driven by a downstream mounted drive-system via a hollow shaft. The body-of-revolution geometry, with a characteristic length of $D = 0.4318$ m, is comprised of a 2:1 forward nose, a cylindrical center-body (both 1D long) followed by a 20-degree tail cone that is about 1.1717D long. A 0.8 mm square trip ring installed between the nose and the mid-body is used to trip the flow. Additional details, including the construction and installation in the test-section via the cruciform tethers are described in detail by Balantrapu et al. [6].

The five-bladed rotor, shown in figure 5.2 has been designed in-house and has a diameter of D_r of 62.5 mm such that it is fully immersed in the boundary layer at the tail. The rotor geometry is adapted to the wake based on the velocity profile measured without the rotor, yielding a zero-thrust advance ratio, J = 1.44. Here $J = U_\infty/nD_r$ with U_∞ as the free-stream velocity, n is the number of rotor revolutions per second, and D_r is the rotor diameter. Further design details of the rotor, including the skew-distribution, the blade-section shape, and thickness distribution are described in a companion study by Hickling [30]. The rotor was CNC-machined and verified against the design via a laser-scan with a measurement uncertainty of 0.1 mm. It was observed that the fabricated geometry matched the design geometry within 0.1% of the rotor diameter, suggesting the rotor is axisymmetric.

The rotor was installed at the tail at $x/D = 3.1717$ (where x is along the BOR-axis with the origin at BOR nose), and driven by a 62.5 mm diameter hollow-shaft in order to facilitate the internal instrumentation required for BOR surface pressure measurements. The shaft was driven by a Kollmorgen servo motor through timing-belt with a sprocket reduction ratio of 2.83. Additional details of the hardware including the installation in the tunnel are described in [30].

The BOR-rotor system was positioned to a $0 \pm 0.25°$ angle-of-attack and verified with a ring of mean surface pressure taps on the nose at $x/D = 0.5$. Axial-symmetry in the tail boundary layer in the absence of rotor were documented with a combination Pitot-probe rake and single hotwire anemometry ad was found to be axisymmetric to within 2% in the mean velocity and 7% in the turbulence intensity [6]. The flow structure on the tail without the

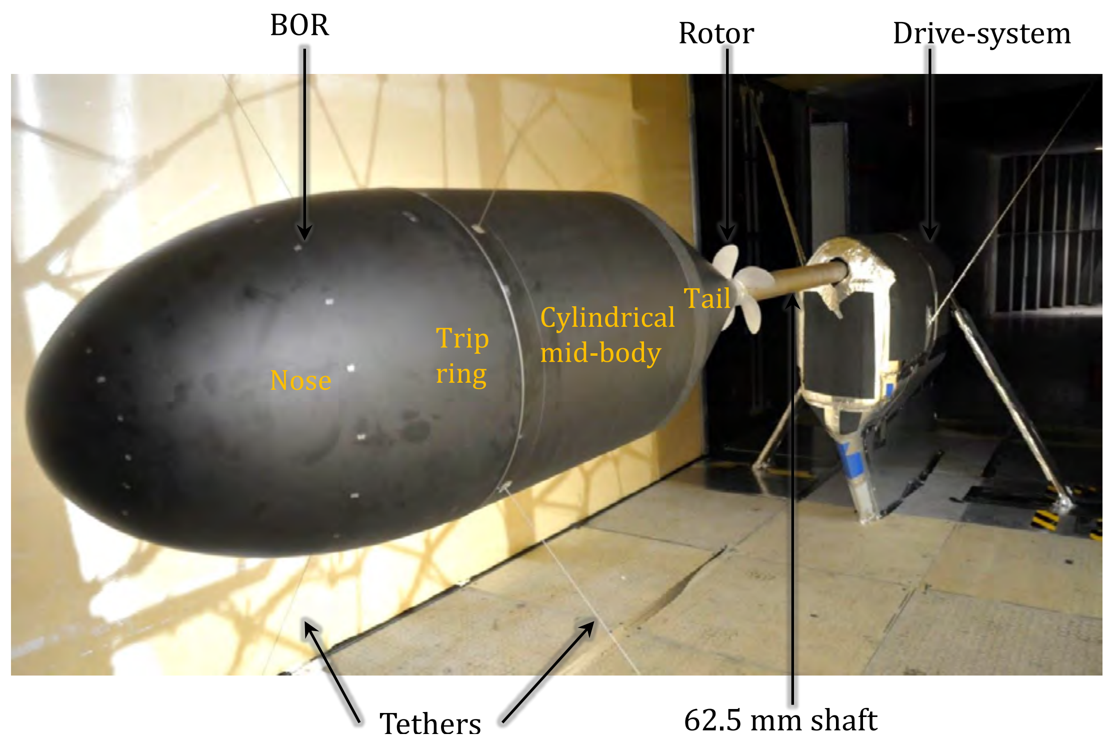

Figure 5.1: Photograph of the test-section, showing the experimental arrangement comprised of a BOR, a rotor mounted at the BOR tail that is driven by the downstream drive-system via a hollow shaft.

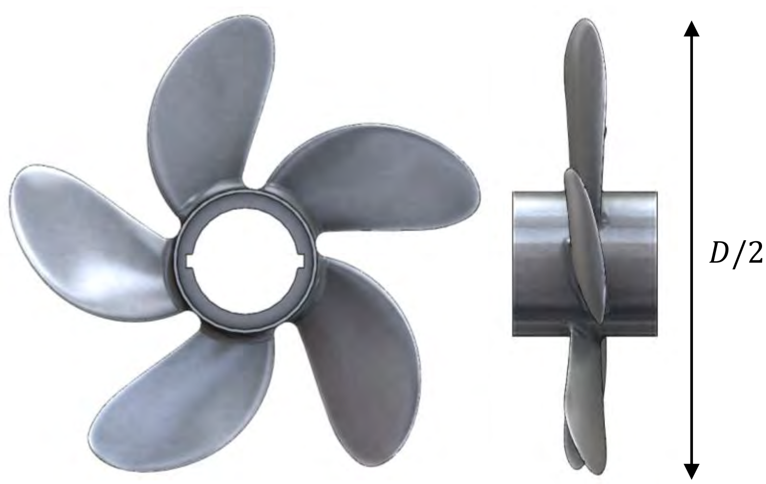

Figure 5.2: Rendering of the geometry of the five-bladed rotor immersed in the tail boundary layer, showing the front-view and the side-view. The diameter of the rotor is 216 mm which corresponds to half the diameter of the BOR.

J	Rotor speed (RPM)	Re_D	U_∞ (ms^{-1})
1.44	4020	6.00×10^5	20.83
1.10	5250	5.99×10^5	20.78
2.64	2240	6.04×10^5	21.28

Table 5.1: Test matrix for the time-resolved inflow measurements

rotor were documented extensively, using a combination of hotwire anemometry and particle Image velocimetry (PIV). Using a single hotwire, fifteen profiles were obtained documenting statistics and temporal structure of the streamwise velocity, detailed in §2.4 in Balantrapu et al. [6]. Measurements of the turbulence structure in the vicinity of the rotor are presented in the following section.

5.2.1 Time-resolved measurements of the inflow to the rotor

Figure 5.3 shows the experimental arrangement for the turbulent inflow to the rotor. Measurements were made in the axial-radial plane oriented vertically at $\theta = \pi/2$ covering the tail boundary layer between $x/D = 2.95$ to 3.2 as shown in the insert at the top right, with the test matrix shown in table 5.1. Two Phantom v2512 high-speed cameras positioned below the test-section floor were focused on to the measurement plane through flat acrylic windows. The cameras were calibrated to the measurement plane with the acrylic window installed in order to account for the distortion due to the acrylic. A 200-mm Nikon lens (type AF-S NIKKOR f/2G VR II) was installed with a Scheimpflug mount, ensuring uniform focus across the measurement plane. A high-speed Photonic Industries DM series, Nd-YAG 532-nm laser was used to illuminate the seed (Di-Ethyl-Hexyl-Sebacat oil) with the beam delivered via a LaVision guiding arm. A LaVision Programmable Timing Unit PTU-X synchronized the operation of laser and cameras, sampling in double-frame mode at 12.848-kHz, acquiring over 24000-images per each acquisition, lasting over two-seconds. Two such runs were acquired increasing the total sampling time to over four-seconds, which is greater 1000 turnover time-scales. Furthermore, the sampling was phase-locked to the rotor to facilitate unsteady background removal during post-processing.

All data was post-processed in Davis 10.0 over multiple passes, beginning with an interrogation window size of 64×64 px^2 (8-mm resolution) followed by a 32×32 px^2 window with 75% overlap, resulting in a 4-mm spatial resolution but a 1-mm vector resolution. The resulting vectors were imported to MATLAB and further post-processed by truncating the physically unrealistic contributions with a threshold based on the histograms of the fluctuating velocity.

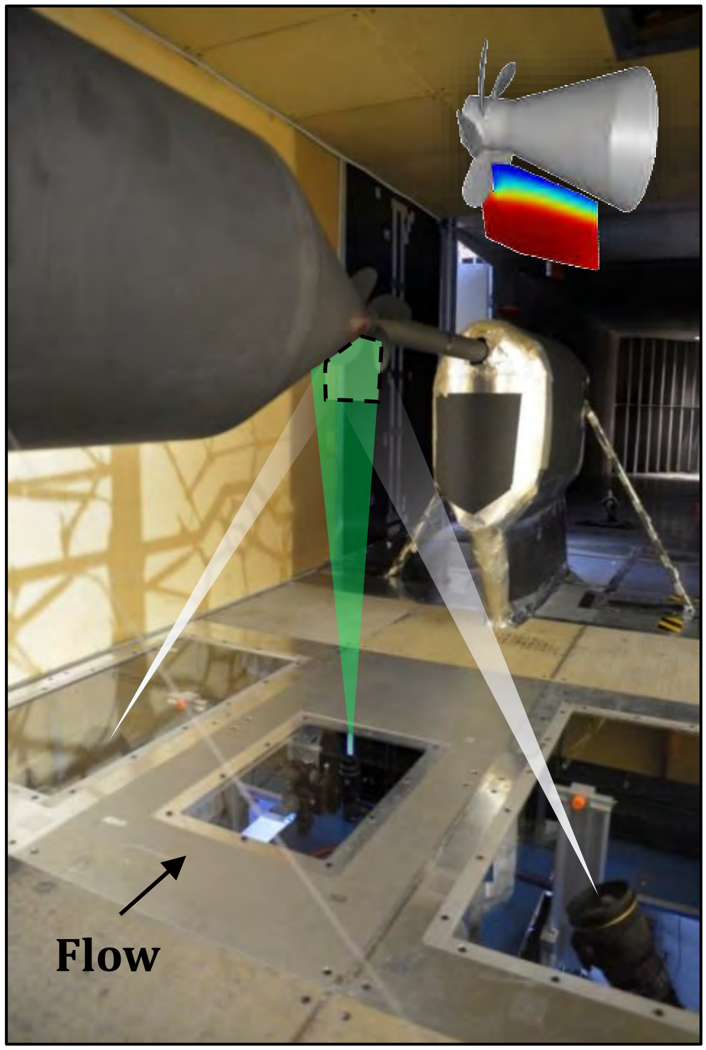

Figure 5.3: Photograph showing the experimental arrangement for the time-resolved particle image velocimetry measurements. The cameras and laser installed outside the floor were focused onto the axial-radial plane (shown in the insert at top-right) just upstream of the rotor.

5.3 Results and Discussion

Results presented below are discussed in a co-ordinate system centered at the BOR nose. The x-axis aligned with the BOR axis, such that the nose extends from x/D of 0 to 1, with the cylindrical mid-body extending from x/D of 1 to 2, followed by the tail from x/D of 2 to 3.1717. With the vertical axis as y and the horizontal as z, the rotor at the BOR extends upto a radius r/D of 0.25.

5.3.1 Inflow at nominally zero thrust

Figure 5.4(a) shows the contours of mean velocity along the axial direction U_x normalized on the tunnel reference velocity (U_∞), for J = 1.44 which corresponds to zero thrust. The results shown here are for the time-averaged mean velocity, obtained by averaging all the samples from a single run (of two) irrespective of the rotor phase. The contours show the velocity increasing on moving away from the BOR surface and eventually approaching the tunnel free-stream, with the boundary layer edge identified by the solid black line. The results for J = 1.44 are generally consistent with the mean velocity estimates from previous measurements made without the rotor (using a combination of quadwire anemometer and PIV), as seen from a profile at the tail shown in figure 5.4(b). Here, all three components of the velocity, axial (U_x), radial (U_r) and circumferential (U_θ), are in agreement with the no-rotor case, suggesting that the rotor is operating approximately, if not exactly, at zero thrust.

Figure 5.5(a) shows the profiles of turbulent stress associated with the tail exit (x/D=3.1717). The turbulent stresses, obtained with respect to the time-averaged mean velocity, are compared against the no-rotor case. While the general form of the stresses, particularly u_x^2, is in agreement with those without the rotor, the magnitudes seem to be slightly underestimated, by about 15%. While this could suggest that the rotor is not exactly at zero-thrust, it is very likely that the underestimation is a result of lower spatial resolution for this TR-PIV measurements. The spatial resolution in this case was 4-mm, almost twice relative to the no-rotor PIV which had a 2-mm resolution. Investigations by varying the interrogation window size of the no-rotor PIV measurements revealed confirmed this scenario, as the 4-mm resolution results were significantly closer to the current TR-PIV estimates. This can also be directly observed in the comparisons of the auto-spectral density estimates shown in figure 5.5(b). Here, the axial velocity spectra ($G_{u_x u_x}(f)$) from three representative locations at the tail, are compared with results at similar locations from quadwire measurements (without the rotor, dotted line) with a 1 mm resolution. The form and levels of the spectra at low frequencies ($f < 500$Hz) are consistent with the no-rotor results; At higher frequencies, the TR-PIV estimates are underestimated by over 2.5-dB (particularly for $|y/D| = 0.188$) which would be consistent with a spatial-filtering due to inadequate resolution. The spectra also differ on two more aspects, i) the sharp peak at $f \sim 400$ Hz which corresponds to the blade

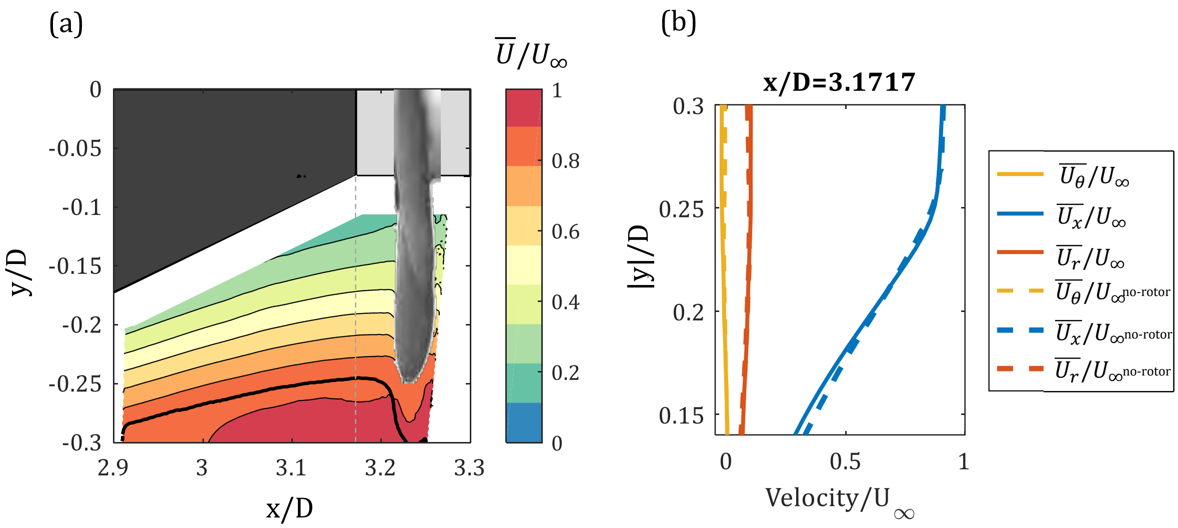

Figure 5.4: (a) Contours of the time-averaged axial mean velocity (normalized on the tunnel free-stream velocity) for the zero-thrust configuration with J = 1.44; Thick black line represents the edge of the boundary layer. (b) Profiles of the mean velocity in the axial, radial and circumferential directions from the tail exit (shown by the vertical grey line in (a) compared with previous measurements from no-rotor configuration

passage frequency, ii) a higher noise floor specially above 3000 Hz.

The above presented results are consistent for all locations in the tail-boundary layer as seen from the contours of the auto-spectral density in figure 5.6(a-b). Here, the vertical axis represents the location in the boundary layer relative to the surface ($|y - y_s|$ with $y_s = 0.0735D$), normalized with the boundary layer thickness ($\delta = 75mm$). The horizontal axis represents the frequency f normalized on the reference scale derived from the edge-velocity and BOR diameter $f' = fD/U_e$. The contour levels represent the pre-multiplied power-spectra $fG_{u_x u_x}$ such that equal areas represent equal contributions to the total energy. While no-rotor results are shown in figure 5.6(a), the results at zero-thrust are shown in figure 5.6(b); The geometric organization is roughly similar, except the vertical band that corresponds to the blade-passing frequency, and lower levels at higher frequencies ($fD/U_e > 10$). Therefore, the results are suitable to explore the large-scale turbulence structure, at low frequencies, which are particularly relevant to the far-field acoustic signature of the rotor.

In the following section, the effects of thrust are considered, with a moderately thrusting advance ratio of J = 1.1 and a strongly braking advance ratio of J = 2.64. First, the effects on the mean flow and turbulence statistics are considered, with a focus on the boundary layer profile at the tail. This is followed by a discussion on the distortion of the turbulence by the rotor as seen from the time-delay correlations for various advance ratios.

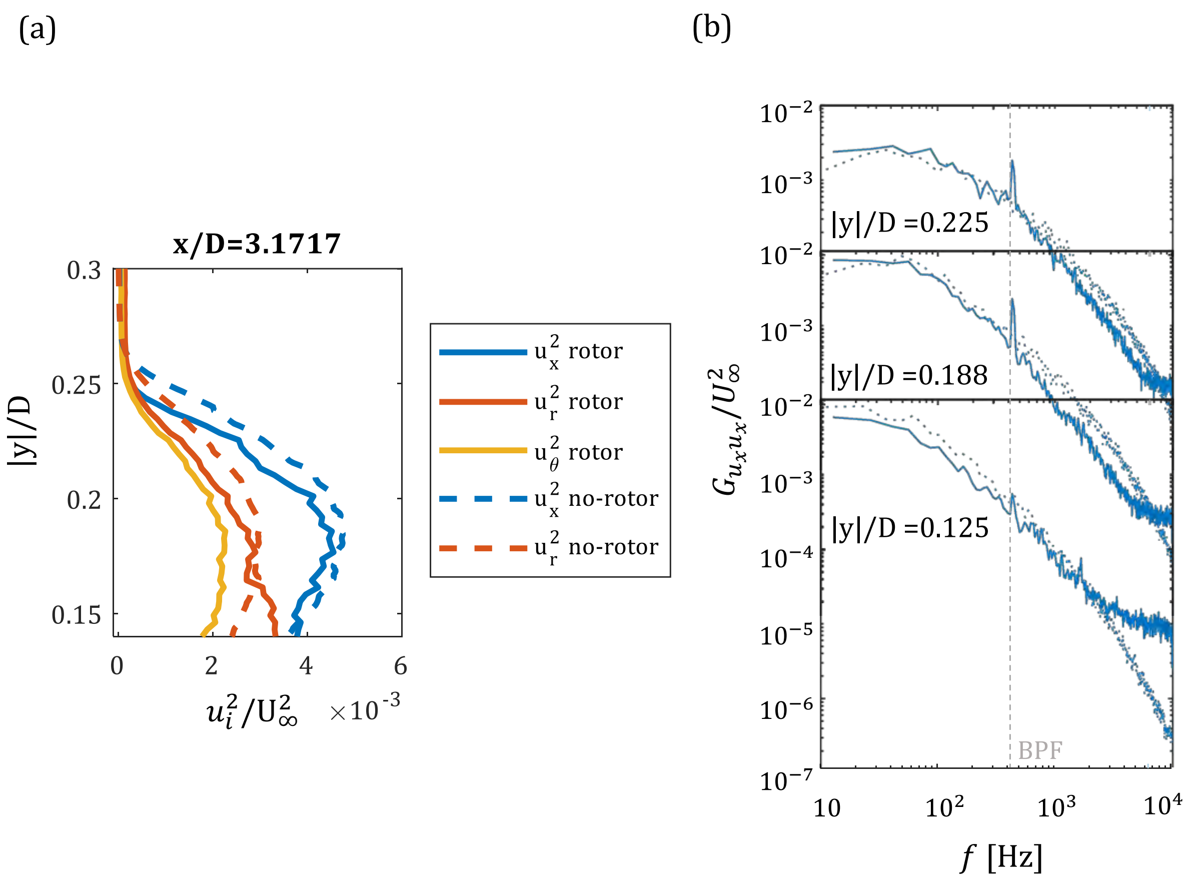

Figure 5.5: Turbulence profiles at the BOR tail for J = 1.44. (a) Turbulence stresses based on the time-averaged mean velocity, compared with results from the no-rotor measurements. (b) Auto-spectrum of the axial unsteady velocity, shown at three representative locations in the boundary layer at the BOR tail, and compared against the no-rotor results. Sold lines represent the zero-thrust results while dotted lines represent the no-rotor estimates.

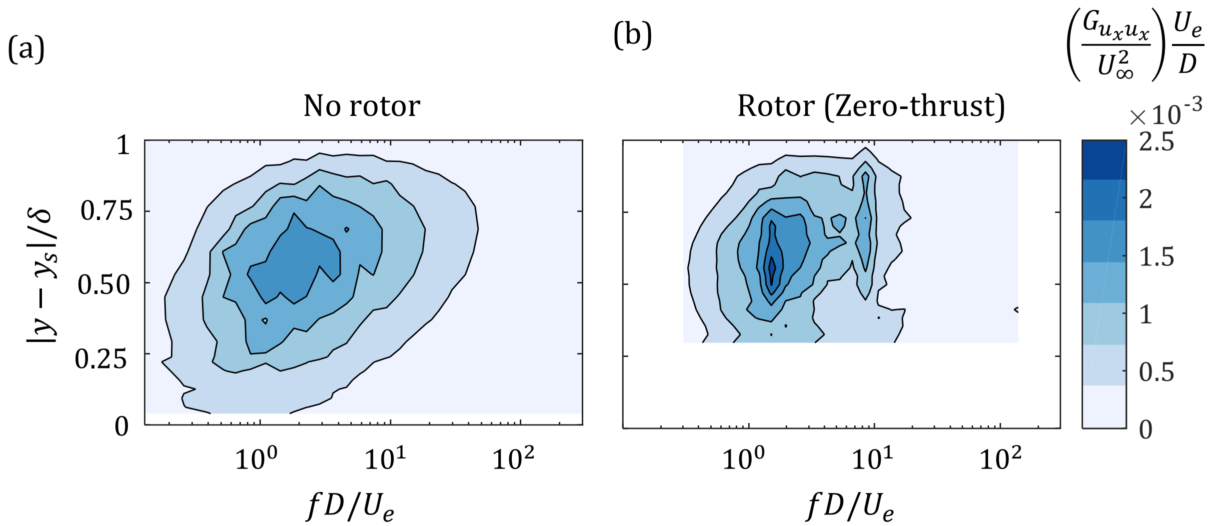

Figure 5.6: Contours of the premultiplied spectra of the axial velocity compared for (a) no-rotor case and (b) with the rotor at zero-thrust

5.3.2 Effect of thrust on the mean flow

Figure 5.7(a) shows the contours of the time-averaged axial velocity for the thrusting case (J = 1.10) normalized with the zero-thrust results (from figure 5.4(a)). As expected from a streamtube contraction, the rotor accelerates the inflow, shrinking the boundary layer (edge shown in blue) relative to the zero-thrust case. The effect of acceleration is higher closer to the BOR surface, with about 40% increase at the tail, and is consistent with the wall boundary condition. At negative thrust,figure 5.7(b), the results are exactly opposite, with the rotor decelerating the mean flow as the boundary layer expands (red line) relative to the zero-thrust case.

Figure 5.8(a) compares the profiles for the various components of the velocity at the BOR tail, with the vertical axis representing the distance from the BOR-axis normalized on the BOR diameter $D = 0.4318m$. Here, the profiles in black show the zero-thrust results reproduced from figure 5.4(b) while blue and red correspond to the thrusting and braking conditions respectively. While the trends in axial velocity profile are consistent with the above observations, the radial velocity is also impacted, in a fashion where the mean flow appears to drift radially towards the rotor blade tips for a thrusting rotor, while drifting inwards for a braking rotor. Furthermore, the Reynolds normal stress profiles (of axial velocity) are also sensitive to the rotor thrust, figure 5.8(b), with the peak levels decreasing and moving inwards as the rotor thrusts, and conversely moving outward as the flow is decelerated by a braking rotor. These effects cannot simply be explained by the fact that the boundary layer is constricted (or expanded) by the rotor; Since these trends persist when the profiles are recast in terms of the boundary layer parameters (from table 5.2) as shown in figure 5.9(a-b). Here, the vertical axis represents the distance from the surface normalized with the boundary

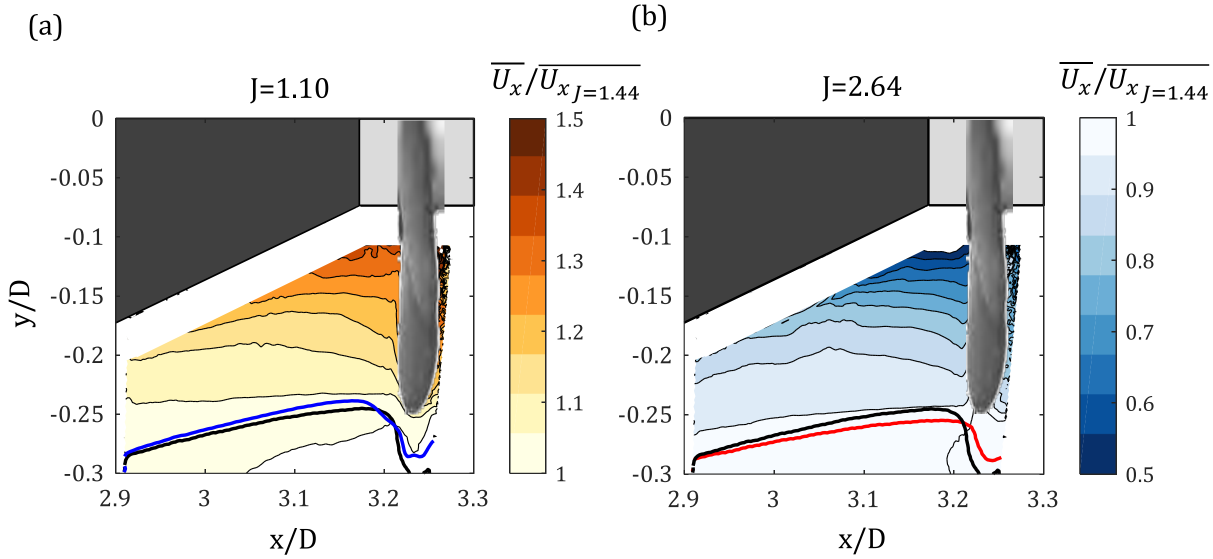

Figure 5.7: Contours of the mean axial velocity revealing the effect of thrust on the inflow. The axial velocity is normalized with the corresponding values from J = 1.44 to demonstrate the change relative to zero-thrust. (a) shows the result for J = 1.10 or the moderate thrust case and (b) shows the result for J = 2.64, the braking condition (negative thrust)

layer thickness, while the horizontal axis represents velocity and Reynolds stress normalized with the edge velocity. The effect on the boundary layer profiles appear equivalent with the effect of a varying axial-pressure gradient; For the thrusting rotor, the observations are consistent with a favorable pressure gradient, with fuller mean velocity profiles and reduced normal stress for the axial velocity. Similarly, for the braking rotor, the velocity profile sees a higher deficit, and a correspondingly a broader peak in the turbulent stresses. This change in the axial turbulence is expected to affect the acoustic signature of the rotor since it is a dominant contributor to the unsteady upswash [30]. However, from a fundamental perspective, if one examines the turbulent kinetic energy profiles ($\frac{1}{2}(u_x^2 + u_r^2 + u_\theta^2)$), figure 5.9(c), it appears that the primary effect of the rotor is to redistribute the turbulent energy into the cross-stream components, such that the net turbulence energy is nearly constant across the advance ratios considered here. Furthermore, the fundamental mechanisms of the boundary layer appear to remain intact, as the mean velocity profiles were found to carry inflection points in the outer regions, with the functional form conforming to the no-rotor results when recast with the embedded shear layer scaling Balantrapu et al. [6] as shown in figure 5.10.

J	Rotor speed (RPM)	Re_D	U_∞ (ms^{-1})	U_e/U_∞	δ (mm)
1.44	4020	6.00×10^5	20.83	0.8594	74.8
1.10	5250	5.99×10^5	20.78	0.8764	71.2
2.64	2240	6.04×10^5	21.28	0.8548	78.2

Table 5.2: Operating conditions and flow parameters for various advance ratios

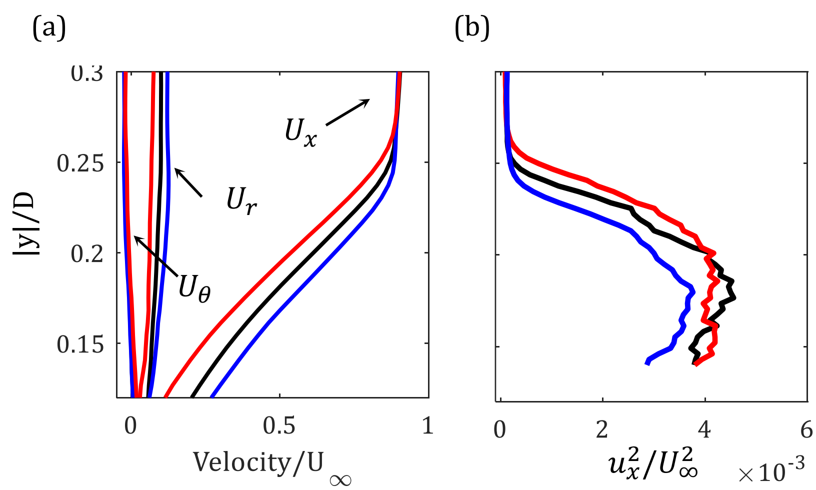

Figure 5.8: Results from the radial profile at the BOR tail ($x/D = 3.1717$) evaluating the effect of thrust. Time averaged mean velocities are shown in (a) and Reynolds stress of the axial velocity are shown in (b). Black represents the zero-thrust results, J = 1.44 (from figure 5.4(b)), blue represents the results for J = 1.10 and red represents the results for J = 2.64.

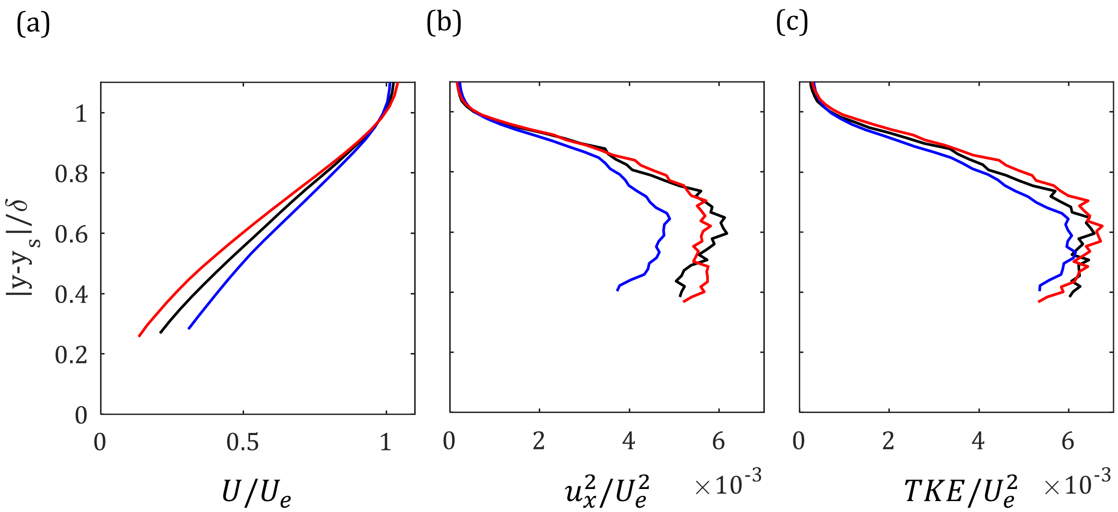

Figure 5.9: Mean velocity and turbulence profiles at the BOR tail ($x/D = 3.1717$) from figure 5.8 normalized on the boundary layer parameters. Vertical axis represents the distance from the surface ($|y - y_s|$) normalized with the boundary layer thickness (δ) while horizontal axis represents the mean velocity magnitude U (a), Reynolds normal stress of the axial velocity (b), and the turbulence kinetic energy ($TKE = 0.5(u_x^2 + u_r^2 + u_\theta^2)$) (c), all normalized with the edge velocity U_e. Color legend shown in figure 5.8

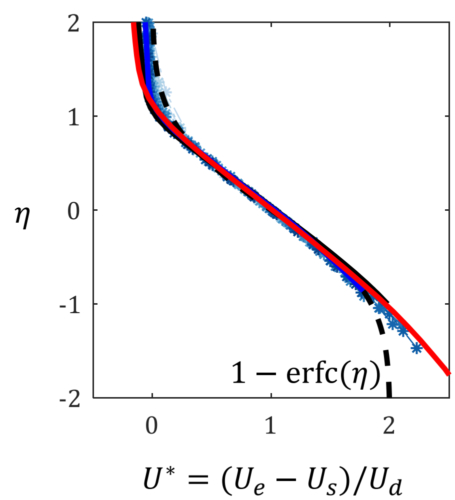

Figure 5.10: Mean velocity profile at the BOR tail with embedded shear layer scaling for the thrusting conditions, shown with the results from various streamwise stations on the tail measured without the rotor (from Balantrapu et al. [6]).

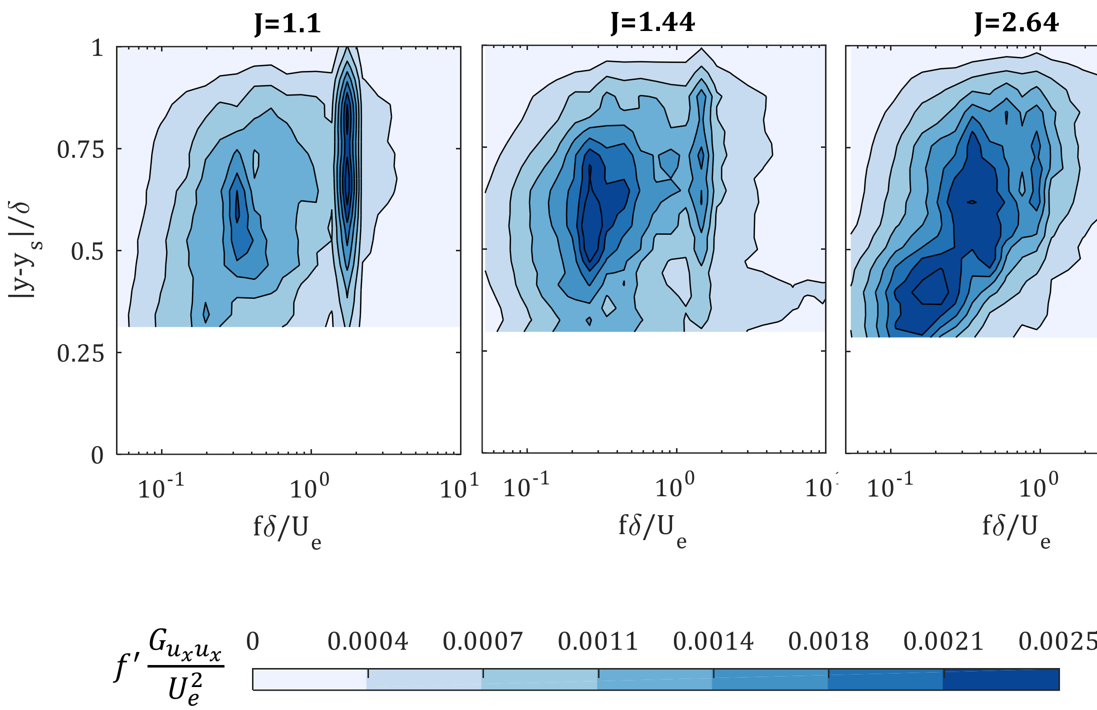

Figure 5.11: Contours of the pre-multiplied spectra of the axial velocity with the boundary layer scaling, revealing the impact of the rotor on the turbulence structure. (a) J = 1.10, (b) 1.44 and (c) J = 2.64

5.3.3 Effect of thrust on the turbulence

Figure 5.11 shows the effect of the rotor on the turbulence structure of the axial velocity. Here, contours of the pre-multiplied spectra of the axial velocity $f'G_{u_x u_x}/U_e^2$ are shown, with the vertical axis representing the location in the boundary layer, and horizontal axis representing the frequency f normalized on the boundary layer time-scale $f' = f\delta/U_e$. While figure 5.11 (a) shows the results for the thrusting rotor, (b) and (c) show the turbulence structure for the zero thrust and braking rotor respectively. Consistent with the observations in the turbulence profiles shown earlier, the turbulence is energized as the rotor shifts from a thrusting to braking scenario. Particularly, for the braking scenario there seems to be a significant increase in the energy in the lower-half of the boundary layer, with a secondary peak centered around $f' \sim 0.2$ distinct from the outer peak centered at $f' \sim 0.4$. Note that the vertical bands at the higher frequencies correspond to the blade-passing frequency and are expected to vanish when the spectra are estimated for the velocity fluctuating about the phase-averaged mean velocity.

In order to examine the influence of the rotor on the turbulence time-scales, the above information is recast in the physical space as shown in figure 5.12(a-d). Here, the contours levels represent the time-delay correlation coefficient,

$$\rho_{u_x u_x}(x', y'; \tau) = \frac{< u_x(x', y', t) u_x(x', y', t + \tau) >}{\sqrt{< u_x(x', y', t) u_x(x', y', t) >}} \tag{5.1}$$

with figure 5.12(a) corresponding to the results without the rotor, and figure 5.12(b,c,d) corresponding to the zero-thrust (J = 1.44), positive-thrust (J = 1.44) and negative thrust (J = 2.64) respectively. Generally speaking, for all conditions, the correlations last longer closer to the wall, consistent with an expected rise in the turbulence length-scales [6]. Furthermore, in the presence of a rotor, figure 5.12 (b,c,d), the correlations appear to carry a periodic component across the boundary layer which is particularly prominent for $|y - y_s|/\delta \sim 1$, which corresponds to the location of the blade tip (see figure 5.4(a)). This is due to the fact that the results are based on the time-averaged velocity and are expected to disappear if one considers the correlations of the velocity fluctuating relative to the blade-phase averaged velocity. However, the rotor appears to influence the turbulence time-scales even for the zero-thrust case and needs further investigation. For a thrusting rotor, the time-delay correlations are compressed across the boundary layer while they are significantly longer for braking conditions. This is expected to alter the characteristics of haystack peaks in the far-field rotor noise spectrum, as it directly influences the blade-to-blade correlated loading.

Further investigations are required to reveal the physical mechanisms that account for this behavior and also understand the complete effects of the rotor. For example, the above analysis must be confirmed with those of the phase-mean subtracted velocities. Furthermore, these results can be more quantitatively associated with measurements of the corresponding far-field acoustic signature of the rotor which were discussed by Hickling [30]. Additionally, one could examine the complete space-time correlations of the various velocity components that can then be used to validate the turbulence distortion models, existing ones as wells as the ones under development [24].

5.4 Conclusions

This study considers the distortion of the inflow to a rotor operating at the tail of an axisymmetric body, that is fully immersed in the boundary layer. Spatio-temporally resolved measurements of the tail boundary layer were made upto one rotor-diameter upstream of the rotor, for advance ratios that include zero, positive and negative thrusting scenarios. The results, including the mean flow, turbulence stresses and spectra are expected to serve towards the development and validation of advanced turbulence distortion models, as required for more accurate predictions of the rotor acoustics.

Preliminary analysis of the results considering a radial profile just upstream of the rotor confirmed that both the mean and fluctuating velocity fields are sensitive to the considered set of rotor operating conditions. While the results for a rotor producing a nominally zero

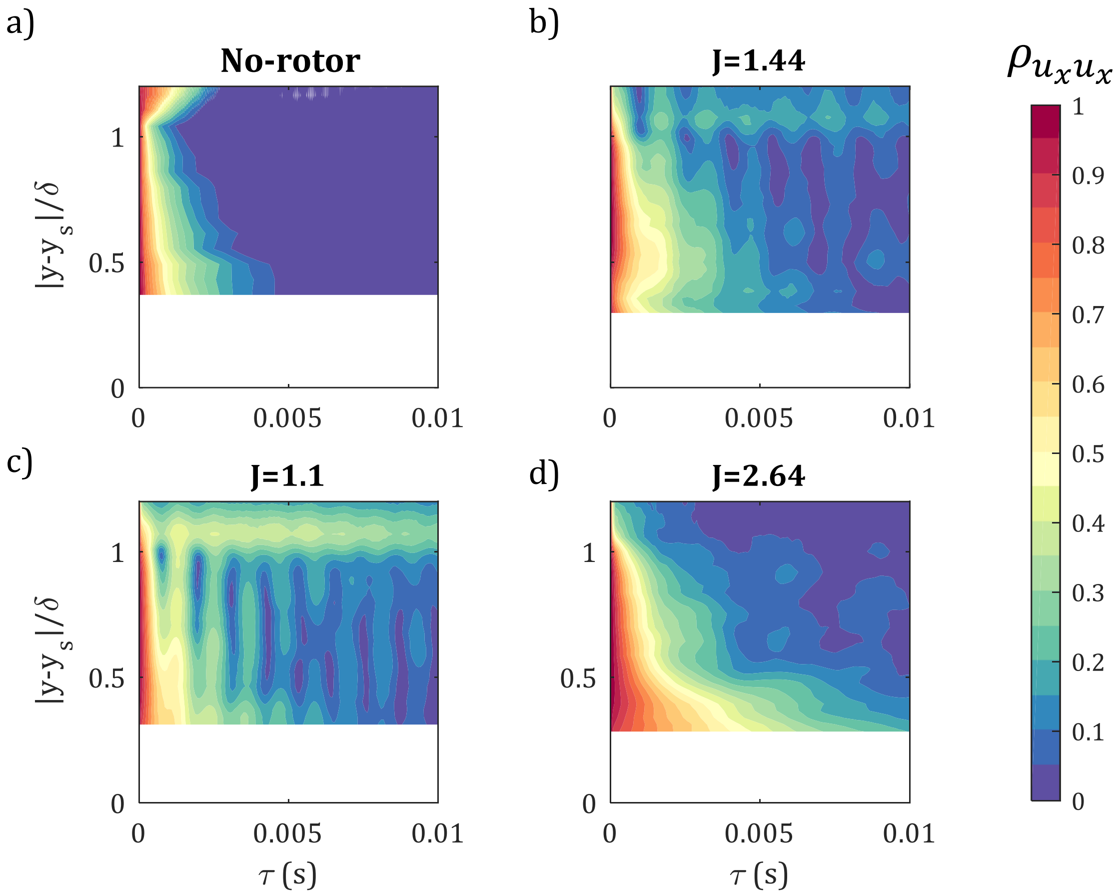

Figure 5.12: Contours of the auto-correlation coefficient of the axial velocity $\rho_{u_x u_x}$, as a function of time-delay τ, showing the effect of the rotor on the turbulence length scales. Note that the results correspond to zero separation in the boundary layer. (a) Results from no-rotor (b) J = 1.44 (c) J = 1.10 (d) J = 2.64

thrust are nearly consistent with previous measurements of the tail boundary layer made without the rotor, the effect of the thrust on the rotor is to alter the axial turbulence in a fashion that can be explained by a varying mean pressure gradient. For positive thrust, the boundary layer contracts, with fuller mean velocity profiles, and weaker Reynolds stress profiles of the axial velocity. The converse is true for a braking rotor: the mean velocity defect strengthens and the turbulence peak of the axial amplifies as the boundary layer expands. Such variations in the axial turbulence, which are dominant contributors to the unsteady blade loading, are expected to vary the the rotor acoustics. However, the fundamental turbulence mechanisms appear to be consistent with the undisturbed boundary layer: while the functional form of the mean velocity profiles is still governed by the embedded shear layer scaling, and the turbulent kinetic energy changes very weakly across the considered thrust cases with the energy appearing to be only redistributed between the axial and cross-stream components.

Acknowledgements

This study was sponsored by the Office of Naval Research, particularly Dr. Ki-Han Kim and Dr. John Muench, through grants N00014-17-1-2698 and N00014-20-1-2650. The authors are grateful to Drs. William Blake, Jason Anderson, Meng Wang, Stewart Glegg, Todd Lowe and Mr. Michael Marcolini for many helpful discussions and advice. The authors would also like to thank the staff of Virginia Tech Stability Wind Tunnel, AOE Machine Shop, and all the graduate research assistants for their deep involvement during the hardware design and measurement campaign.

Declaration of interests

The authors report no conflict of interest.

Chapter 6

Conclusions and Outlook

This dissertation describes the measurements of an axisymmetric boundary layer under a strong adverse pressure gradient, and is relevant to practical applications such as marine vehicles and pusher-type aircraft. The mean flow, turbulence, and correlation structure over the tail of a body-of-revolution, measured with a combination of hotwire anemometry and particle image velocimetry, are examined in addition to the measurements of the mean and fluctuating surface pressure. Subsequently, the impact of a rotor at the tail on the upstream boundary layer, measured with high-speed particle image velocimetry, is examined for a set of advance ratios in order to supply information towards development of more accurate turbulence models for aeroacoustic predictions. The key conclusions are presented below in addition to suggestions for further analysis towards the development of a broad framework for turbulence modelling in practical configurations.

The non-equilibrium flow in the outer region along the tail of body-of-revolution was found to have some properties of a free-shear layer and was self-similar with a recently proposed embedded shear layer scaling. Based on the location of the inflection points in the mean velocity profile, the velocity defect served as the velocity scale and the associated vorticity thickness served as the length scale. While the functional form of the profile in the outer regions was described by the complementary error function (used in mixing layers) the collapse in the streamwise turbulence intensity was less perfect with the a peak value of approximately $0.021U_d$.

The vorticity thickness was found to grow linearly at a rate consistent with previous studies in free-shear flows. Additionally the velocity and length scales were proportional to the edge velocity and boundary layer thickness respectively - consistent with the requirement of self-similarity. However, the argument of whether such embedded shear layer motions is triggered by the inviscid instability arising from inflectional velocity profiles is outstanding. While it is believed that the existence of inflection points and embedded shear layer is correlated but not causal, further investigations must be performed to examine this cause and effect relationship for strong adverse pressure gradient flows. Subsequently, the boundary conditions that trigger the formation of an embedded shear layer must be examined through parametric investigations in order to identify the range of conditions where embedded shear layer scaling is valid.

The turbulence structure of the streamwise velocity is consistent with the observations made in the mean flow. While the large-scale motions in the outer region amplify and grow with the boundary layer thickness, the low-frequency regions of the pre-multiplied power spectrum are roughly self-similar with the embedded shear layer scaling, emphasizing the role of the embedded shear layer on the turbulence structure.

Analysis of the correlation structure revealed that the non-linear interactions could be significant in the lower half of the boundary layer given the high turbulence levels. By comparing the two-point correlations (from PIV) with single point estimated (from hotwire) it was observed that the turbulence convection velocity was about about one and a half times the local mean speed, suggesting that the turbulence may be convecting itself. It is therefore important to consider such corrections when extrapolating single-point estimates into a full correlation structure through Taylor's hypothesis.

The associated wall pressure fluctuations were studied with a longitudinal array of microphones on the rear-half of the tail. As the flow decelerated downstream, the root-mean-square levels dropped downstream along with the wall-shear stress, roughly as $7\tau_w$. While the associated auto-spectra saw a broadband reduction of over 15-dB per Hz, they attained a single functional form (within 2-dB) with the wall-wake scaling where the wall-shear stress was the pressure scale and a scale derived from the boundary layer thickness and edge velocity was the time-scale. The general success of this scaling, extending to even the viscous roll-off regions suggests the dominant role played by the outer layer motions in the wall pressure.

Further investigations of the space-time structure revealed the presence of a quasi-periodic feature that appeared to convect at speeds matching those at the inflection points, suggesting that corresponding pressure-producing motions are centered in the outer regions. Furthermore, the conditional structure obtained from wavelet analysis was found to scale with the wall-wake scaling, supporting the observations made in the wall-pressure spectrum. This lead to the hypothesis that the outer region motions play a more indirect role, by modulating the near-wall turbulence and consequently the wall pressure and shear-stress. While the modulation of the near-wall turbulence has been observed before, the impact on the wall-pressure fluctuation and wall shear-stress needs to be examined. To investigate the wall pressure one can evaluate the source terms of the pressure-Poisson equation by including both the pressure-gradient terms of the mean-shear component as well as the non-linear terms. To evaluate the impact on wall shear-stress, one can consider the recent work of Renard and Deck (Renard, N., & Deck, S. (2016). A theoretical decomposition of mean skin friction generation into physical phenomena across the boundary layer. Journal of Fluid Mechanics, 790, 339-367.).

Subsequent measurements of the space-time structure of the tail boundary layer in the vicinity of a rotor were examined to study the impact of the rotor as function of thrust. The flow structure for the zero-thrust configuration is found to be closely consistent with the undisturbed flow in the absence of rotor. At thrusting and braking operations, the distortion of the mean flow is consistent with the slip-stream contraction. For a thrusting rotor, the mean velocity profiles are fuller and the axial turbulence is weaker, while the opposite is true for a braking rotor. However, the fundamental turbulence mechanisms appear to be consistent across the set of conditions considered; The modified mean velocity and turbulence profiles appeared to attain a functional form similar to that of the no rotor case, when scaled with the embedded shear layer parameters that are based on the properties at the outer inflection points in the mean velocity. The primary effect of the rotor appears to alter the distribution of the turbulent kinetic energy between the individual components while minimally affecting the net energy. The structure of the axial turbulence was investigated as they are important from the aeroacoustic perspective; The turbulence structure seemed sensitive to the presence of the rotor and was altered even for the zero-thrust case. Furthermore, at non-zero thrust the impact was roughly equivalent to the effect of a pressure gradient: at thrusting, the pressure gradient is lowered and the turbulence structure weakens and moves closer to the wall. The opposite is true for braking condition. Analysis of the time-delay correlation structure revealed that the axial turbulence scales are affected by the rotor both at zero-thrust and thrusting conditions, such the correlations were shortened by a thrusting rotor while elongated by a braking rotor. This is expected to impact the correlated blade-to-blade loading and hence the characteristics of the acoustic signature, particularly of the tonal haystacks.

Bibliography

[1] Ronald J. Adrian. Hairpin vortex organization in wall turbulence. 19(4):041301, 2007. doi: 10.1063/1.2717527. URL https://aip.scitation.org/doi/abs/10.1063/1.2717527.

[2] Ronald J Adrian, Carl D Meinhart, and Christopher D Tomkins. Vortex organization in the outer region of the turbulent boundary layer. *Journal of fluid Mechanics*, 422: 1–54, 2000.

[3] W. Nathan Alexander, William J. Devenport, and Stewart A. L. Glegg. Noise from a rotor ingesting a thick boundary layer and relation to measurements of ingested turbulence. *Journal of Sound and Vibration*, 409:227–240, 2017. ISSN 0022-460X. doi: https://doi.org/10.1016/j.jsv.2017.07.056. URL http://www.sciencedirect.com/science/article/pii/S0022460X17305898.

[4] Jason M. Anderson, M. Ryan Catlett, and Devin O. Stewart. Modeling rotor unsteady forces and sound due to homogeneous turbulence ingestion. *AIAA Journal*, 53(1):81–92, 2015. ISSN 0001-1452 1533-385X. doi: 10.2514/1.j052874.

[5] C. D. Aubertine and J. K. Eaton. Turbulence development in a non-equilibrium turbulent boundary layer with mild adverse pressure gradient. *Journal of Fluid Mechanics*, 532:345–364, 2005. ISSN 0022-1120. doi: 10.1017/S0022112005004143.

[6] N. Agastya Balantrapu, C. Hickling, William N. Alexander, and William J. Devenport. The structure of a highly-decelerated axi-symmetric turbulent boundary layer. *Journal of Fluid Mechanics*, ((under review)), 2021.

[7] William K Blake. *Mechanics of flow-induced sound and vibration, Volume 2: Complex flow-structure interactions*. Academic press, 2017. ISBN 0128122900.

[8] L. Castillo and Wang Xia. Similarity analysis for nonequilibrium turbulent boundary layers. *Transactions of the ASME. Journal of Fluids Engineering*, 126(5):827–34, 2004. ISSN 0098-2202. doi: 10.1115/1.1789527. URL http://dx.doi.org/10.1115/1.1789527.

[9] Luciano Castillo and William K. George. Similarity analysis for turbulent boundary layer with pressure gradient: Outer flow. *AIAA Journal*, 39(1):41–47, 2001. ISSN 0001-1452. doi: 10.2514/2.1300. URL https://doi.org/10.2514/2.1300.

[10] Matthew Catlett, Jason Anderson, and Devin Stewart. Aeroacoustic response of propellers to sheared turbulent inflow. In *18th AIAA/CEAS Aeroacoustics Conference (33rd AIAA Aeroacoustics Conference)*, page 2137, 2012.

[11] D. M. Chase. Modeling the wavevector-frequency spectrum of turbulent boundary layer wall pressure. *Journal of Sound and Vibration*, 70(1):29–67, 1980. ISSN 0022-460X. doi: https://doi.org/10.1016/0022-460X(80)90553-2. URL http://www.sciencedirect.com/science/article/pii/0022460X80905532.

[12] David M Chase. Mean velocity profile of a thick turbulent boundary layer along a circular cylinder. *AIAA Journal*, 10(7):849–850, 1972. ISSN 0001-1452.

[13] Francis H Clauser. Turbulent boundary layer in adverse pressure gradient. *J. Aero. Sci.*, 21:91–108, 1954.

[14] D. Coles. The law of the wake in the turbulent boundary layer. *Journal of Fluid Mechanics*, 1(2):191–226, 1956.

[15] ER Corino and RS Brodkey. A visual study of turbulent shear flow. *J. Fluid Mech*, 37 (1):30, 1969.

[16] D.B. DeGraaff and J. Eaton. Reynolds-number scaling of the flat-plate turbulent boundary layer. *Journal of Fluid Mechanics*, 422:319–346, 2000.

[17] William J. Devenport, Ricardo A. Burdisso, Aurelien Borgoltz, Patricio A. Ravetta, Matthew F. Barone, Kenneth A. Brown, and Michael A. Morton. The kevlar-walled anechoic wind tunnel. *Journal of Sound and Vibration*, 332(17):3971–3991, 2013. ISSN 0022-460X. doi: https://doi.org/10.1016/j.jsv.2013.02.043. URL http://www.sciencedirect.com/science/article/pii/S0022460X13002848.

[18] Artur Dróżdż and Witold Elsner. Amplitude modulated near-wall cycle in a turbulent boundary layer under an adverse pressure gradient. *J Archives of Mechanics*, 65(6): 511–525, 2013. ISSN 0373-2029.

[19] PA Durbin and SE Belcher. Scaling of adverse-pressure-gradient turbulent boundary layers. *Journal of Fluid Mechanics*, 238:699–722, 1992.

[20] H. E. Fiedler. Coherent structures in turbulent flows. *Progress in Aerospace Sciences*, 25(3):231–269, 1988. ISSN 0376-0421. doi: https://doi.org/10.1016/0376-0421(88)90001-2. URL http://www.sciencedirect.com/science/article/pii/0376042188900012.

[21] Bharathram Ganapathisubramani, Ellen K. Longmire, and Ivan Marusic. Characteristics of vortex packets in turbulent boundary layers. *Journal of Fluid Mechanics*, 478:35–46, 2003. ISSN 0022-1120. doi: 10.1017/S0022112002003270. URL https://www.cambridge.org/core/article/characteristics-of-vortex-packets-in-turbulent-boundary-layers/7AD29033F7D6FF2E105CF54C07CD7A0C.

[22] Stewart Glegg and William Devenport. *Aeroacoustics of low Mach number flows: fundamentals, analysis, and measurement*. Academic Press, 2017. ISBN 0128097930.

[23] Stewart Glegg, Michael Morton, and William Devenport. Rotor inflow noise caused by a boundary layer: theory and examples. In *18th AIAA/CEAS Aeroacoustics Conference (33rd AIAA Aeroacoustics Conference)*, page 2263, 2012.

[24] Stewart A Glegg, Nicole Perry, and William J Devenport. Turbulence ingestion noise in complex flows. In *25th AIAA/CEAS Aeroacoustics Conference*, page 2636.

[25] Stewart A. L. Glegg, William Devenport, and Nathan Alexander. Broadband rotor noise predictions using a time domain approach. *Journal of Sound and Vibration*, 335: 115–124, 2015. ISSN 0022460X. doi: 10.1016/j.jsv.2014.09.007.

[26] Michael Goody. Empirical spectral model of surface pressure fluctuations. *AIAA Journal*, 42(9):1788–1794, 2004. ISSN 0001-1452. doi: 10.2514/1.9433.

[27] James M. Hamilton, John Kim, and Fabian Waleffe. Regeneration mechanisms of near-wall turbulence structures. *Journal of Fluid Mechanics*, 287:317–348, 1995. ISSN 0022-1120. doi: 10.1017/S0022112095000978. URL `https://www.cambridge.org/core/article/regeneration-mechanisms-of-nearwall-turbulence-structures/3A4EDE208C75EFC5250278B4D11DC0F9`.

[28] Z. Harun, J. P. Monty, R. Mathis, and I. Marusic. Pressure gradient effects on the large-scale structure of turbulent boundary layers. *Journal of Fluid Mechanics*, 715: 477–98, 2013. ISSN 0022-1120. doi: 10.1017/jfm.2012.531. URL `http://dx.doi.org/10.1017/jfm.2012.531`.

[29] M. R. Head and P. Bandyopadhyay. New aspects of turbulent boundary-layer structure. *Journal of Fluid Mechanics*, 107:297–338, 1981. ISSN 0022-1120. doi: 10.1017/S0022112081001791. URL `https://www.cambridge.org/core/article/new-aspects-of-turbulent-boundarylayer-structure/5DE439FC314ACEF7D5C6D7448F10667B`.

[30] Christopher John Hickling. *Inhomogeneous, Anisotropic Turbulence Ingestion Noise in Two Open Rotor Configurations*. PhD thesis, Virginia Tech, 2020.

[31] Scott E. Hommema and Ronald J. Adrian. Packet structure of surface eddies in the atmospheric boundary layer. *Boundary-Layer Meteorology*, 106(1):147–170, 2003. ISSN 1573-1472. doi: 10.1023/A:1020868132429. URL `https://doi.org/10.1023/A:1020868132429`.

[32] A. K. M. Fazle Hussain. Coherent structures and turbulence. *Journal of Fluid Mechanics*, 173:303–356, 1986. ISSN 0022-1120. doi: 10.1017/S0022112086001192. URL `https://www.cambridge.org/core/article/coherent-structures-and-turbulence/4B9538E410B2D70C412DD1A4CB7BE154`.

[33] N Hutchins and Ivan Marusic. Evidence of very long meandering features in the logarithmic region of turbulent boundary layers. 2007.

[34] N. Hutchins, T.B. Nickels, I. Marusic, and M. S. Chong. Hot-wire spatial resolution issues in wall-bounded turbulence. *Journal of Fluid Mechanics*, 635:103–168, 2009. doi: 10.1017/S0022112009007721.

[35] N. Hutchins, J. P. Monty, B. Ganapathisubramani, H. C. H. Ng, and I. Marusic. Three-dimensional conditional structure of a high-reynolds-number turbulent boundary layer. *Journal of Fluid Mechanics*, 673:255–285, 2011. ISSN 0022-1120. doi: 10.1017/S0022112010006245.

[36] Javier JimÉNez and Alfredo Pinelli. The autonomous cycle of near-wall turbulence. *Journal of Fluid Mechanics*, 389:335–359, 1999. ISSN 0022-1120. doi: 10.1017/S0022112099005066. URL https://www.cambridge.org/core/article/autonomous-cycle-of-nearwall-turbulence/150E7F8DA5E1F4A96BA2A301C2D24A9F.

[37] Javier JimÉNez, Sergio Hoyas, Mark P. Simens, and Yoshinori Mizuno. Turbulent boundary layers and channels at moderate reynolds numbers. *Journal of Fluid Mechanics*, 657:335–360, 2010. ISSN 0022-1120. doi: 10.1017/S0022112010001370. URL https://www.cambridge.org/core/article/turbulent-boundary-layers-and-channels-at-moderate-reynolds-numbers/E8735442AFB972D02342A9D2A340D398.

[38] Stephen A. Jordan. On the axisymmetric turbulent boundary layer growth along long thin circular cylinders. *Journal of Fluids Engineering*, 136(5), 2014. ISSN 0098-2202. doi: 10.1115/1.4026419. URL https://doi.org/10.1115/1.4026419.

[39] John Kim, Parviz Moin, and Robert Moser. Turbulence statistics in fully developed channel flow at low reynolds number. *Journal of fluid mechanics*, 177:133–166, 1987.

[40] Vassili Kitsios, Atsushi Sekimoto, Callum Atkinson, Juan A Sillero, Guillem Borrell, Ayse G Gungor, Javier Jiménez, and Julio Soria. Direct numerical simulation of a self-similar adverse pressure gradient turbulent boundary layer at the verge of separation. *Journal of Fluid Mechanics*, 829:392–419, 2017. ISSN 0022-1120.

[41] Joseph C. Klewicki. Reynolds number dependence, scaling, and dynamics of turbulent boundary layers. *Journal of Fluids Engineering*, 132(9):094001–094001–48, 2010. ISSN 0098-2202. doi: 10.1115/1.4002167. URL http://dx.doi.org/10.1115/1.4002167.

[42] S. J. Kline, W. C. Reynolds, F. A. Schraub, and P. W. Runstadler. The structure of turbulent boundary layers. *Journal of Fluid Mechanics*, 30(4):741–773, 1967. ISSN 0022-1120. doi: 10.1017/S0022112067001740. URL https://www.cambridge.org/core/article/structure-of-turbulent-boundary-layers/D0DEB24FDF12498D1574F36FA976B688.

[43] Praveen Kumar and Krishnan Mahesh. Large-eddy simulation of flow over an axisymmetric body of revolution. *Journal of Fluid Mechanics*, 853:537–563, 2018. ISSN 0022-1120. doi: 10.1017/jfm.2018.585. URL https://www.cambridge.org/core/article/largeeddy-simulation-of-flow-over-an-axisymmetric-body-of-revolution/2FDAE3309AD808096982072973A4AEAC.

[44] Jae Hwa Lee. Large-scale motions in turbulent boundary layers subjected to adverse pressure gradients. *Journal of Fluid Mechanics*, 810:323–61, 2017. ISSN 0022-1120. doi: 10.1017/jfm.2016.715. URL http://dx.doi.org/10.1017/jfm.2016.715.

[45] R. M. Lueptow and H. G. Nepomuceno. Pressure and shear stress measurements at the wall in a turbulent boundary layer on a cylinder. *Physics of Fluids*, 9(9):2732–9, 1997. ISSN 1070-6631. doi: 10.1063/1.869384. URL http://dx.doi.org/10.1063/1.869384.

[46] Y. Maciel, Wei Tie, A. G. Gungor, and M. P. Simens. Outer scales and parameters of adverse-pressure-gradient turbulent boundary layers. *Journal of Fluid Mechanics*, 844:5–35, 2018. ISSN 0022-1120. doi: 10.1017/jfm.2018.193. URL http://dx.doi.org/10.1017/jfm.2018.193.

[47] Yvan Maciel, Karl-Stephane Rossignol, and Jean Lemay. Self-similarity in the outer region of adverse-pressure-gradient turbulent boundary layers. *AIAA Journal*, 44(11):2450–2464, 2006. ISSN 00011452. doi: 10.2514/1.19234. URL http://dx.doi.org/10.2514/1.19234.

[48] Yvan Maciel, Ayse G. Gungor, and Mark Simens. Structural differences between small and large momentum-defect turbulent boundary layers. *International Journal of Heat and Fluid Flow*, 67:95–110, 2017. ISSN 0142-727X. doi: https://doi.org/10.1016/j.ijheatfluidflow.2017.07.011. URL http://www.sciencedirect.com/science/article/pii/S0142727X17300474.

[49] R. Mathis, N. Hutchins, and I. Marusic. Large-scale amplitude modulation of the small-scale structures in turbulent boundary layers. *Journal of Fluid Mechanics*, 628:311–337, 2009. doi: 10.1017/S0022112009006946.

[50] George L. Mellor. The effects of pressure gradients on turbulent flow near a smooth wall. *Journal of Fluid Mechanics*, 24(2):255–274, 1966. ISSN 0022-1120. doi: 10.1017/S0022112066000624. URL https://www.cambridge.org/core/article/effects-of-pressure-gradients-on-turbulent-flow-near-a-smooth-wall/07CFB415B2C1DFE9981696F70BC6FC0D.

[51] Iii R. Minniti, W. Blake, and T. Mueller. *Determination of inflow distortions by interpreting aeroacoustic response of a propeller fan*. Aeroacoustics Conferences. American Institute of Aeronautics and Astronautics, 1998. doi: doi:10.2514/6.1998-228610.2514/6.1998-2286. URL https://doi.org/10.2514/6.1998-2286.

[52] Nicholas J. Molinaro, N. Agastya Balantrapu, Christopher Hickling, W. Nathan Alexander, William J. Devenport, and Stewart A. L. Glegg. The ingestion of wake turbulence into an open rotor. In *23rd AIAA/CEAS Aeroacoustics Conference, 2017, June 5, 2017 - June 9, 2017*, 23rd AIAA/CEAS Aeroacoustics Conference, 2017. American Institute of Aeronautics and Astronautics Inc, AIAA.

[53] Nicholas Joseph Molinaro. *The two point correlation structure of a cylinder wake*. PhD thesis, Virginia Tech, 2017.

[54] M.A. Morton. *Rotor Inflow Noise Caused by a Boundary Layer: Inflow Measurements and Noise Predictions*. Thesis, 2012. URL http://scholar.lib.vt.edu/theses/available/etd-08102012-103032/.

[55] H.H. Murray. *Turbulence and Sound Generated by a Rotor Operating Near a Wall*. Ms, 2016.

[56] Yasutaka Nagano, Toshihiro Tsuji, and Tomoya Houra. Structure of turbulent boundary layer subjected to adverse pressure gradient. *International Journal of Heat and Fluid Flow*, 19(5):563–572, 1998. ISSN 0142-727X. doi: https://doi.org/10.1016/S0142-727X(98)10013-9. URL http://www.sciencedirect.com/science/article/pii/S0142727X98100139.

[57] Ronald L. Panton. Overview of the self-sustaining mechanisms of wall turbulence. *Progress in Aerospace Sciences*, 37(4):341–383, 2001. ISSN 0376-0421. doi: https://doi.org/10.1016/S0376-0421(01)00009-4. URL http://www.sciencedirect.com/science/article/pii/S0376042101000094.

[58] VC Patel, A Nakayama, and R Damian. Measurements in the thick axisymmetric turbulent boundary layer near the tail of a body of revolution. *Journal of Fluid Mechanics*, 63(2):345–367, 1974. ISSN 1469-7645.

[59] AE Perry and WH Schofield. Mean velocity and shear stress distributions in turbulent boundary layers. *The Physics of Fluids*, 16(12):2068–2074, 1973. ISSN 0031-9171.

[60] J. Piquet and V. C. Patel. Transverse curvature effects in turbulent boundary layer. *Progress in Aerospace Sciences*, 35(7):661–672, 1999. ISSN 0376-0421. doi: https://doi.org/10.1016/S0376-0421(99)00007-X. URL http://www.sciencedirect.com/science/article/pii/S037604219900007X.

[61] Stephen Pope. *Turbulent Flows*. IOP Publishing, 2001. ISBN 0957-0233.

[62] GNV Rao and NR Keshavan. Axisymmetric turbulent boundary layers in zero pressure-gradient flows. *Journal of Applied Mechanics*, 39(1):25–32, 1972. ISSN 0021-8936.

[63] Lewis F Richardson. Weather prediction by numerical process cambridge university press. *cambridge university press*, 1922, 1922.

[64] S. K. Robinson. Coherent motions in the turbulent boundary layer. *Annual Review of Fluid Mechanics*, 23(1):601–639, 1991. ISSN 0066-4189. doi: 10.1146/annurev.fl.23.010191.003125. URL https://doi.org/10.1146/annurev.fl.23.010191.003125.

[65] DF Scharpf and TJ Mueller. An experimental investigation of the sources of propeller noise due to the ingestion of turbulence at low speeds. *Experiments in Fluids*, 18(4): 277–287, 1995. ISSN 0723-4864.

[66] D. M. Schatzman and F. O. Thomas. An experimental investigation of an unsteady adverse pressure gradient turbulent boundary layer: embedded shear layer scaling. *Journal of Fluid Mechanics*, 815:592–642, 2017. ISSN 0022-1120 1469-7645. doi: 10.1017/jfm.2017.65.

[67] Joseph A Schetz and Rodney DW Bowersox. *Boundary layer analysis*. American Institute of Aeronautics and Astronautics, 2011. ISBN 160086824X.

[68] M Sevik. Sound radiation from a subsonic rotor subjected to turbulence. 1974.

[69] Per Egil Skåre and Per-åge Krogstad. A turbulent equilibrium boundary layer near separation. *Journal of Fluid Mechanics*, 272:319–348, 1994. ISSN 0022-1120. doi: 10.1017/S0022112094004489. URL https://www.cambridge.org/core/article/turbulent-equilibrium-boundary-layer-near-separation/A104A1912FCB6E744860E8DF6F146E80.

[70] Alexander J. Smits, Beverley J. McKeon, and Ivan Marusic. High–reynolds number wall turbulence. *Annual Review of Fluid Mechanics*, 43(1):353–375, 2011. ISSN 0066-4189 1545-4479. doi: 10.1146/annurev-fluid-122109-160753.

[71] O. R. Tutty. Flow along a long thin cylinder. *Journal of Fluid Mechanics*, 602:1–37, 2008. ISSN 0022-1120. doi: 10.1017/S0022112008000542. URL https://www.cambridge.org/core/article/flow-along-a-long-thin-cylinder/D7AD9D975137DA67C6B127F1F8662F69.

[72] Ralph J. Volino and Michael P. Schultz. Determination of wall shear stress from mean velocity and reynolds shear stress profiles. *Physical Review Fluids*, 3(3):034606, 2018. doi: 10.1103/PhysRevFluids.3.034606. URL https://link.aps.org/doi/10.1103/PhysRevFluids.3.034606.

[73] James M Wallace. Quadrant analysis in turbulence research: history and evolution. *Annual Review of Fluid Mechanics*, 48:131–158, 2016.

[74] Anthony Wietrzak and Richard M. Lueptow. Wall shear stress and velocity in a turbulent axisymmetric boundary layer. *Journal of Fluid Mechanics*, 259:191–218, 1994. ISSN 0022-1120. doi: 10.1017/S0022112094000091. URL https://www.cambridge.org/core/article/

wall-shear-stress-and-velocity-in-a-turbulent-axisymmetric-boundary-layer/17EFE6DD1B10B43CF529F8E39B4012ED.

[75] D. Wisda. *Noise from a Rotor Ingesting Inhomogeneous Turbulence*. Thesis, 2015.

[76] John P. Wojno, Thomas J. Mueller, and William K. Blake. Turbulence ingestion noise, part 1: Experimental characterization of grid-generated turbulence. *AIAA Journal*, 40 (1):16–25, 2002. ISSN 0001-1452. doi: 10.2514/2.1636. URL https://doi.org/10.2514/2.1636.

[77] J.P. Wojno. *An Experimental Investigation of the Aeroacoustic Response of a Ten-Bladed Rotor Ingesting Grid-Generated Turbulence*. Thesis, 1999.

[78] Kristofer M. Womack, Charles Meneveau, and Michael P. Schultz. Comprehensive shear stress analysis of turbulent boundary layer profiles. *Journal of Fluid Mechanics*, 879:360–389, 2019. ISSN 0022-1120. doi: 10.1017/jfm.2019.673. URL https://www.cambridge.org/core/article/comprehensive-shear-stress-analysis-of-turbulent-boundary-layer-profiles/DC05D177E6AA069B3E2FE333A13D2115.

[79] Mark V. Zagarola and Alexander J. Smits. Mean-flow scaling of turbulent pipe flow. *Journal of Fluid Mechanics*, 373:33–79, 1998. ISSN 0022-1120. doi: 10.1017/S0022112098002419. URL https://www.cambridge.org/core/article/meanflow-scaling-of-turbulent-pipe-flow/20DD24A940AA29EB700A4AE71A3E5C78.

[80] Jigen Zhou, Ronald J Adrian, and S Balachandar. Autogeneration of near-wall vortical structures in channel flow. *Physics of Fluids*, 8(1):288–290, 1996.